INFORMATION TO USERS

This manuscript has been reproduced from the microfilm master. UMI films the text directly from the original or copy submitted. Thus, some thesis and dissertation copies are in typewriter face, while others may be from any type of computer printer.

The quality of this reproduction is dependent upon the quality of the copy submitted. Broken or indistinct print, colored or poor quality illustrations and photographs, print bleedthrough, substandard margins, and improper alignment can adversely affect reproduction.

In the unlikely event that the author did not send UMI a complete manuscript and there are missing pages, these will be noted. Also, if unauthorized copyright material had to be removed, a note will indicate the deletion.

Oversize materials (e.g., maps, drawings, charts) are reproduced by sectioning the original, beginning at the upper left-hand corner and continuing from left to right in equal sections with small overlaps. Each original is also photographed in one exposure and is included in reduced form at the back of the book.

Photographs included in the original manuscript have been reproduced xerographically in this copy. Higher quality 6" x 9" black and white photographic prints are available for any photographs or illustrations appearing in this copy for an additional charge. Contact UMI directly to order.

U·M·I

University Microfilms International
A Bell & Howell Information Company
300 North Zeeb Road, Ann Arbor, MI 48106-1346 USA
313/761-4700 800/521-0600

Reproduced with permission of the copyright owner. Further reproduction prohibited without permission.

Order Number 9405603

Spin polarized x-ray photoelectron spectroscopy

Xu, Zhongde, Ph.D.

City University of New York, 1993

U·M·I
300 N. Zeeb Rd.
Ann Arbor, MI 48106

4

SPIN POLARIZED X-RAY PHOTOELECTRON SPECTROSCOPY

by

Zhongde Xu

A dissertation submitted to the Graduate Faculty in Physics
in partial fulfillment of the requirement for the degree of
Doctor of Philosophy, The City University of New York.

1993

This manuscript has been read and accepted for the Graduate Faculty in Physics in satisfaction of the dissertation requirement for the degree of Doctor of Philosophy.

July 7, 1993
Date

Leonard O. Roellig Leonard O. Roellig
Chair of Examining Committee

July 15, 1993
Date

Joseph B. Krieger Joseph B. Krieger
Executive Officer

Peter D. Johnson Peter D. Johnson

Martin A. Kramer Martin A. Kramer

Fred H. Pollak Fred H. Pollak

Myron Strongin Myron Strongin
Supervisory Committee

The City University of New York

ABSTRACT

SPIN POLARIZED X-RAY PHOTOELECTRON SPECTROSCOPY

by

Zhongde Xu

Advisor: Dr. Peter D. Johson

A new electron spectrometer for spin polarized x-ray photoelectron spectroscopy (XPS) study is described. With a plane mirror analyzer (PMA) connected in between the hemispherical electron energy analyzer and the low energy diffuse scattering electron spin polarimeter, it is possible to simultaneously measure both transverse and longitudinal electron spin polarization components. The operating characteristics of the spectrometer are demonstrated on X1B, an undulator based soft x-ray beamline at the National Synchrotron Light Source (NSLS). Results obtained from simple ferromagnetic systems such as Fe and Co are consistent with existing data.

Cr and Mn thin films on Fe(100) are studied experimentally. The spin polarized core level photoemission from a Cr monolayer on Fe(100) shows that the Cr monolayer is ferromagnetically aligned within the plane but antiferromagnetically aligned with respect to the Fe substrate. With the deposition of a second monolayer of Cr, it is no longer possible to measure a net spin polarization in the Cr $3p$ level. This is consistent with a picture in which the Cr layers couple antiferromagnetically with respect to each other. Spin polarized Mn $3p$ spectra of Mn overlayer on Fe(100) with different Mn film thicknesses at both room temperature and –120° C show no measurable net polarization. The results indicate that the Mn overlayer on Fe(100) can not form a ferromagnetic structure above temperature –120°C.

The complexities of the spin polarized core level spectra are examined by simple modeling. This model is based on the core hole atomic multiplet structure and quenching of the *d* electron orbital component in 3*d* transition metals. Based on this simple model, the experiment results from a monolayer of Cr on Fe(100) are shown to be consistent with a predicted local magnetic moment of ~ 3 Bohr magnetons on the Cr site.

ACKNOWLEDGMENTS

The author wishes to express his gratitude to Dr. Peter D. Johnson of Physics Department, Brookhaven National Laboratory (BNL) for his supervision of this research. The author is also indebted to Mr. Fran E. Loeb of Physics Department, BNL for his general technical assistance. Besides, the writer wishes to acknowledge the following for their valuable helps during the course of this work:

Mr. J. Altman	Physics Department of the City College of New York, (spin polarimeter parts machining).
Dr. J. W. Davenport	Physics Department of BNL, (TD).
Dr. W. Eberhardt	Institut für Festkörperforxchung der KFA, Germany, (TD).
Dr. K. C. Garrison	Physics Department of BNL, general discussions, (EA, TA).
Dr. S. L. Hulbert	National Synchrotron Light Source (NSLS) of BNL, (ES, TA).
Dr. B. S. Itchkawitz	Fritz-Haber-Institut der Max-Planck-Gesellschaft, Germany. (EA, TA, proof reading).
Dr. C. Kao	NSLS of BNL, (TD).
Dr. P. Kuiper	Physics Department of BNL, (TD).
Dr. Y. Ma	Pacific Northwest National Laboratory, (EA, TA).
Dr. J. K. Randall	Advanced Photon Source (APS) of Argonne National Laboratory (ANL), (EA, TA).
Dr. M. W. Ruckman	Physics Department of BNL, (ES).
Dr. M. Strongin	Physics Department of BNL, (ES).
Dr. K. Tsuei	Physics Department of BNL, (TA, TD).

Dr. M. T. Weinert Physics Department of BNL, (TD).
Technical Support Group and Vacuum Group of NSLS, BNL, (ES, TA).
EA: Experimental Aid, ES: Equipment Support, TA: Technical Advice,
TD: Theoretical Discussion.

Finally, the author is especially grateful to Prof. Leonard O. Roellig of the Physics Department of the City College of New York, for his support throughout this work.

Zhongde Xu

Upton, New York
June, 1993.

CONTENTS

LIST OF FIGURES AND TABLES

ABBREVIATIONS

ADC	Analog to Digital Converter.
AES	Auger Electron Spectroscopy.
AFM	Antiferromagnetic.
ALS	Advanced Light Source (SSR at Berkeley, USA).
APS	Advanced Photon Source (SSR at Argonne, USA).
BESSY	Berliner Elecktronenspeicherring-Gesellschaft für Synchrotronstrahlung mbH (SSR at Berlin, Germany).
BM	Bending Magnet.
CEM	Cylindrical Element Monochromator.
CMA	Cylindrical Mirror Analyzer.
DAC	Digital to Analog Converter.
EELS	Electron Energy Loss Spectroscopy.
ELETTRA	Sincrotrone Trieste (SSR at Trieste, Italy).
FM	Ferromagnetic.
FOM	Figure of Merit.
FWHM	Full-Width-Half-Maximum.
HFM	Horizontal Focusing Mirror.
NSLS	National Synchrotron Light Source (SSR at Brookhaven, USA).
PLEED	Polarized Low Energy Electron Diffraction.
PMA	Plane Mirror Analyzer.
RGA	Residual Gas Analyzer.
TGM	Toroidal Grating Monochromator.
TSP	Titanium Sublimation Pump.
TTL	Transistor Transistor Logic.
UHV	Ultrahigh Vacuum.

VFM	Vertical Focusing Mirror.
VLEED	Very Low Energy Electron Diffraction.
VUV	Vacuum Ultraviolet.
SSR	Synchrotron Storage Ring.
XPS	X-ray Photoelectron Spectroscopy.
XR	X-ray Ring.

OVERVIEW

The properties of bulk magnetic materials such as Fe and Co have been fairly well studied using conventional magnetic probing techniques such as neutron scattering and Mössbauer spectroscopy. On the other hand, our knowledge of the magnetic properties of surfaces, interfaces and thin films is still insufficient because it is difficult to obtain reliable magnetic information on individual atoms for these systems with the conventional magnetic probing techniques.

Spin polarized core level x-ray photoelectron spectroscopy (XPS) is a young but promising field. It is both surface sensitive and element specific, and its capability for distinguishing photoelectron spin components makes it a particularly usefully probe of the magnetic ordering of surfaces, interfaces and thin films. A long standing question which still remains unsolved is to what extent, in a magnetic system, the core level XPS spectra reflects the exchange coupling between core and valence electrons. A thorough understanding of such multi-electron effects is necessary for obtaining information on the magnetic ground state from the technique.

Due to the complexity of the core level photoionization process in ferromagnetic transition metals, there have been no theoretical calculations up to now for spin polarized core level XPS spectra of magnetic metals which include the electron correlation as well as the atomic and solid state effects. On the experimental side, the inherent inefficiency of the spin polarimeters makes it very difficult for any spin polarized core level XPS studies. This has been partially compensated by the availability of the high flux photon sources from insertion devices that began operating at synchrotron light sources in the later eighties. In spite of those developments, there are still only a few experimental spectra in the data-base so far.

The main purpose of the work presented in this thesis is to establish a new spectrometer for spin polarized XPS studies. This includes the design and construction of the spin polarized electron analyzer, the experimental set up for magnetic surface, interface and thin film sample treatment and characterization, and the development of the experimental control and data acquisition system. A simple model has also been used to try to obtain a clearer physical understanding of the results obtained in the preliminary experiments. Hopefully the experiment results and the discussion presented in this work will provide some new insights and a better understanding of the problems associated with core level spin polarized XPS as well as the magnetic structure of surface, interface and thin film materials.

A discussion of spin polarized core level XPS is given in Chapter 1. After an introduction in section 1.1, a brief discussion and summary of the problems in both the theory and experiment of spin integrated core level XPS from transition metals is given in section 1.2. Section 1.3 includes a summary of the current experimental situation of spin polarized core level XPS and a discussion of the current models interpreting the photoemission process. Section 1.4 provides an example of applications of spin polarized core level XPS.

The inherent inefficiency of spin detectors requires the brightest possible photon source to perform spin polarized core level XPS experimental studies. The X1 undulator is described in section 2.1 of chapter 2. The design considerations and layout details of the beamline are given in section 2.2 and details of its testing and commissioning are given in section 2.3.

Chapter 3 provides details on the layout, construction, and tests of the new electron spin polarization analyzer. The basic theory is described in section

3.1. A review and appraisal of the existing electron spin polarimeters is given in section 3.2 and the concept of low energy diffuse scattering electron spin polarimeters is introduced in section 3.3. Section 3.4 provides a detailed layout and assembly of the electron spin polarization analyzer. And finally, the test results and discussions of the analyzer are given in section 3.5.

Chapter 4 describes the core level spin polarized XPS experimental consideration. Section 4.1 introduces the basic principles of the spin polarized XPS experiment. In section 4.2, the features of the experimental system are described in detail. In section 4.3, the experimental control and data acquisition system layouts are provided.

Results from studies of Fe and Co are presented in chapter 5. Section 5.1 reviews the objectives of the experiments. In section 5.2, the detailed experimental procedures are described. Section 5.3 presents the Fe and Co 3*p* core level spin polarized XPS data. In section 5.4, based on the core hole atomic multiplet structure, a simple model is used to examine the data.

In chapter 6, the systems of Cr and Mn overlayers on Fe(100) are studied. Section 6.1 reviews the current work on Cr/Fe(100). Section 6.2 gives the experimental procedures, and in section 6.3, the discussions of the experimental results are presented.

Finally, the conclusions and the future recommendations are presented in the summary.

Chapter 1. Spin Polarized Core Level XPS

1.1 Introduction

An electron with binding energy E_b below the vacuum level is excited by an incoming photon of energy $h\nu$ and is emitted from the solid with a kinetic energy $E_k = h\nu - E_b$. This process is called the photoelectric effect. Figure 1.1 shows a schematic diagram of the process. The energy distribution of photoemitted electrons reflects the initial energy distribution of electronic states in the solid shifted in energy by $h\nu$. The emission of electrons from solids by photons was first observed by Hertz[1.1] in 1887. The correct explanation of the effect was given by Einstein[1.2] eighteen years later. Since then, photoemission has evolved to be an indispensable probe in the solid state physics. This is particularly true in surface science because the short mean free path of the photoelectrons in solids means the photoemission spectra primarily reflect the electronic states of the surface.

It was established by Siegbahn and co-workers[1.3] that sharp peaks are observed in the photoelectron spectra of solids irradiated by monochromatic x-rays. These peaks correspond to occupied core electron energy levels. Since different atoms have different characteristic core level electron binding energies, core level x-ray photoemission spectroscopy (XPS) can identify different chemical species present near the surface. Furthermore, the binding energies are sensitive to local-charge environments, and hence the XPS peaks shift significantly as the local chemical environment (e.g., valence state) is altered. Therefore, increasingly better resolution in XPS has led to a wealth of information on the changes of atomic core levels associated with the changes in the local atomic environment.

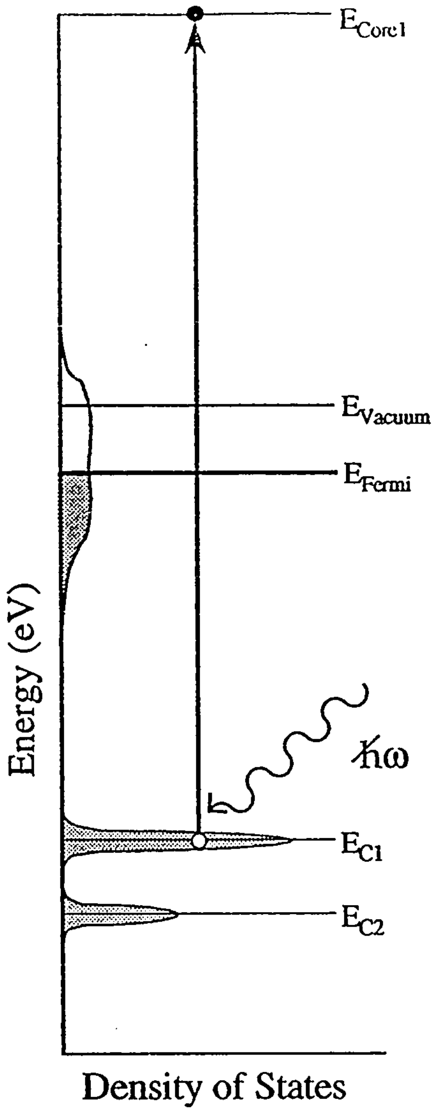

Figure 1.1 Schematic diagram of the photoemission process.

Core level x-ray photoemission spectra from transition metals often show energy level splittings which do not appear for simple metals. It was first suggested about 20 years ago[1.4-1.6] that one could use the core level splittings as a monitor of the local magnetic moment because the splitting should vary linearly with the spin state of the unfilled inner shell. In the atomic model, the spin of a core level electron is coupled to the spin of the localized *d* electrons on the same site via the direct exchange interaction. For transition metals, which have unpaired valence *d* electrons, the exchange interaction affects spin-parallel and spin-antiparallel core electrons unequally with respect to the spin of the localized *d* electrons. For *s* levels, the resulting splitting is directly proportional to the exchange interaction, and the intensity ratio between the peaks should be $(S + 1){:}S$, as proposed by van Vleck.[1.7] Here S is the magnitude of the total spin of localized *d* electrons. There have been various attempts based on this argument to employ the multiplet splittings as a diagnostic of the local magnetic moment.[1.8-1.10]

On the other hand, the splitting in Ni XPS spectra was interpreted as the formation of an atomic two-hole bound state.[1.11,1.12] In this picture, the core hole interacts with the valence electrons on the same site via the Coulomb interaction. The resulting core level spectrum is considered a simple superposition of spectra with different *d* electron configurations. The basic idea is that the ground state may be regarded as a mixture of basis states of similar energy but with different numbers of *d* electrons, so that the number of *d* electrons in the ground state is nonintegral. In the final state, the energies of the corresponding basis states are no longer similar upon photoionization, hence they mix less strongly, and separate peaks are observed in the XPS spectrum due to transitions to the different final states.

Both the exchange interaction and the configuration mixing picture of splitting in the core levels are based solely on the atomic picture. However, because of the high electron mobility for metallic systems, one may go to the fully delocalized extreme. In this limit, a core hole undergoes an average coupling with the itinerant *d* electrons. When the system is magnetic, the splitting is proportional to the local magnetization S_z, and one may naively think that the *s* level photo emission intensity ratio should be 1:1.[1.14,1.15,1.28] Nevertheless, this is theoretically incorrect as will be shown later in this chapter.

Since the first measurements of multiplet splittings in XPS, people have come to understand much more about the spectra, and the original idea that the multiplet splitting gives a direct measurement of the ground state magnetic moment has been questioned.[1.13-1.16] An extensive collection of data on Fe 3*s* splittings of Fe compounds by van Acker *et al.*[1.17] show that the multiplet splittings and the intensity ratios do not always correlate with the magnetic moment. The most remarkable result was that 3*s* splittings were found in compounds which do not have a local magnetic moment.

These findings might be taken as evidence to exclude the exchange interaction as the origin of the observed splittings. Nevertheless, core level electrons are in fact, affected by the moment of the *d* electrons via exchange interaction, no matter that the *d* electrons are localized or itinerant or both, as can be seen from the hyperfine splittings in Mössbauer spectroscopy.[1.18] If the core level splitting due to the exchange interaction can be distinguished from the other contributions, it will be extraordinarily useful in studying the magnetic structure of complex ferromagnetic systems such as transition metal alloys, interfaces and thin films. The core level XPS can identify different chemical species present on the surface; the multiplet splitting corresponding to different species can provide information on the magnitude and direction of the local magnetic moments for each species.

1.2 Multiplet Splitting in Core Level XPS of Transition Metals

The first systematic investigation of core level transition metal XPS was performed by Fadley and Shirley.[1.4,1.5] They investigated the spectra of the 3*s* inner core electrons for Fe, Co, Ni and Cu and found a characteristic line splitting of 4.5 eV in Fe and 6 eV in Ni. The splitting was found to be uncertain in Co but definitely absent in Cu. The splitting was interpreted as being due to the direct exchange interaction between the 3*s* core level electron and the 3*d* valence electrons at the same atomic site. The exchange interaction acts only between electrons with the same spin within the Hartree-Fock scheme.[1.19] Thus core electrons with spins-parallel to those of the unpaired valence electrons will experience the direct exchange interaction, while those with spins-antiparallel will not. Since the exchange interaction reduces the average Coulomb repulsion between two electrons, the binding energy of the spin-parallel core electrons is expected to be higher compared to that of spin-antiparallel core electrons. Therefore, the spin-parallel and spin-antiparallel core electrons will be separated in energy in XPS spectra.

The simplest calculation based on an atomic model can be obtained by using van Vleck's theorem.[1.7] For a filled *s* orbit in the presence of an open *l* orbit (for a *d* orbit, $l = 2$), the final configuration will have two states split by

$$\Delta E = \frac{2S+1}{2l+1} G^l(sl), \tag{1.1}$$

where S is the total spin of the valence electrons and $G^l(sl)$ is the Slater exchange integral. The spin of the final states will be $S - 1/2$ and $S + 1/2$, with the higher-spin state lying lower in energy as is expected. The relative intensities of the two photoemission peaks both for the majority and minority distribution curves (photoelectrons with spin magnetic moment components parallel and antiparallel to the magnetic moment component of the valence electrons) are (see appendix 1.1)

$$I_{\text{maj}}\left(S+\frac{1}{2}\right)=\frac{1}{2S+1}, \tag{1.2}$$

$$I_{\text{maj}}\left(S-\frac{1}{2}\right)=\frac{2S}{2S+1}; \tag{1.3}$$

$$I_{\text{min}}\left(S+\frac{1}{2}\right)=1, \tag{1.4}$$

$$I_{\text{min}}\left(S-\frac{1}{2}\right)=0. \tag{1.5}$$

Note that the minority curve has only one peak and that the ratio between the two peaks for the majority curve is

$$R_{\text{maj}} = \frac{I_{\text{maj}}(S+1/2)}{I_{\text{maj}}(S-1/2)} = \frac{1}{2S}. \tag{1.6}$$

The total intensity ratio between the two peaks for $S + 1/2$ and $S - 1/2$ is then

$$R_{\text{total}} = \frac{I_{\text{maj}}(S+1/2)+I_{\text{min}}(S+1/2)}{I_{\text{maj}}(S-1/2)+I_{\text{min}}(S-1/2)} = \frac{S+1}{S}. \tag{1.7}$$

The numerical results for the splittings obtained from equation (1.1) by using the Hartree-Fock approximation are always more than a factor of two larger than the observed splittings. This disagreement illustrates the failure of the one-electron theory.

The exchange interaction originates from the Pauli exclusion principle which states that parallel-spin electrons must be spatially separated. This lowers the total energy of the system with parallel-spin electrons. It has long been recognized that there is an almost equally important tendency of even electrons with antiparallel spins to avoid one another because of their Coulomb repulsion.[1.20] This is called the correlation effect, which should be taken into account for any theory of magnetization energy to have even a qualitative validity.

The subject of core level transition metal XPS is a many-body problem. Due to the electron correlation effect, the antiparallel-spin (higher binding energy) state has less electron-electron repulsion between the *s* and *d* electrons than estimated within the Hartree-Fock approximation which ignores the correlation effect and hence over estimates the Coulomb repulsion force between antiparallel-spin electrons. This affects both the energy splitting of the multiplet and the relative peak intensities. Electron correlation in real systems therefore lowers the energy of the antiparallel-spin (higher-energy) state and reduces the splitting.

Bagus *et al.*[1.21] used the configuration interaction method to determine the electron correlation effect for 2*s* and 3*s* splittings. The set of configurations was formed by distributing the *d* shell electrons among the 3*s*, 3*p*, and 3*d* orbitals to be consistent with the angular momentum of the multiplet. For the antiparallel-spin state, the Slater Coulomb and exchange integrals involved in the off-diagonal matrix elements are large, and substantial mixing of the internal configurations can occur. The center weight of the antiparallel-spin states then shift toward lower energy resulting in a smaller splitting. This configuration interaction method corrects the calculation based on the one-electron picture with Hartree-Fock approximation and it predicts the existence of new structure for the 3*s* binding energy splittings — structure which does not exist in the one-electron theory and which has been confirmed experimentally then by Kowalczyk *et. al.*[1.22]

In the mid-seventies, sample studies[1.23-1.25] had shown that results from a number of XPS measurements on nonmetallic transition metal compounds, and also on rare-earth metals and ionic compounds, were compatible with this scheme. It seems that the subject has been closed and many subsequent attempts have been made to use the multiplet splittings as a measure of the local magnetic moment.[1.8-1.10,1.25]

However, the problem seems indeed much more complicated than just that. Van Acker *et al.*[1.17] did extensive experimental studies on various 3*d* transition metal systems. The experimental data indicate poor correlation between core level splittings and magnetic moments as measured by other methods, such as neutron scattering and Mössbauer spectroscopy. It is clear that XPS multiplet splittings are not exclusively due to the exchange interaction between the core hole and the unpaired valence electrons. A real physical model of the core level photoionization needs to take account of the exchange interactions between core and valence electrons, atomic multiplet structure, screening effects and charge variations, and the strength of hybridization between the valence electrons, as well as the effective electron correlation between the valence electrons. In practice this is very difficult.

A typical example of non-exchange splitting is found in the Ni XPS spectra. These spectra show a satellite line about 6 eV below each main line for all levels with binding energies below 1 keV.[1.11] This applies even to the valence band. Clearly this 6 eV splitting is not due to the exchange interaction between the core level electrons and the *d* electrons since otherwise the splitting should not be the same for different core shells. The wave functions of 3*d* electrons overlap much less with 2*p* wavefunction than 3*s* or 3*p* wavefunctions and hence the exchange integral must alter accordingly. The observed constant splitting can not be reconciled with the exchange interaction scheme. Instead, it has been interpreted as a two-hole final state interaction.[1.27] This is primarily due to the electron correlation effect and can be described by the configuration interaction. The final state may be regarded as a mixture of basis states of similar energy but with different numbers of d electrons, so that the number of d electrons in the state is nonintegral. Upon photoionization, the final state energies of the corresponding basis states are no longer similar, so they mix less strongly, and separate peaks are observed in the XPS spectrum. These are due to transitions to the different final basis states. For Ni, the main peak at lower binding energy corresponds to the d^{10} state while the satellite peak at higher binding energy corresponds to the d^9 state. Thus in this picture, the splitting between the peaks is not due to the exchange interaction between core level electrons and valence d electrons and it does not reflect the local magnetic moment.

In order to settle the controversy concerning the origin of the 3*s* satellites and their relevance to local magnetic moments, Oh *et al.*[1.29] proposed a semi-empirical method. Since the wave function overlap between the 2*p* and the 3*d* wavefunctions is small, the splitting due to the exchange interaction can be neglected for 2*p* spectra. The method is to first extract the non-exchange splitting parameters by fitting the 2*p* spectra. The parameters of the fit include the charge transfer energy from the ligand 4*p* level to the transition metal 3*d* state Δ, the Coulomb repulsion energy between 3*d* electrons U, the hybridization parameter between p and 3*d* levels T, and the Coulomb attraction between the 2*p* core hole and the 3*d* electrons Q_{2p}. The same parameters Δ, U, and T are then used to calculate the parallel-spin and antiparallel-spin final states separately, using different Q values for parallel-spin (Q_H) and antiparallel-spin (Q_L) configurations. With further restrictions and approximations, the authors were able to fit the experimental data. This model works well with all the spin unresolved experimental data currently existing for the 3*s* core level spectra of

Mn and Fe insulating compounds. Unfortunately the electron correlation effect and the electron exchange interaction between the core and valence electrons were phenomenologically included in the Coulomb attraction parameters Q_H and Q_L, so they could not be separated.

The models discussed so for have been based on an atomic picture. Such a procedure may be seriously questioned since the observed multiplet splittings are of the same order of magnitude as the *d* electron bandwidth reflecting the kinetic energy of the itinerant electrons. The core level electrons interact with the conduction electrons through the direct Coulomb and exchange interactions. In the atomic limit, the core hole tightly couples to the localized *d* electrons at the same site and an atomic spectrum is seen in the photoelectron cross section. In the opposite limit of delocalized conduction electrons with large kinetic energies, the core electrons only couple to an averaged conduction-electron number at the same site, according to the independent electron or Hartree-Fock picture. The true physical situation is somewhere between these two limiting cases.

Kakehashi *et al.* have proposed a simplified model in an attempt to resolve this problem.[1.14,1.16,1.28] The model is schematically shown in figure 1.2. The *d* electrons are described by a single-band Hubbard model with a Coulomb integral U and a transfer integral t_{ij} between sites i and j which is characteristic of the *d* electron bandwidth W. A core hole with spin S_c is coupled to the *d* electrons on the same site via the Coulomb and the exchange interactions V and J. The model neglects the fivefold degeneracy of the *d* band and the existence of *sp* hybridization of the conduction electrons. The numerical calculations performed by the authors demonstrated how the line shape of the core spectra varies in terms of the Coulomb and exchange interactions V, the *d* electron bandwidth W, and Coulomb interaction U between the *d* electrons. The change

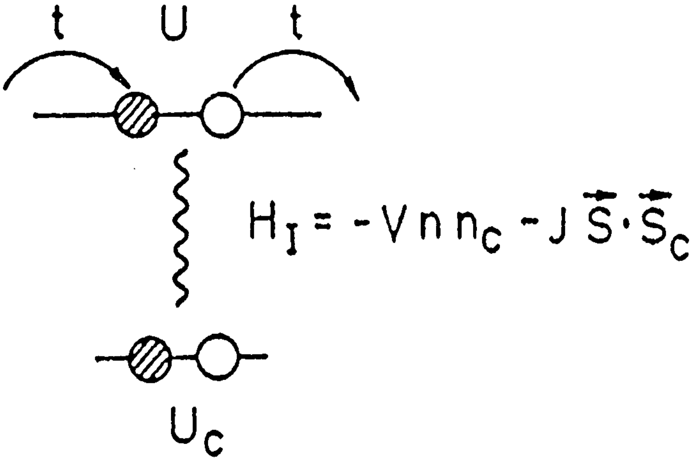

Figure 1.2 Model for transition metal core level XPS calculation. Localized core electrons with the Coulomb repulsion U_c are coupled to *d* electrons via the coupling H_I. *d* electrons have the transfer integrals *t* and the intra-atomic Coulomb integral *U*.[1.14]

of the line shape in terms of U is significant in the regime $0 < U < W$, indicating that the inclusion of U is very important for the core spectra of transition metals.

Since the model is simplified, it can not identify the type of splittings in the 3*s* core level spectra of 3*d* transition metals. However, the results of numerical calculations do qualitatively show that the singlet (core hole spin antiparallel to that of the *d* electrons) and the triplet (core hole spin parallel to that of the *d* electrons) peaks merge together when the exchange interaction between the core hole and *d* electrons $J/W = 0$. The singlet and the triplet peaks separate from each other in the delocalized limit, and the high binding energy side tail forms a satellite as U/W increases from zero even when $J/W = 0$, which is due to the electron correlation effect. The model includes the basic features of the inner core spectra but it is oversimplified in that it simply treats the *s* core level electron with spin parallel (triplet state $S + 1/2$) and antiparallel (singlet state $S - 1/2$) to that of the *d* electrons as equivalent to the minority ($m_s = -1/2$) and majority ($m_s = +1/2$) photoelectron.

The core level spectra in the ferromagnetic state will strongly depend on the spin component. This is true even when the fivefold degeneracy of the *d* orbitals is taken into account. Spin polarized core level XPS is therefore necessary to resolve the complexity and it will serve as a useful tool in determining the origins of the multiplet splittings in the ferromagnetic systems.

1.3 Spin Polarized Core Level XPS

Spin polarized core level XPS probes the local electronic and magnetic structure of ferromagnetic systems. The combination of a spin polarimeter with a conventional electron energy analyzer allows the separation of spin-up and spin-down photoelectrons, hopefully providing a wealth of new information.

Compared to conventional XPS, spin polarized XPS has attracted relatively little attention, presumably because of the experimental difficulties of spin analysis. The main limitation of spin polarized photoemission is the inherent inefficiency of spin polarimeters. The efficiency of a typical Mott type low energy spin polarimeter is about 10^{-4}. This means a spectrum which takes one minute in a conventional XPS experiment will require several days to obtain an equivalent signal-to-noise ratio for spin polarized XPS. It is only by employing the highest available photon fluxes from insertion devices operating at synchrotron light sources that spin polarized XPS becomes a versatile experimental tool.

There have been several spin polarized core level experiments providing observations of 3*p* levels of transition metal Fe, Co and Ni,[1.30,1.31] O_2 chemisorption on Fe[1.32] and Co,[1.33] and the Fe 3*s* level.[1.34,1.35] For Fe and Co metals, the spin integrated 3*p* spectra show no multiplet splittings. While for the spin polarized spectra, both the lineshapes and the energies of the spin-up and spin-down 3*p* levels differ drastically. The results for Fe and Co are similar, with a single peak in each spin channel, as shown in figure 1.3.[1.31] In both cases the minority spin (spin-down) feature is narrower and it lies at lower binding energy relative to the majority (spin-up) peak. The linewidth difference between the two spin channels is larger for Fe than for Co.

The spin polarized 3*p* core level spectra of O_2 chemisorbed on Fe[1.34] and Co[1.35] show that when the surfaces become oxidized and no longer ferromagnetic, the differences between the two spin channels disappear correspondingly. This clearly indicates that the significant differences of the spin polarized 3*p* core level spectra linewidths and binding energies between the majority and minority spin channels are due to the ferromagnetism of the system.

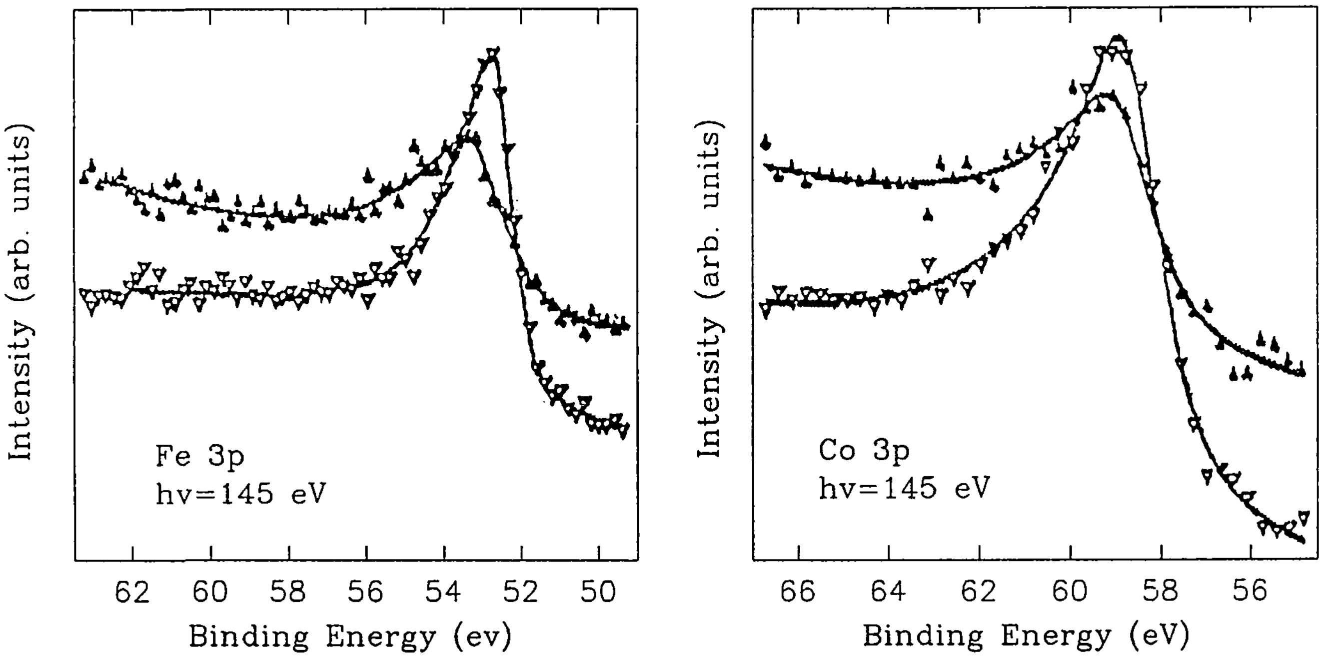

Figure 1.3 Spin polarized 3*p* core level XPS spectra of Fe and Co.[1.31] Open triangles: minority spin curves, solid triangles: majority spin curves.

For the Fe 3*s* core level, Hillebrecht, Jungblut, and Kisker[1.35] presented the spectrum shown in figure 1.4. Figure 1.4 (a) shows the raw experimental data of the spin resolved energy distribution curves. The same data after subtracting flat backgrounds and smoothing the data are shown in figure 1.4 (b). The minority-spin distribution curve has only one peak which is more intense and narrower than the majority-spin peak. The majority-spin peak is at 4.5 eV higher binding energy than the minority peak, and it has a low-binding-energy shoulder which is energetically degenerate with the minority-spin peak. The authors simply compare the total intensities of the minority and the majority spin curves and obtain the ratio $I_{\mathrm{min}}/I_{\mathrm{maj}}$ = 1.16 ± 0.1, concluding that 'the majority-spin weight had been strongly underestimated in the past', and that 'the value is much closer to the intensity ratio of 1 expected for the fully delocalized case'.[1.35]

In principle, if the spin flip effect is negligible during the XPS process, the ratio should be exactly one since the spin of the core electrons is paired off (see appendix 1.1). One reason that Hillebrecht *at el.* underestimate the intensity of the majority spin curve could be that the flat tail caused by the electron configuration interaction was not included. At the fully delocalized limit, the *d* band electrons do not have any atomic structure. The *s* core level electrons then are affected by the average interaction from the *d* band electrons through the configuration interaction. In this case, the ratios given by equations (1.6) and (1.7) are still valid (see appendix 1.1). Therefore, the spectra do not show if the Fe is more itinerant or more localized.

Let us examine the spectra in figure 1.4 again by using the argument which has been discussed above and in appendix 1.1. Within a single configuration, by using $2S = \mu = 2$ Bohr magnetons for Fe, S would equal 1. Substitution of the equations (1.6) and (1.7), one obtains the ratio for two peaks of the majority spin curve R_{maj} = 0.5 and the ratio for two peaks of spin

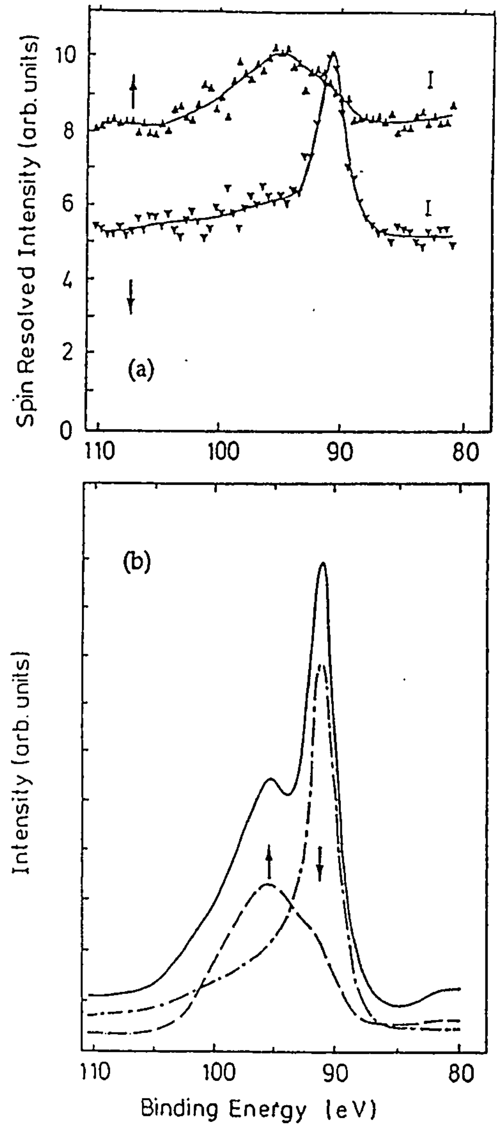

Figure 1.4 Spin polarized 3*s* core level XPS spectra of Fe. (a) raw experimental data, (b) after subtraction of background and averaging over the data points. Solid line is the spin integrated curve.[135]

integrated curve $R_{\text{total}} = 2$. Figure 1.5 shows the spectra generated by the above data with Lorentzian line shapes. The energy splitting of 4.5 eV was chosen based upon experimental observation. Because of the spin conservation, a majority spin core hole will be refilled by a majority spin valence band electron and a minority spin core hole by that of a minority spin electron. The difference between the majority and minority valence electron densities leads to the linewidth difference between the majority and minority peaks. The configuration interaction (or correlation) effects further increase the difference between the majority and minority peaks.[1.36] The linewidth of 2 eV for the minority peak and 3.5 eV for majority peaks were again chosen based upon experimental observation. The results in figure 1.5 agree with the experimental data show in figure 1.4. This indicates that (1) the exchange interaction between the 3*s* core level electrons and the valence electrons is the main cause of the multiplet splitting in the Fe 3*s* XPS spectra, (2) the linewidth difference between the majority and minority peaks are mainly due to the difference between the majority and minority valence electron densities and configuration interaction (or correlation) effects, and (3) the model based on an atomic picture is valid for at least qualitatively describing the spectra.

1.4 Bimetallic Ferromagnetic Systems — Application of Spin Polarized XPS

Spin polarized XPS can be of help in the study of multiple magnetic systems. The spin dependence of the core level spectral distribution is significant and measurable in most ferromagnetic systems. The experimental study of the spin polarized core level XPS can contribute to the fundamental understanding

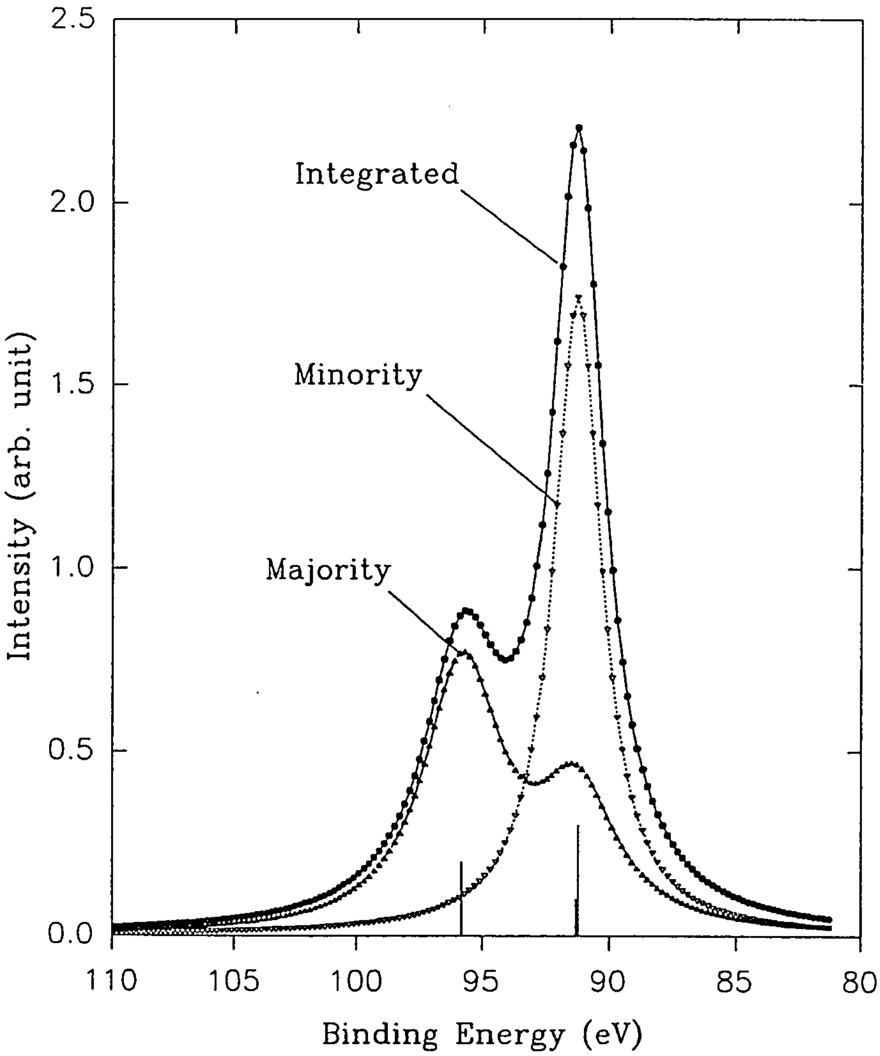

Figure 1.5 Calculated spin polarized 3*s* core level XPS spectra of Fe. Dashed (solid) lines show minority (majority) spectra lines.

of the spin dependent core level photoexcitation, electron scattering and diffraction. Moreover, spin polarized core level spectroscopy appears very promising as a new method both for its surface sensitivity and its element specificity, to probe the ferromagnetic ordering in surfaces, interfaces and thin films.

For a bimetallic system, emission from the valence states often overlap, and it is difficult to disentangle the contributions from different species to obtain electronic information for a particular element. Since atoms of different species have different characteristic core level electron binding energies which are sensitive to the local-charge environments, the core level XPS spectra yield significant information about the local chemical environment of the particular species. For multiple ferromagnetic systems, spin polarized valence band photoemission spectroscopy usually provides averaged magnetic information. By the same argument, spin polarized core level XPS can be a powerful tool to probe the local electric and magnetic properties of different species in a complex ferromagnetic system.

An example is the study of the magnetic properties of Cr overlayers on Fe. The nearly half-filled 3*d* band of Cr produces unique electronic and magnetic properties in the bulk metal. Neutron diffraction studies[1.37] show that the bulk Cr is in the body-centered-cubic (bcc) structure with an antiferromagnetic ground state modulated by an incommensurate spin-density wave with a local magnetic moment of $\mu = 0.59$ Bohr magnetons (μ_B). There is a spin-density wave in each of the (100)-type directions with a wavelength of approximately 21 times the side of the unit cube. In this structure, atoms in the body-centered positions of the bcc lattice have spins pointing only in one direction, while atoms in the corner positions have spins in the opposite direction. Consequently, the simple antiferromagnetic structure of Cr demands that the (100) surface possess ferromagnetic order.

Self-consistent calculations[1.38-40] show that a Cr monolayer on ferromagnetic Fe(100) surface is ferromagnetic within the layer, with a magnetic moment of $\mu = 3.63\ \mu_B$. The Cr layer is aligned antiferromagnetically with respect to the Fe substrate. Such a huge polarization is caused by two effects: the Cr(100) surface band narrowing and the strong antiferromagnetic Fe-Cr interaction. The former effect can be attributed to the large number of unpolarized *d* holes present in Cr bulk. Consequently, the decreased bandwidth of the Cr surface, which leads to a stronger effective magnetic interaction, can greatly increase the surface spin polarization. Elements like Fe or Ni, with fewer available unpolarized holes, experience smaller changes in the same local environment.

Spin polarized XPS experiments should be able to recognize if an atomic element of the system is ferromagnetically aligned by its self, and how it couples magnetically respect to the other ferromagnetic elements. Jungblut *et al.*[1.41] have performed spin polarized 3*p* core level XPS studies of Cr overlayers deposited on an Fe(100) surface. However, the only 3*p* core level XPS data shown in the paper is with 2.2 Å Cr on Fe, which is equivalent to 1.6 monolayers (the thickness of one monolayer for Cr is 1.44 Å). If the first layer of Cr is ferromagnetically ordered and aligned antiferromagnetically with respect to the Fe substrate, the second layer of Cr will be aligned ferromagnetically with respect to the Fe substrate.[1.42] So the polarization of the first monolayer will be reduced by that of the other 0.6 monolayers Cr on the top by a factor of 4 (the mean free path of $\lambda = 5$ Å was used). Unfortunately, the authors also use an incorrect argument based on the 'integral polarization' of the Cr 3*p* core level spectra, i.e. $P_{\text{total}} = (I_{\text{maj}} - I_{\text{min}})/(I_{\text{maj}} + I_{\text{min}})$. They claim the polarization to be 13% and opposite to the Fe 3*p* polarization. It is a basic physics principle that $P_{\text{total}} = 0$

since the spins of the 3*p* core level electrons are fully paired off and cancel each other out, as was discussed earlier.

Chapter 2. X1B Soft X-ray Beamline

Part of the work presented in this chapter is based on the paper published in Rev. Sci. Instrum. 63, 1367 (1992) in collaboration with K. J. Randall et al.

2.1 Introduction

The efficiency of a typical electron-spin polarimeter is about 10^{-4}. This low efficiency would prolong the acquisition time for a spin polarized photoemission spectrum by a factor of 10^4 for a signal-to-noise ratio equivalent to that of a normal photoemission spectrum. Long acquisition times make it virtually impossible to do any surface or thin film studies, since the samples would become significantly contaminated in such a long time. This difficulty can be overcome by increasing the intensity of the photon source.

Spin polarized XPS can be improved with extremely intense, tunable and highly monochromatized x-ray photon sources. The 2*p*, 3s, and 3p level electron binding energies for 3d transition metals range from 870 eV for Ni 2*p* to 28 eV for Sc 3*p*, so the soft x-ray region with photon energy from 200 eV to 900 eV is of primary interest. Figure 2.1 shows some of the world's brightest synchrotron radiation sources. The solid lines represent the sources already available and the broken lines represent the sources still being constructed. According to the figure, it is clear that beamline X1 at the NSLS of Brookhaven National Laboratory provides the world's brightest soft x-ray radiation source and it covers the spectral region of most interest.

X1 is an undulator based synchrotron radiation source.[2.1,2.2] The undulator is a magnet/steel hybrid device, made of samarium/cobalt. It has 35 periods, each of which partially contributes radiation to the photon flux to the beam

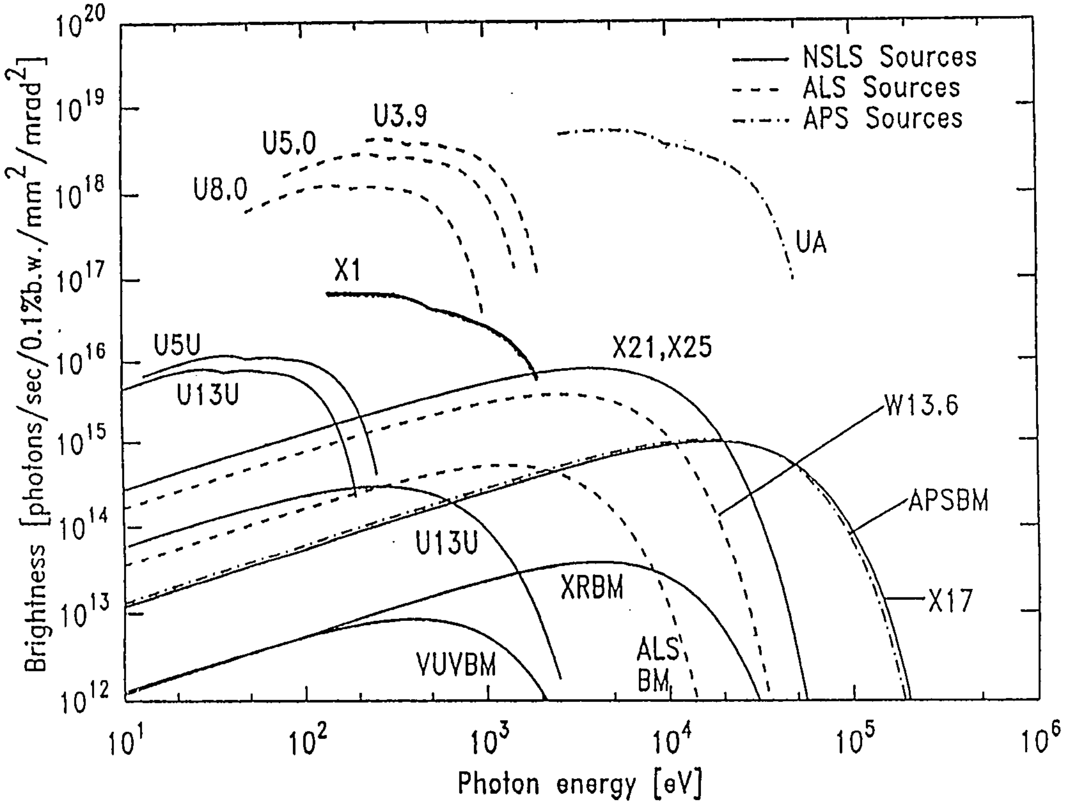

Figure 2.1 Comparison of synchrotron radiation sources. The broken lines are under construction. The solid lines are available. NSLS: National Synchrotron Lingt Source, ALS: Advanced Light Source, APS: Advanced Photon Source.

which is well collimated. Therefore, the flux of the source is orders higher than that of a conventional bending magnet type. The undulator is installed at the X1 straight section of the NSLS x-ring. The tunable photon energy range of the undulator's first harmonic covers the energy range of 200-700 eV with the variable gap of 32 – 98 mm. The maximum radiated power can reach 267 W at 170 eV with the nominal storage ring energy of 2.5 GeV and current of 200 mA. It has a central intensity of more than 10^{15} photons/(s, mm^2, $mrad^2$, 0.1%BW) at $h\nu$ = 345 eV. The undulator offers considerable advantages: First, the spectral flux from an undulator, integrated over the central cone, is typically a factor of 10 higher than the flux from 10 mrad of a bending magnet source. Secondly, the undulator source can be matched to the monochromator more efficiently because of the inherently higher spectral brilliance.

Installation of the spectroscopy beamline (X1B) was completed in 1991. The monochromator, based on the Dragon Beamline (Brookhaven UV ring) concept[2.3,2.4] has a spherical grating and a movable exit slit. The two pre-focusing mirrors, the entrance slit, and the grating are water-cooled in order to handle up to 400 W.[2.5] At a resolving power of approximately 5000 at 400 eV photon energy, more than 10^{11} photons/sec have been measured in ~ 1 mm^2 focus. The X1B beamline represents one of the next generation of the soft x-ray undulator beamlines which will be developed at new synchrotron radiation facilities such as ALS, BESSY II and ELETTRA. It is ideal for the spin-polarized core level XPS studies as well as all kinds of other photoionization-based experiments.

2.2 Design Considerations and Layout of X1B Beamline

The most important requirements for a soft x-ray monochromator on a spectroscopy beamline are high intensity and high resolution. Dealing with hundreds of watts of power in a narrow beam in ultra-high vacuum demands that all surfaces potentially exposed to the white beam be water-cooled. This is especially true for those elements which form part of the optical design and which need to retain their position and shape to a high degree of accuracy. In principle, the simpler the geometry of the monochromator is, the better. C. T. Chen's cylindrical element monochromator[2.3,2.4] (CEM) has only three reflecting elements: a cylindrical horizontal focusing mirror (HFM), a cylindrical vertical focusing mirror (VFM) and a spherical grating with a fixed entrance slit and a movable exit slit. The resolution of the system is mainly determined by the slope error of the grating. Practically speaking, it is much easier to reach higher optical figure quality for simple surface geometries such as planar, cylindrical and spherical ones. The movable exit slit further enables the CEM to obtain a better focusing condition, and thus higher resolution, than toroidal grating monochromators (TGM). Therefore, we have chosen the CEM for it combines both high resolution and high transmission.

Figure 2.2 shows the layout of the X1B monochromator. The first mirror, the horizontally focusing cylindrical mirror (HFM), focuses the source onto the sample in the experimental chamber, reducing the photon beam width in size by a factor of 0.8. Ignoring aberrations, this horizontal focusing gives an image size of approximately 0.7 mm (FWHM) at the sample position. The image actually observed on a phosphor screen at the sample position has relatively sharp edges and is estimated to be 1 to 1.5 mm wide. This image can be tolerated in the spin-polarized XPS experiments since the focal point of the analyzer entrance lens is about the same size. The additional broadening is probably due to the thermally induced distortion of aluminum mirror, since it quantitatively agree with results of finite element calculations carried out by Hulbert and Sharma[2.6]. The HFM absorbs most of the power radiated by the undulator, thus protecting the more

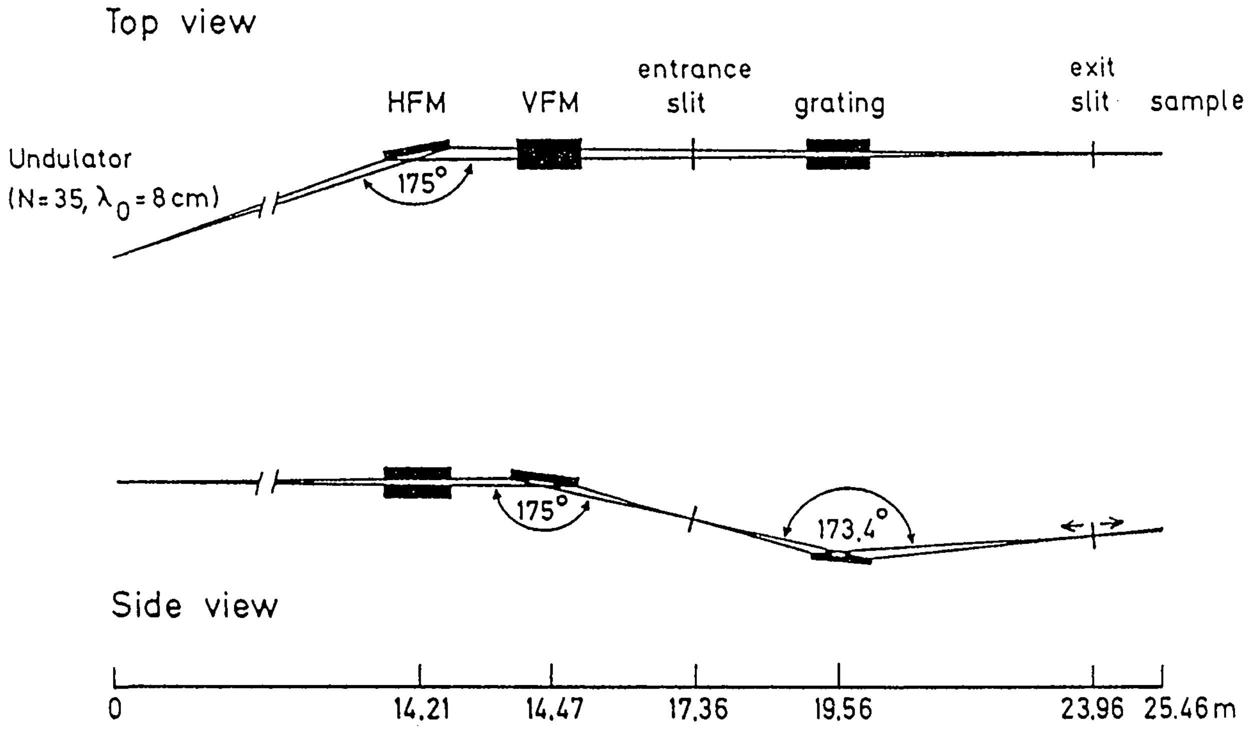

Figure 2.2 Lay out of X1B monochromator.

critical optical elements downstream such as the grating. It also deflects the beam horizontally into the X1B beamline. The second mirror, the vertically focusing cylindrical mirror (VFM), focuses the undulator radiation vertically onto the water-cooled entrance slit. With a 5:1 demagnification, the image size at the slit is approximately 5 to 10 μm (FWHM) in height, giving the maximum transmission efficiency at the same entrance slit settings, but increasing the vertical divergence by factor of 5 to 300 μrad (RMS half width). For near-to-grazing angles of incidence onto a spherical grating, at a photon energy of ~ 200 eV, a vertical divergence less than 100 μrad is expected to under-illuminate the grating to such an extent that the resolution would be diffraction limited. At the other extreme, a vertical divergence greater than 500 μrad would over-illuminate the grating and the resolution would then be aberration limited.

Both mirrors have been manufactured from aluminum by Zeiss (Oberkochen, Germany) and coated with Kanigen and gold: Each is water-cooled and mounted with five independent degrees of freedom controlled by stepper motors via vacuum bellows for *in situ* adjustment (two linear motions, pitch, roll and yaw).

The entrance slit is also water-cooled for better stability. The monochromator will eventually have a grating exchange mechanism, which will allow up to three gratings to be installed. At present, the single 800 line/mm grating is in a water-cooled mounting to minimize distortions. The grating was mechanically ruled with a 1.5 degree blazing angle in Au on a spherical fused silica blank by Hyperfine Inc. (Boulder, Colorado, USA). The exit slit position is adjustable along the beamline to meet the focusing condition and to maintain the best resolution during a wavelength scan. The exit slit is not water-cooled because the power load after the grating is much less than at the entrance slit.

After the exit slit, the beam diverges vertically, resulting in a spot at the sample position of less than a square millimeter in size.

The basic theory of diffraction gratings[2.7-9] combined with the special properties of the CEM result in four main terms in the resolution limitation:

(1) aberration (coma only)

$$\frac{\Delta\lambda_a}{\lambda}=\frac{1.8C_{30}(L/2)^2}{Nk\lambda}, \tag{2.1}$$

(2) entrance slit

$$\frac{\Delta\lambda_i}{\lambda}=\frac{s_1\cos\alpha}{r_1Nk\lambda}, \tag{2.2}$$

(3) exit slit

$$\frac{\Delta\lambda_f}{\lambda}=\frac{s_2\cos\beta}{r_2Nk\lambda}, \tag{2.3}$$

and, (4) figure slope error

$$\frac{\Delta\lambda_e}{\lambda}=2\sigma'_{err}\cot\phi, \tag{2.4}$$

where

$$C_{30}=\frac{\sin\alpha}{2r_1}\left(\frac{\cos^2\alpha}{r_1}-\frac{\cos\alpha}{R}\right)+\frac{\sin\beta}{2r_2}\left(\frac{\cos^2\beta}{r_2}-\frac{\cos\beta}{R}\right), \tag{2.5}$$

$$\alpha=\phi+\theta, \tag{2.6}$$

$$\beta=\phi-\theta, \tag{2.7}$$

$$\phi=\sin^{-1}\left(\frac{Nk\lambda}{2\cos\theta}\right). \tag{2.8}$$

C_{30} is the coma coefficient in the grating path function. L, R and σ'_{err} are the length of the illuminated area, the radius and the rms figure slope error of grating respectively. r_1, r_2 and s_1, s_2 are the entrance, exit focal lengths and slit openings respectively. α and β are the incident and outgoing angles relative to the normal of the grating. N, k and λ are the groove density, order of diffraction and the wavelength. ϕ and θ are the scanning angle and the zeroth order incident angle of the grating. For the total resolution limit we simply take the vector sum of these four contributions.

There is another parameter C_{20} in the grating path function representing the defocus coefficient:

$$C_{20} = \frac{1}{2}\left[\frac{\cos^2\alpha}{r_1} + \frac{\cos^2\beta}{r_2} - \frac{\cos\alpha + \cos\beta}{R}\right]. \tag{2.9}$$

The exit slit position r_2 is determined by letting the defocus coefficient $C_{20} = 0$, giving:

$$r_2 = \frac{\cos^2\beta}{\left(\dfrac{\cos\alpha + \cos\beta}{R} - \dfrac{\cos^2\alpha}{r_1}\right)}. \tag{2.10}$$

The calculated spectral resolution for the X1B monochromator is shown in figure 2.3 as a function of photon energy. The individual contributions of coma, the entrance and exit slits and the slope error are indicated. Not shown in this figure is the contribution due to the diffraction limit which has been included in the 'total' curve. In the calculation, the entrance and exit slits are both set at 5 μm. The slope error is chosen to be 0.5 arc sec, the grating groove density is 800 line/mm, and the vertical divergence is chosen to be 300 μrad (rms) for the 'total' resolution limit curve. If the nominal slope error of 0.5 arc sec for the spherical grating can be acquired, a resolution E/ΔE of ~ 8×10^3 at the N *K* edge and > 1×10^4 at the C *K* edge would become possible. As will be shown below, there is a strong possibility that the above calculated resolution can actually be obtained. We also note from the model calculations depicted in figure 2.3 that for 5 μm entrance and exit slit settings, the slope error effectively determines the

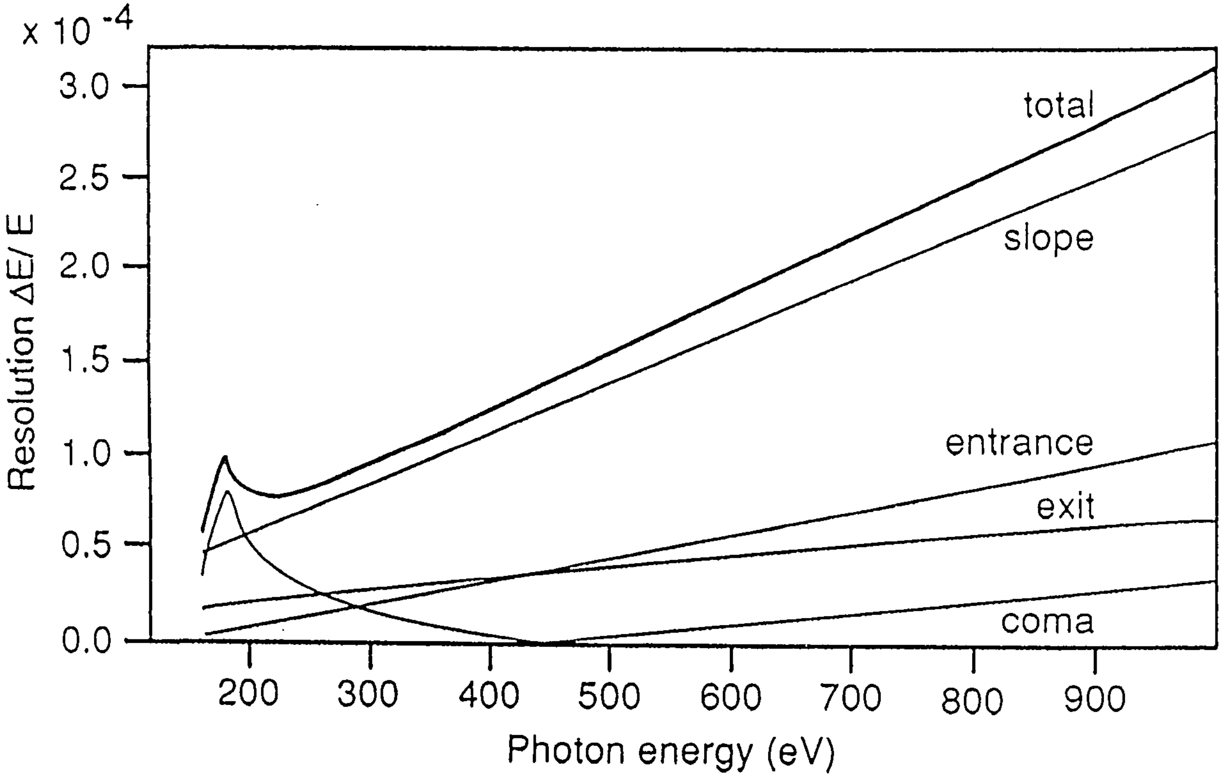

Figure 2.3 Calculated resolution of X1B monochromator as a function of photon energy for exit and entrance slits of width 5 μm, 0.5 arc sec slope error on the 800 l/mm spherical grating and vertical divergence of 300 μrad (σ). Also shown are the contributions to the total resolution from coma, slit width, and the slope error.

resolution. For 10 μm slit settings (not shown) the contribution of each of the other parameters is of the same order of magnitude as that of the slits.

2.3 Testing and Commissioning of X1B Beamline

The flux measurements at the exit slit of the X1B monochromator have been conducted by using a Hamamatsu GaAsP diode as well as a calibrated (oxidized) aluminum photo diode, the latter having previously been used at Brookhaven.[2.10] At 400 eV, with 20 μm entrance and exit slit settings, the GaAsP diode gives a value of ~ 1×10^{11} photons per second and the aluminum photo diode of ~ 4×10^{11} photons per second. With the same slit settings, it gives a spectral resolution of ~ 80 meV, similar to that measured on the Dragon beamline (i.e. beamline U4B at the NSLS, BNL) under the optimal conditions at that time (The N1*s* to π_g* transition in the core level photoabsorption spectrum of N_2). In order to relate these figures to monochromators on bending magnets, we note that 1×10^{11} is a typical value measured with the same GaAsP diode at the exit slit of beamline HE-TGM 1 at BESSY where the resolution is only about 1 eV at 400 eV photon energy.

The C1*s* to π* transition in the core level photoabsorption spectrum of CO is shown in figure 2.4. The spectrum was measured directly in absorption using a GaAsP diode as the detector. The gas cell was 25 cm long and filled to a pressure of ~ 10 mTorr. Both entrance and exit slits were set for maximum resolution at 5 μm. The total measuring time was 5 minutes. The energy scale was calibrated with reference to the electron energy loss spectroscopy (EELS) data of Tronc *et al.*[2.11] The vibrational structure is clearly resolved in the spectrum of figure 2.4. The separation between the $v' = 0$ and $v' = 1$ lines is 250 meV, in agreement with the analysis of Domke *et al.*[2.11] The instrumental

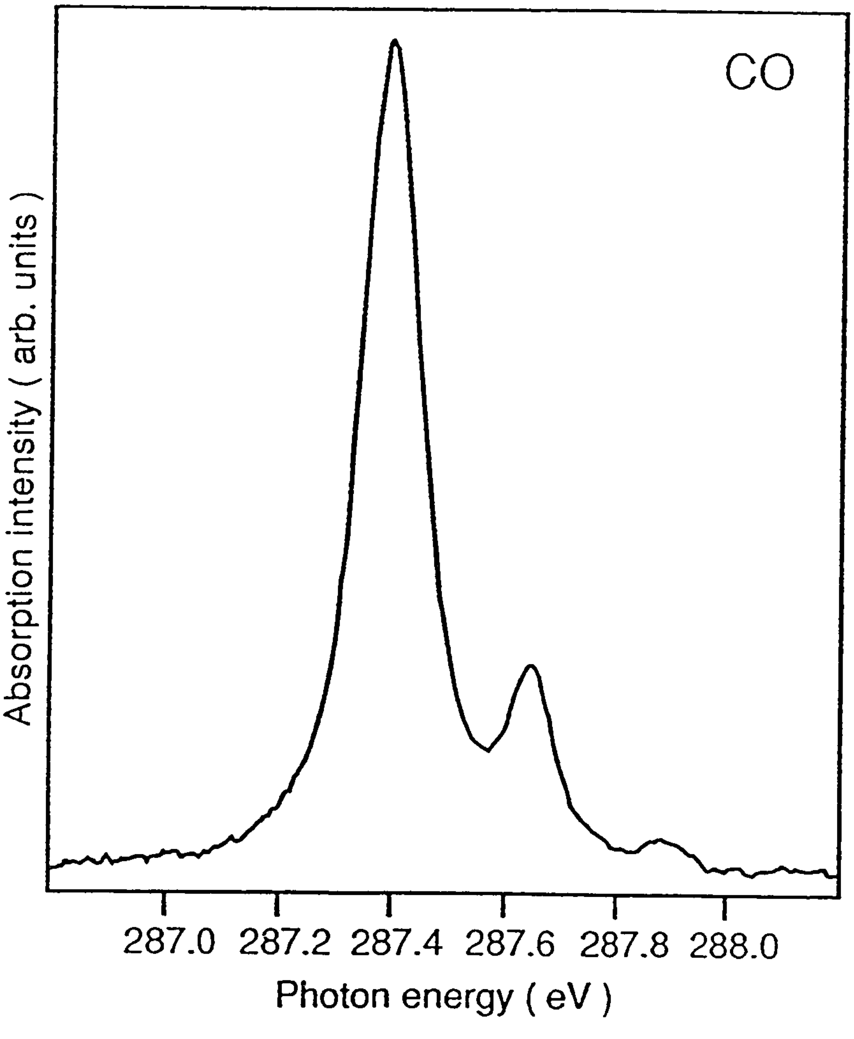

Figure 2.4 Photoabsorption spectrum of core level C1*s* to π* transition from CO.

resolution is undoubtedly better (higher peak-to-valley ratio) than in the latter paper where a value of 80 meV is given.

The absorption spectrum of N1*s* to π_g* transition in the core level photoabsorption for N_2 taken under the same conditions is shown in figure 2.5. The energy scale was calibrated via the *v*' = 1 line in the EELS spectrum of Tronc *et al.*[2.12] Because of the pronounced vibrational fine structure, it is impossible to give a value here for the as-measured linewidth without deconvolution. Chen and Sette[2.4] have shown that such a 'deconvolution' can be performed entirely with Lorentzian lineshapes, which they interpreted as resulting from a very small contribution from instrumental (Gaussian) broadening. The resolution of the Dragon monochromator at this photon energy is estimated to be lower than 40 meV based on a comparison with EELS data. While this cannot necessarily be accepted as a definitive value, Chen and Sette do propose useful criteria for determining the comparative resolution of soft x-ray monochromators. They took the first valley to third peak ratio in the N1*s* to π_g* photoabsorption spectrum for N_2 (at 400.95 eV and 401.31 eV, respectively) which matched the EELS data for 70 meV instrumental resolution.[2.13] They obtained a value of ~ 0.85 for the Dragon monochromator. Approximately the same value was obtained on the SX-700 II in second order (resolution ~ 74 meV at 400 eV in second order).[2.14] The value obtained on X1B shown in figure 2.5 is 0.73. This is a clear indication of significant increase in spectral resolution as compared to the two bending magnet monochromators. A conservative estimate at this stage would therefore place the absolute value of spectral resolution on X1B significantly below 70 meV at 400 eV.

Additional evidence of an improvement in resolution can be observed by comparing the spectrum of O1*s* to Rydberg region of the photoabsorption spectrum of O_2. The individual transitions have been assigned by Ma *et al.*[2.15]

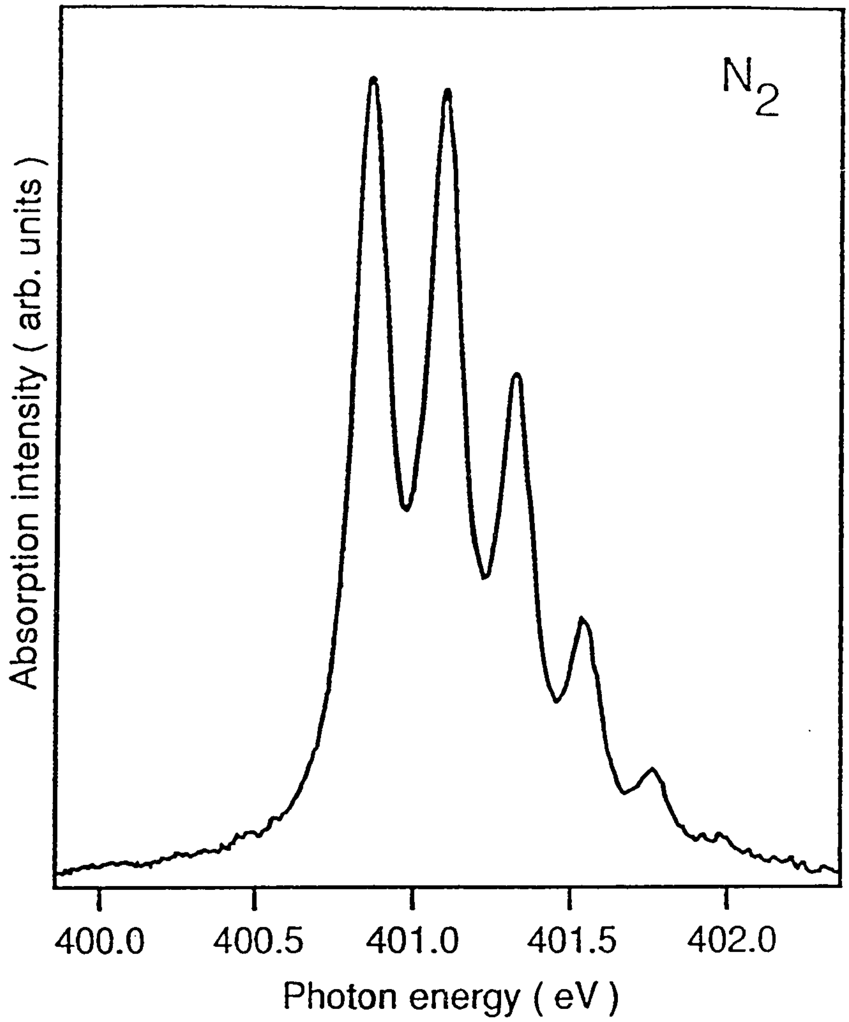

Figure 2.5 Photoabsorption spectrum of core level N1*s* to π_g* transition from N_2.

The spectra shown in figure 2.6 (a) and (b) were taken on the Dragon beamline. Spectrum (b) is a magnified view of Rydberg region enclosed by a dashed line in spectrum (a). The spectrum in figure 2.6 (c) was taken on X1B. The photon energy scale has been calibrated with reference to EELS data of Hitchcock and Brion.[2.16] It is not difficult to see the improvement in resolution by comparing two spectra shown in figure 2.6 (b) from the Dragon and figure 2.6 (c) from X1B. An oxygen spectrum with similar resolution has recently been measured on the SX700-II monochromator at BESSY in 3rd diffraction order and using only 5% of the ellipsoidal mirror. Under the same conditions, however, the photon flux is several orders of magnitude lower than that of X1B. Furthermore, the absorption spectrum is rather noisy so that any other type of spectroscopy would certainly be difficult, if not impossible.

A comparison of the X1B spectra with the corresponding spectra from the Dragon beamline and the beamline SX-700 II suggests that the resolution on X1B is significantly higher. As expected, the flux is at least a factor of 10 higher than that of similar monochromators installed on bending magnets and operating at comparable resolution. During the commissioning of X1B, we successively carried out a variety of experiments in atomic and molecular physics[2.17,2.18] as well as in surface and solid state physics. The results demonstrated that the high flux, high resolution soft x-ray source of X1B would allow previously difficult experiments, such as spin polarized XPS, to be performed with greater ease.

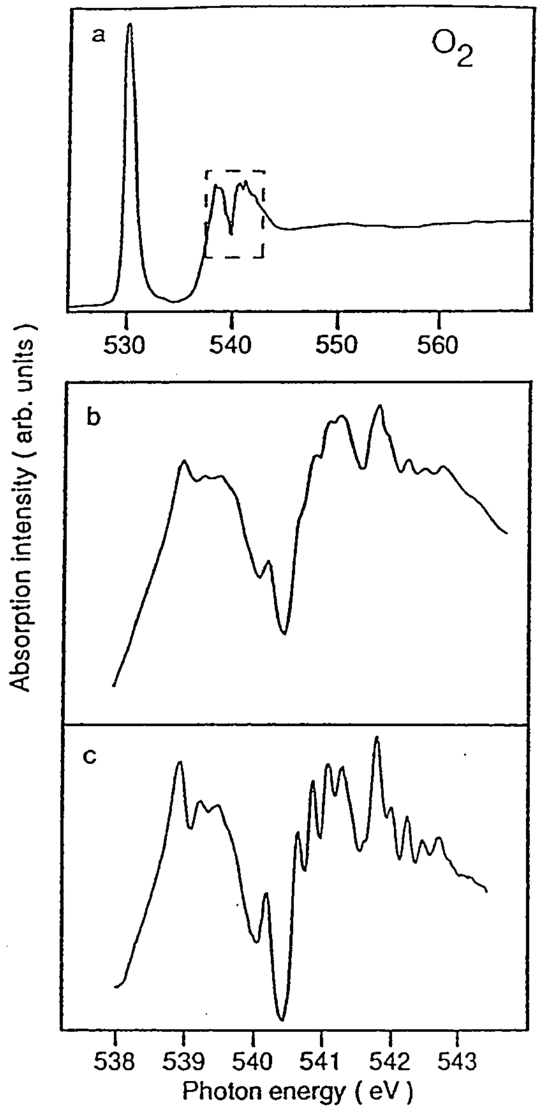

Figure 2.6 Photoabsorption spectrum of O1*s* to Rydberg transition from O_2. (a) overview spectrum from Ref. 2.15. (b) The expanded Rydberg region also from Ref. 2.15. (c) Same region as (b) taken on the X1B monochromator.

Chapter 3. Electron-spin Polarization Analyzer

3.1 Introduction

Mott[3.1,3.2] pointed out that the uncertainty principle, together with the Lorentz force, prevents spin-up and spin-down electrons from being separated by a macroscopic field of the Stern-Gerlach type. Although many attempts have been made to disprove Mott's argument, all efforts toward modifying the experiment to make it work have failed

This does not mean that polarized free electrons cannot be produced or detected. Instead, Mott[3.1] proposed that the electron spin could be detected in a double scattering experiment, which is schematically illustrated in figure 3.1. Here a beam of unpolarized electrons is initially scattered from high-Z nuclei in a target surface or foil. Because of the spin-orbit interaction, large angle $(\theta_1 \geq 90^\circ)$ scattering from the first target produces electrons with a significant spin polarization transverse to the scattering plane. The scattering of these polarized electrons from the second target yields a left-right scattering asymmetry, again due to the spin-orbit interaction, that is proportional to the polarization induced by the first scattering.

If an electron is scattered by a bare nucleus of charge *Ze*. The motion of the electron in the electric field **E** of the nucleus yields a magnetic field **B** in the electron's rest frame. The interaction of this magnetic field with the electron spin magnetic moment μ_s introduces a term $U_{so} = -\mu_s \cdot \mathbf{B}$ to the scattering potential. The electron magnetic moment is related to the electron spin **s**. From the basic theory of relativistic quantum mechanics, we can then write

$$U_{so} \propto \frac{Z}{r^3}(s \cdot l) \qquad (3.1)$$

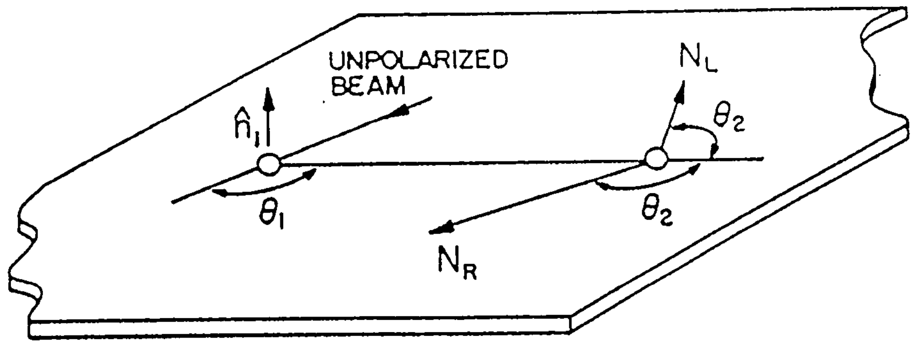

Figure 3.1 Schematic diagram of a double scattering experiment.

Therefore, the spin-orbit interaction corresponds to an additional scattering potential. The sign of the potential depends on whether the electron with spin-up or spin-down passes the scattering center on the right or on the left. This is shown in figure 3.2. The curve 'no spin' corresponds to the bare Coulomb potential. For transversally polarized electrons, if the scattering potential is spin-dependent, the differential cross section then will be different for spin-up and spin-down electrons. Figure 3.3 shows an experimental measurement of the elastic scattering from Hg atoms. The differential cross section $\sigma(\theta)$ as a function of the scattering angle θ has some structure, determined by λ/R where R is the effective range of the potential and λ is the electron wavelength. For a given scattering angle, the effective range depends on the sign and magnitude of the spin-orbit interaction. However, the scattering cross sections are slightly shifted with respect to each other on the θ axis. We define the asymmetry function $S(\theta)$ by

$$S(\theta)=\frac{\sigma^{\uparrow}(\theta)-\sigma^{\downarrow}(\theta)}{\sigma^{\uparrow}(\theta)+\sigma^{\downarrow}(\theta)} \tag{3.2}$$

i.e. the normalized difference of spin-up and spin-down intensities at a given scattering angle θ.

A point of clarification is needed here concerning the directions of the spin. Whenever we use the terms 'spin-up' and 'spin-down', or later 'majority spin' and the 'minority spin', we do not really mean that the direction of the electron spin angular momentum is 'up' or 'down'. Practically, the term 'spin-up' or 'majority spin' ('spin-down' or 'minority spin') means that the spin magnetic moment component is parallel (anti-parallel) to some quantization axis, usually the direction of the applied external magnetic field.

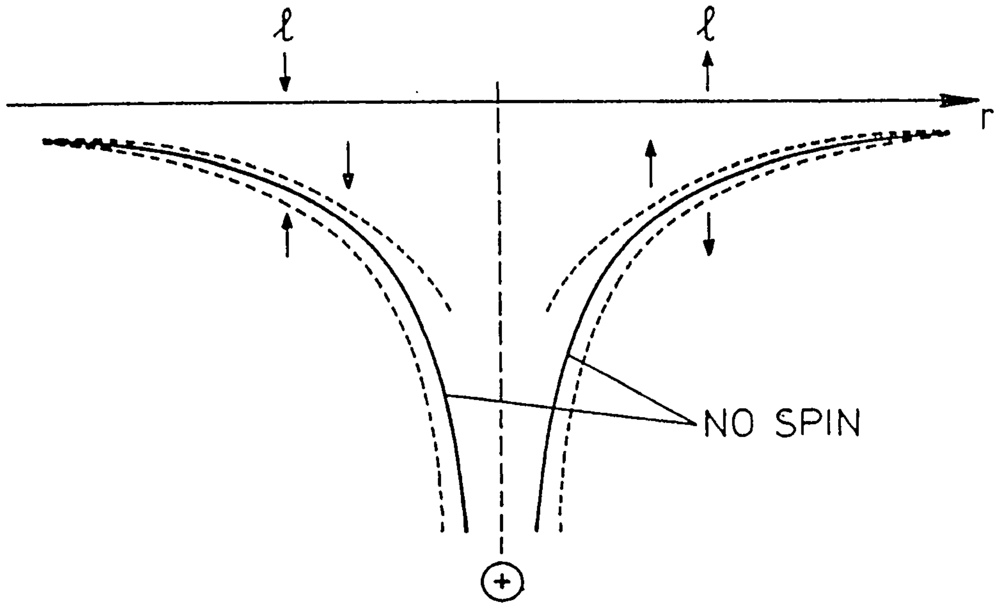

Figure 3.2 Potential curves for electrons with different spins normal to the scattering plane. The solid lines are for electrons without spin-orbit coupling.

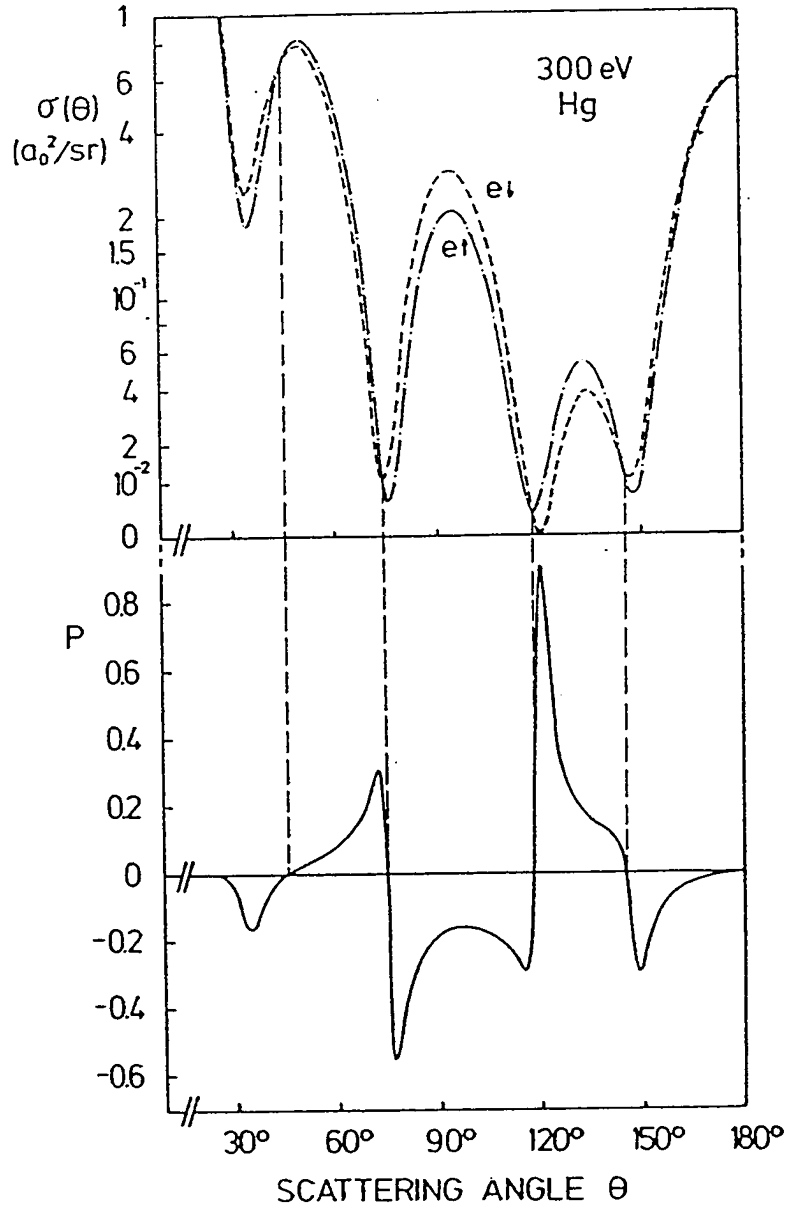

Figure 3.3 Calculated differential scattering cross sections and polarization for completely polarized electrons scattered elastically from free Hg atoms at 300 eV.[3.2]

Considering the symmetry in figure 3.3, or the definition of the asymmetry function $S(\theta)$, one can immediately conclude that the asymmetry function $S(\theta)$ is asymmetric itself, i.e.

$$S(-\theta) = -S(\theta) \tag{3.3}$$

This is very important because as a consequence, the polarization of an electron beam can be determined using spin-orbit coupling by two measurements of the intensity for complementary angles.

The asymmetry function $S(\theta)$ is defined as the normalized difference of the scattering cross sections. Therefore, for elastic scattering, it can be expressed by means of scattering amplitudes.

$$\sigma(\theta,\phi) = I(\theta)\left[1+S(\theta)\sin(\phi)\right] = I(\theta)\left[1+\boldsymbol{P}(\theta)\cdot\boldsymbol{n}\right]. \tag{3.4}$$

So the polarization of the electrons after scattering is

$$\boldsymbol{P}(\theta) = S(\theta)\sin(\phi) = S(\theta)\boldsymbol{n} \tag{3.5}$$

where $\boldsymbol{n} = \dfrac{\boldsymbol{k}\times\boldsymbol{k}'}{|\boldsymbol{k}|^2\times|\boldsymbol{k}'|^2}$, is the normal to the scattering plane and $\boldsymbol{k}$ and $\boldsymbol{k}'$ are the wavevectors of the primary and scattered electrons respectively. Equation (3.5) is important for two reasons. First, it shows that an unpolarized electron beam is polarized by scattering due to spin-orbit coupling. The polarization vector is normal to the scattering plane. Second, it shows that, for an unpolarized beam, after scattering, the polarization P has the same intensity as the asymmetry S, which is obtained when scattering a polarized electron beam with P normal to the scattering plane.

Furthermore, because the first scattering is to the left of the normal $\boldsymbol{n}$ of the scattering plane as shown in figure 3.1, the unpolarized incident electron beam can be considered as being comprised of equal numbers of electrons with spin parallel and antiparallel to $\boldsymbol{n}$, i.e. with spin-up (m_s = +1/2) and spin-down

($m_s = -1/2$). From equation 3.4 it follows that the number $N_\uparrow$ of spin-up electrons scattered (to the left) through angle θ_1 is proportional to $1 + S(\theta_1)$, and the number $N_\downarrow$ of scattered spin-down electrons is proportional to $1 - S(\theta_1)$. Thus electrons scattered through θ_1 have a net polarization $P(\theta_1)$ given by

$$P(\theta_1) = \frac{N_\uparrow - N_\downarrow}{N_\uparrow + N_\downarrow} = S(\theta_1), \tag{3.6}$$

or, in vector notation, by equation 3.5. Scattering of these polarized electrons from a second target yields a left-right scattering asymmetry $A(\theta_2)$ defined as

$$A(\theta_2) = \frac{N_\mathrm{L} - N_\mathrm{R}}{N_\mathrm{L} + N_\mathrm{R}}, \tag{3.7}$$

where N_L and N_R are the number of electrons scattered to the left and right, respectively, through an angle θ_2. If the first and second scattering events are coplanar, N_L will be proportional to $N_\uparrow[1 + S(\theta_2)] + N_\downarrow[1 - S(\theta_2)]$, and N_R will be proportional to $N_\uparrow[1 - S(\theta_2)] + N_\downarrow[1 + S(\theta_2)]$.

For the coplanar scattering case, substitution in equation 3.6 yields

$$A(\theta_2) = P(\theta_1)S(\theta_2), \tag{3.8}$$

or

$$P = \frac{1}{S}A = \frac{1}{S}\frac{N_\mathrm{L} - N_\mathrm{R}}{N_\mathrm{L} + N_\mathrm{R}}. \tag{3.9}$$

Equation 3.9 is the basis of the electron-spin polarization analyzer. If S i.e. the Sherman function is known, measurement of the scattering asymmetry A yields P, i.e., the component of the incident beam polarization perpendicular to the scattering plane.

The spin dependent scattering asymmetry experiment was first proposed by Mott[3.1] in 1929. It was not until 1942 that Schull, *et al.*[3.3] demonstrated the existence of a scattering asymmetry which was in agreement with Mott's calculations. Since then the Mott scattering studies have been used to the production and measurement of electron polarization in various fields of physics.[3.2]

3.2 Review of Existing Electron Spin Polarimeters

Electron spin polarimeters are used in many different applications. There is no single type of spin polarimeter that possesses all characteristics required for every application. Two aspects are particularly important in quantifying the characteristics of an electron spin polarimeter. They are the figure of merit, and the electron optical acceptance. The figure of merit is defined as S^2I/I_0, where S is the Sherman function, I and I_0 is the detected and primary incident electron intensities respectively

. Clearly it is best to have the analyzing power (or the Sherman function) S to be as large as possible. The ratio I/I_0 is also to be optimized. The second measure of a polarimeter is the electron optical acceptance. The spin polarimeter's electron optical acceptance should be matched to (i.e., greater than or equal to) the emittance or phase space product of the electron beam to be measured in order to avoid loss of signal. According to the law of Helmholz and Lagrange, at any two points, 1 and 2, along a beam path, the phase-space product is conserved:

$$E_1 dA_1 d\Omega_1 = E_2 dA_2 d\Omega_2 \tag{3.10}$$

where E is the electron kinetic energy, dA is the cross-section of the electron beam, and $d\Omega$ is the solid angle. So a large electron optical acceptance, i.e., a large acceptable phase-space product, is a desirable property of the polarimeter. Other considerations such as the size of the polarimeter, which is usually related to the operating energy, can also be an important factor. The vacuum requirements of the polarimeter and the experimental region should also be compatible, although differential pumping stage can be used to compensate for significant pressure differences. The long and short-term stability of the spin polarimeter and its calibration are factors which may be strongly related to the vacuum environment. Also, there is the question of the calibration. Some spin polarimeters are self-calibrating while others require calibration against another type of polarimeter. Finally, the simplicity and the cost of the polarimeter also need to be considered.

The traditional and most widely used means of measuring electron spin polarization is the Mott polarimeter. A typical Mott detector[3.4] operates at 100-120 keV and measures the back scattered electron intensities at ± 120° from a thin gold foil target. The analyzing power S of the foil is calibrated by measuring the asymmetry for a number of foil thicknesses and extrapolating to zero foil thickness where, from reliable calculations for 100 keV electron scattering from Au nuclei, $S = 0.39$. The value of S is reduced by multiple scattering in thicker foils but the scattering intensity is increased. A reasonable agreement is reached when the value of S ranges from 0.2 to 0.3. The thin Au foils are not opaque to the high energy electrons. Typically, only 10^{-3} to 10^{-4} of the incident electrons are scattered back into the counters.

Low-energy Mott polarimeters based on the spin-orbit scattering of electrons from a Hg atomic beam have also been used. Since the Hg beam is a low-density target resulting a low scattering efficiency, a figure of merit of 4×10^{-5} has been achieved and it has been suggested that increases of the figure of merit are possible with a higher density Hg beam.[3.5] Such a spin polarimeter requires only moderate vacuum and is good for some electron atom scattering experiments.

Some of the Mott polarimeter uses two electrodes, one sitting inside the other. The electrons are accelerated to the inner electrode and scattered from the Au foil at high energy, and are then decelerated as they pass again to the outer electrode which is nominally at ground potential. This accelerating/decelerating type of polarimeter is usually in a cylindrical[3.6] or spherical geometry.[3.7,3.8] This kind of polarimeter has the advantages that the inelastically scattered electrons are automatically discriminated through the decelerating process and that the scattered electron detectors are operated at ground potential. The chamber is also at ground potential. This type of Mott polarimeter in spherical geometry has operated effectively in the 20 keV — 40 keV range with a figure of merit of 2×10^{-5}. Because of its relatively small size for a Mott polarimeter, it has been called the 'Mini Mott.'

When scattering takes place at low energy from a single crystal, electrons are diffracted back into well defined beams. The left-right asymmetry of the scattering, which is again due to the spin-orbit interaction, has also been used in developing a spin polarimeter.[3.9] This polarized low-energy electron diffraction (PLEED) polarimeter is different from those described above in three important respects: (1) the target is a single crystal and is opaque to the electrons, (2) the target, a W single crystal, can be automatically cleaned by flashing to ~ 2500 K every 1/4 -1/2 hour, and (3) the scattering is not diffuse. A very good figure of merit of 1.6×10^{-4} has been achieved for PLEED polarimeters.[3.9] In order to gain the maximum value of the spin analyzing power S, the angular spread of the incident beam at the crystal was set at less than 2° and the energy spread less than 5 eV.

Very low energy electron diffraction (VLEED) from a Fe(100) surface magnetized parallel to the surface has also been used to make a spin polarimeter[3.10] since the reflectivity for the electrons is spin-dependent under certain conditions. The basic cause of this spin dependence is the exchange splitting of the Fe crystal band structure. When the electron energy is close to a critical point, the majority spin density of states is larger than the spin minority density of states. If the incoming electrons are polarized, the number of backscattered electrons depends on the relative orientation of the polarization and the magnetization of the analyzer. The polarization is detected by reversing the magnetization of the analyzer (or the sample) and measuring the change of the count rate. When the energy of the incoming electron beam is from 8 to 14 eV, the backscattered electrons from magnetized Fe(100) films grown epitaxially on Ag(100) single crystal surface yields the largest asymmetry of ~ 5%. The highest figure of merit of 3.8×10^{-3} has been claimed. The configuration of this VLEED polarimeter is compact, efficient and ultra-high-vacuum compatible. Thin film targets are used because they are easy to magnetize and they have negligible stray fields. The disadvantages are that the Fe(100) film surface is easily contaminated and that the Fe(100) crystal surface is not easily grown.

Mott polarimeters based on low-energy (150 eV) diffuse scattering from an amorphous gold surface have been developed that combine high efficiency with small size.[3.11] The detailed description will be given in section 3.3.

The use of the spin dependence[3.12,3.13] of electron-electron scattering (or Møller scattering[3.14]), which is due to the Pauli exclusion principle, has been developed for measuring the longitudinal polarization of high-energy electrons (≥ 300 keV).

Spin-polarized electrons transfer angular momentum in the excitation of Zn atoms from the $4s^2\ {}^1S_0$ ground state to the $4s5s\ {}^3S_1$ excited state. The emitted light polarization from the subsequent decay of this excited state determines the polarization of the incident beam. This effect has also been exploited to make a spin polarimeter.[3.15]

Owing to the spin-orbit interaction, there is a spin dependence in the absorption of a spin polarized electron beam incident on a metal surface.[3.16] This spin dependence is generally enhanced at energies near that where the secondary yield is unity. The polarimeter using this technique is extremely compact and efficient. It has a shortcoming for some applications that it can only measure analog signals and is impossible to count the single electron pulses.

Some of the most widely used spin polarimeters are listed in table 3.1. Based on the operating energies, the spin polarimeters in the table can be divided into two main groups: polarimeters operating at high energies and polarimeters operating at less than 200 eV. The sizes correlate with the operating energies and depend on the particular construction of the different polarimeters. A typical Mott spin polarimeter with the scattering chamber at 100 kV and the surrounding safety region around it will occupy a volume as large as couple of cubic meters. Even for the cylindrical and spherical retarding field types, the high voltage feedthroughs and the safety region will typically occupy approximately 0.1 m^3. The low-energy spin polarimeters are much smaller. The size of a compact spin polarimeter is about 10^{-3} m^3.

All the polarimeters in table 3.1 use solid state targets such as W, Au and Fe except the Hg beam spin polarimeter. The high energy polarimeters use thin Au foils. The foils are very fragile and usually backed with a low Z material. The high energy polarimeters are not sensitive to surface contamination and can operate in a vacuum of 10^{-5} torr, but they can also be operated, if required, in ultrahigh vacuum. The Hg beam spin polarimeter is inherently a low vacuum device and requires significant differential pumping stages if it is to be used in an ultrahigh vacuum experiment. The other three low operating energy spin polarimeters are inherently ultrahigh vacuum devices, although W and Fe single crystal targets used in polarized low-energy electron diffraction spin polarimeter and very low energy electron diffraction respectively are much more sensitive to contamination than the Au target used in the other two polarimeters.

Analyzer type	Operating energy	Size (m^3)	Target	Vacuum required	ΔE	$E A \Omega$ (mm^2 sr eV)	I/Io	S	Figure of merit	Ref.
Mott, traditional	100 - 120 keV	1 - 10	Thin Au foil	10^{-5}	10 keV	10^3	1.5×10^{-3}	0.26	1×10^{-4}	3.4
Mott, cylindrical	60 - 120 keV	10^{-1}	Thin Au foil	10^{-5}	1.3 keV	10^4	10^{-6}	0.33	1×10^{-7}	3.6
Mott, spherical	40 keV	10^{-1}	Thin Au foil	10^{-5}	1.3 keV	10^4	4×10^{-4}	0.20	2×10^{-5}	3.8
Hg beam	15 eV	10^{-3}	Hg atoms	10^{-5}	2 eV	10	2.8×10^{-4}	0.37	4×10^{-5}	3.5
PLEED	105 eV	10^{-3}	W crystal	10^{-10}	2 eV	1.6	2.2×10^{-3}	0.27	1.6×10^{-4}	3.9
Absorbed current	100 eV	10^{-4}	Au film	10^{-9}	10 eV	1			1×10^{-4}	3.16
Low energy diffuse scatt.	150 eV	10^{-3}	Au film	10^{-9}	40 eV	10^2	1×10^{-2}	0.11	1×10^{-4}	3.11
VLEED	8 - 14 eV		Fe(100)	10^{-10}			1.8×10^{-2}	0.50	3.8×10^{-3}	3.10

Table 3.1 Comparison of electron spin polarimeters.

The ΔE in table 3.1 is the allowable energy spread of an electron beam within which the polarization of the beam can be measured by a given spin polarimeter. The range of ΔE is limited by different factors. At high energies, the analyzing power (Sherman function) S does not change significantly with respect to the beam energy. For the traditional Mott polarimeter, the analyzing power S varies slowly with beam energy. The energy spread of the incident beam is limited by the 10 keV energy window of the surface barrier Si detectors. For the retarding field Mott polarimeters, the window can be varied within a big range. In order to let only elastically scattered electrons be detected, the energy spread usually is limited to a small value. A large energy window allows more inelastically scattered electrons to be detected, which improves the efficiency I/I_o, but decreases the analyzing power S. An optimized figure of merit was found for a 1.3 keV polarimeter energy window, which places a similar limitation on the energy spread of the incident beam. At low energies, the analyzing power varies more rapidly with respect to the beam energy. The acceptable energy spread for the low energy spin polarimeters is mainly limited by the scattering conditions which produce high analyzing powers. The typical values of ΔE for the Hg polarimeter[3.5] and for the PLEED[3.9] polarimeter are a few eV. For the low energy diffuse scattering polarimeter, the energy spread is 40 eV.

Another parameter in the table is the electron optical acceptance, or the largest detectable phase space product $EA\Omega$. This parameter varies widely between different spin polarimeters. The high energy of a traditional Mott polarimeter has a very high electron optical acceptance value due to its inherent high electron energy E. A typical beam diameter on a Au foil scattering target of a traditional Mott polarimeter is about 3 mm with an angular spread of about 1°, which yields a value for the acceptance of a traditional Mott polarimeter 10^3 mm^2 sr eV.

The cylindrical and spherical Mott polarimeters focus the beam on to the foil. The phase space product $EA\Omega$ for spherical and cylindrical Mott polarimeters is about 10^4 mm^2 sr eV.

The acceptance angle of the Hg beam spin polarimeter is from 85° to 110°. The analyzing power of the polarimeter remains high over this range. Therefore, the incident beam can have a solid angle of 0.5 sr and still be accepted by the spin polarimeter. This yields the $EA\Omega$ for this low energy detector of the order of 10 mm^2 sr eV.

The electron optical acceptance for the absorbed current polarimeter mainly depends on the angular range of the incident beam, the same as that of the PLEED polarimeter which also has severe constraints on the angular range of the incident beam. For the low energy diffuse scattering spin polarimeter, since a range of scattering angles is detected, there is not a restrictive constraint on the angular spread of the beam to be analyzed. Therefore the electron optical acceptance for this type of polarimeter is quite large (10^2 mm^{2}sr eV).

In general, the most frequently quoted parameter is the figure of merit, S^2I/I_0. The actual values of S and I/I_0 used are important. If S is small and the polarization to be determined is small, the apparatus asymmetries and other systematic uncertainties must be particularly well controlled. The figure of merit is related to other parameters such as the phase space product $EA\Omega$ and energy spread of the beam ΔE. For example, a high figure of merit is achieved in the PLEED spin polarimeter when it is operating at a well defined energy and angle. At different operating conditions, the PLEED polarimeter phase space product can be increased a factor of 6 by doubling A and increasing Ω by a factor of 3. But this would be at the cost of reducing the analyzing power S from 0.27 to 0.20. Clearly it is insufficient to simply compare the figures of merit without considering other factors such as the acceptance phase space and the allowable energy spread. In practice, the electron optical path of a spin polarimeter must be matched to that of the experiment in different cases. Otherwise, there will be only very small part of the incident electron beam detected on the polarimeter target.

3.3 Low Energy Diffuse Scattering Electron Spin Polarimeter

Because electron-spin polarimeters are used in a wide variety of experimental situations, no single set of design objectives can be rigidly applied. However, there are a few main design features which have wide applicability. One of the features is the efficiency of the analyzer system, as measured by the figure of merit S^2I/I_o. This is a very important consideration in spin polarization experiments since the typical range of the FOM is about 10^{-4}. Another factor is the size of the analyzer. As described above, a conventional, high-energy Mott analyzer operating at 100 keV is relatively bulky, typically occupying several cubic meters owing to the required accelerating optics and the safety region around the device. The low energy devices are considerably less bulky.

A detector is also characterized by its electron optical acceptance and the detector design will limit the types of electron sources that can be analyzed without signal loss. In our case, we needed the detector to match small, low-energy sources since the energy range for the 3*d*, 3*p*, 3*s* and 2*p* levels in XPS from 3*d* transition metals is 200 eV to 900 eV (with the photon energy at the same order). This further limits our choices within the low operating energy polarimeters.

Experiments involving spin analysis are extremely complex. An analyzer which is simple to install, to calibrate, and to use is essential. The mechanical and electron optical alignment should also be easily accomplished. The scattering target should remain stable at least for a length of time longer than that of a typical experiment, and the new target should be easily generated if necessary. The stability and ease of installation, alignment and use will depend on the kinds of materials used for the target and the vacuum environment at the detector.

Furthermore. the accuracy of the polarization measurement as distinct from the precision of the polarimeter is also very important. Theoretical calculations of the polarimeters operating at low energies are not reliable enough to permit an initial estimation of the detectors' analyzing power. Therefore, the low energy spin analyzers must be made reproducible and stable, and they must be calibrated by comparison with an analyzer of high accuracy or a source of known polarization. If the spin analyzer is sufficiently stable, the overall accuracy then should be near that of the calibration standard.

Based upon the above criteria, the low-energy diffuse scattering electron-spin polarization analyzer[3.11] was chosen. This spin analyzer is based upon the spin-dependent diffuse scattering of 150 eV electrons by an evaporated polycrystalline Au film due to the spin-obit interaction. The analyzer is sensitive to the transverse components of the spin polarization which are those normal to the scattering plane. A longitudinal polarization (along the incident electron direction) will not be detected. A gold-scattering target was selected for three main reasons. First, the high atomic number of Au leads to a relatively large spin-orbit interaction and hence a greater analyzing power (bigger Sherman function). Secondly, the Au film surface is not as chemically reactive as that of other high-Z materials so that surface contamination is less of a problem. The third reason is that Au is easily evaporated in a clean, well-defined manner.

Electrons scattered by the evaporated polycrystalline Au film yield a diffuse and structureless spatial distribution. Figure 3.4[3.17] shows a measurement of the angular dependence of the asymmetry and intensity for the scattering of 145 eV electrons from a Au film. The measurement was made by directing polarized electrons from a GaAs source at various Au film targets and measuring the scattered electron distributions with a Faraday cup. Angular profiles were also measured by the same authors with incident electron energies from 100 to 300 eV. The angular profiles showed smooth, atomic-like variations in intensity and asymmetry with respect to various beam energies. On the other hand, the scattering from a single crystal is extremely sensitive to angle and energy as the electrons scattered from the crystal lattice have a well defined diffraction pattern. While the total integrated intensity of scattered electrons from a polycrystalline sample is about the same as from single crystal samples, the energies and angular dependencies are different. The insensitivity of the scattering from the polycrystalline Au film to angle and energy yields only a small signal being scattered into any particular direction. This weak angular dependence is compensated for by the use of a detector having anodes with a large solid angle of acceptance that integrate over a large range of intensities and asymmetries.

3.4 Layout and Assembly of the Electron-spin Polarization Analyzer

The schematic layout of the electron-spin polarization analyzer is shown in figure 3.5. It is composed by three main assemblies: an HA 50 hemispherical analyzer from VSW Scientific Instruments Ltd, which is used to analyze the energy distribution of the photoelectrons, a plane mirror analyzer (PMA) which is used to bend the trajectory of the electrons another 90 degrees (the reason for doing so will be explained shortly), and a low-energy diffuse scattering electron-spin polarimeter.

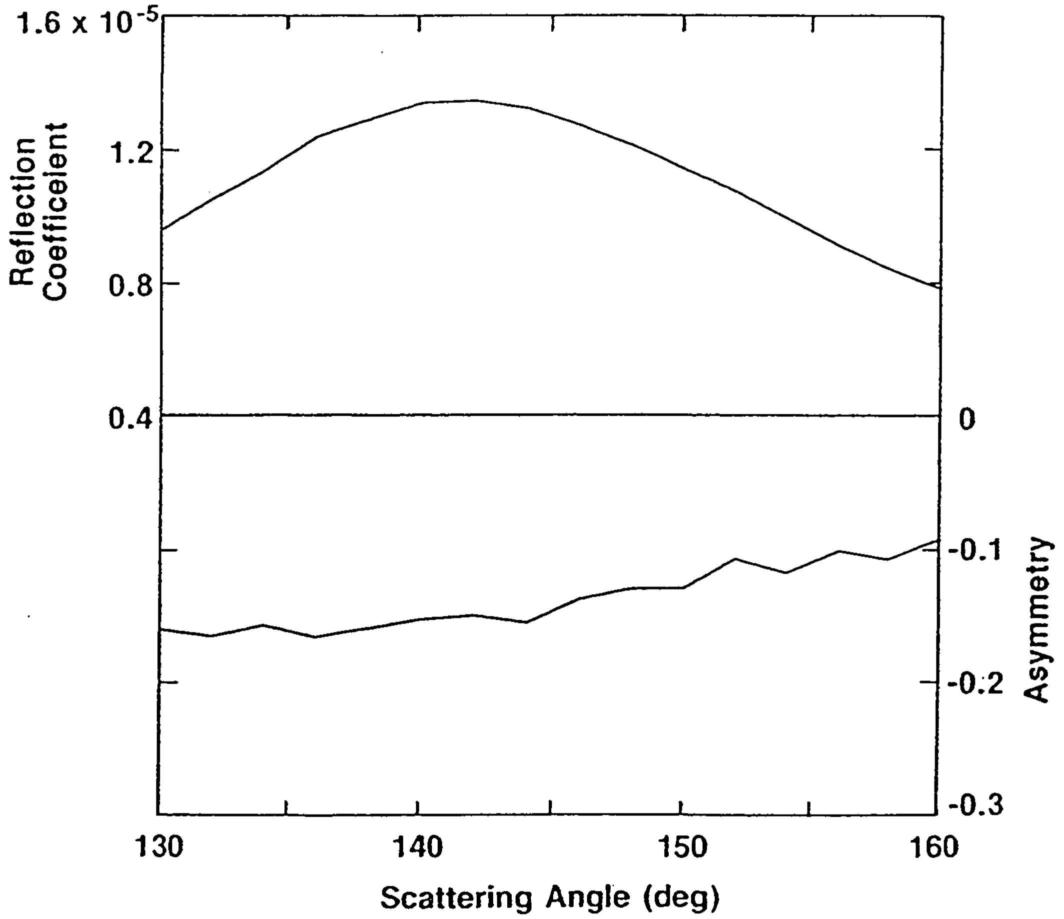

Figure 3.4 Angular dependence of the intensity and of the spin-dependent asymmetry for completely polarized electrons scattered elastically from a polycrystalline gold film at 145 eV.[3.17]

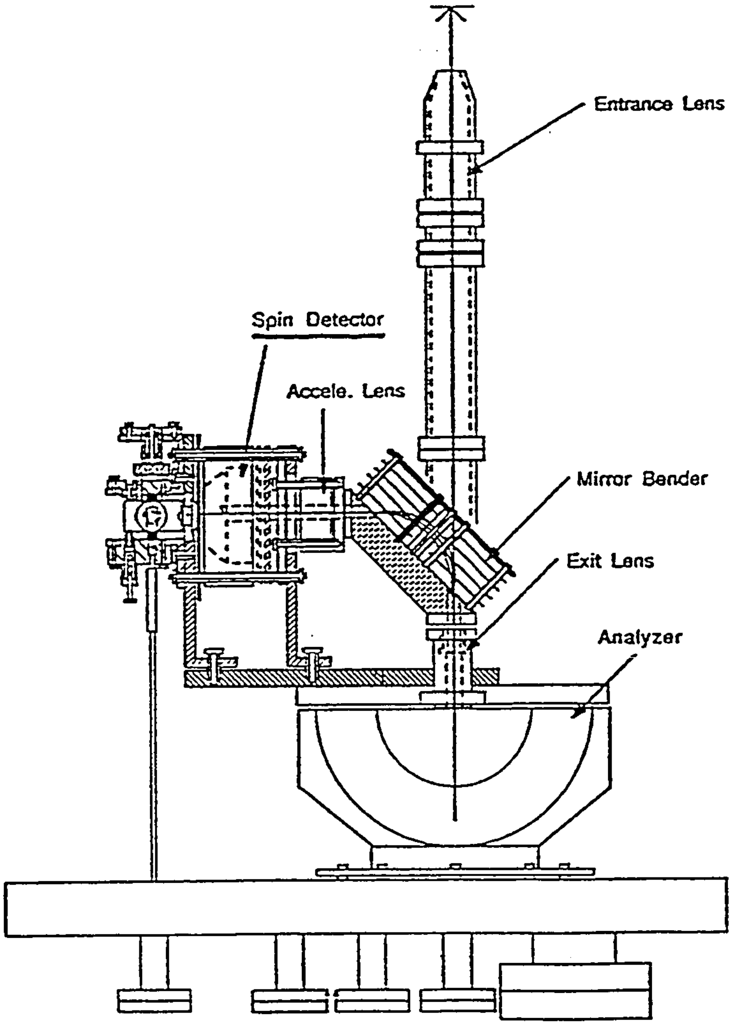

Figure 3.5 Layout of the electron spin polarization analyzer.

A schematic diagram of the hemispherical electron energy analyzer is shown in figure 3.6. Photoelectrons excited from the sample by the incoming radiation drift in a field free region to the first element of the entrance lenses. For a selected kinetic energy, electrons are retarded and focused at the entrance aperture of the hemispherical selector by a cylindrical four-element electrostatic lens. With the correct potentials applied to the inner and outer hemispheres, the selected electrons follow a semicircular path around the analyzer and are focused on the exit aperture of the hemispherical selector in both directions. The mean radius of the analyzer is 50 mm, with $r_{\text{in}} = 36$ mm and $r_{\text{out}} = 74$ mm. Except for the entrance lenses, all of the electron optical components of the analyzer are standard. The entrance lenses were specially designed to collect large solid angles to increase the photoelectron current. Figure 3.7 shows the raytracing results for a photoelectron energy of 100 eV and lens voltages of proper values. This electron raytracing calculation was carried out with the EGUN raytracing program available from the Stanford Linear Accelerator Center, Stanford University.[3.18] The acceptance angle of the entrance lenses is ±3 degrees. The distance between the sample and the entrance aperture over which the zoom lens focuses is 30 mm. Space charge effects have been neglected in the calculation since Kuyatt and Simpson[3.19] have shown that they do not seriously affect the electron paths if the transmitted current is less than the critical value given by

$$I_{\text{crit.}} = 1.17\times10^{-2}E_0^{3/2}\alpha_{\text{max}}^2 \quad (\mu\text{A}) \qquad (3.11)$$

where E_0 is the electron pass energy and α_{max} (4 degrees) is the maximum electron in-plane diverging angle from the central ray of the bundle in the analyzer. The values of $I_{\text{crit.}}$ are given in table 3.2 for E_0 = 10.0 to 100.0 eV. The maximum current from an Fe sample with incident radiation from the undulator based X1B beamline is about 50 nA at 250 eV photon energy (50/50 μm entrance

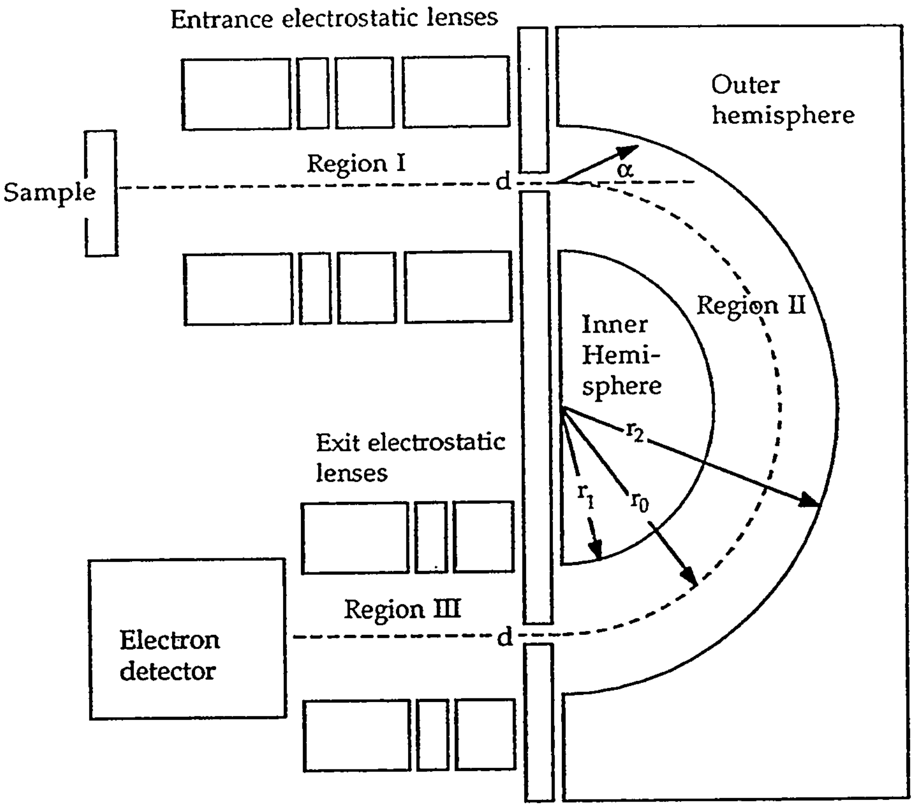

Figure 3.6 Layout of an HA50 hemispherical electron energy analyzer.

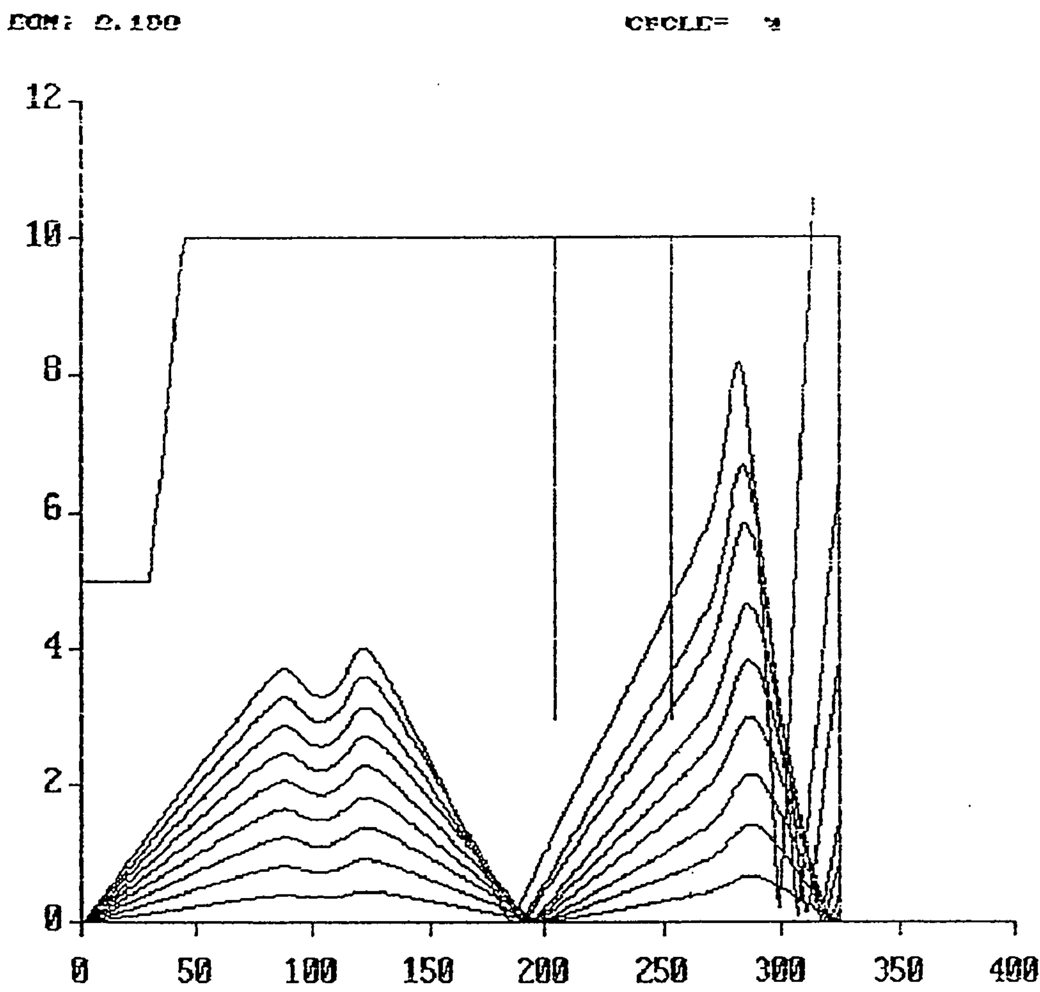

Figure 3.7 Raytracing results of the analyzer entrance lenses with electron kinetic energy of 40 eV and pass energy of 25 eV.

I_{crit}(μA)	E_o(eV)
0.20	1.0
0.57	2.0
2.24	5.0
6.32	10.0
17.90	20.0
70.73	50.0
200.04	100.0

Table 3.2 Critical transmitted current vs. electron pass energy.

and exit slit settings). The photon source resolution matches the analyzer resolution with a pass energy of 10 eV. Therefore, the space charge effects can be neglected.

To reduce any patch fields, a coating of a colloidal graphite solution in iso-propyl alcohol (Acheson Colloid Dag 380) was applied to the inner surfaces of the lens elements and hemispheres.

All electron spin polarimeters based on the electron spin-orbit interaction only measure the polarization of transversely polarized electron beams. To measure the polarization of the low-energy, longitudinally polarized electron beams, one simple way is to electrically deflect the electrons another 90 degree. The spin of the electrons will keep their direction during the deflection. Therefore, the longitudinal polarized electrons become transversely polarized and can then be measured by a spin-polarimeter.

There are many apparatus which can be used to deflect electrons through 90 degrees. The criteria to be matched are: (1) deflection of electrons by 90 degrees; (2) high efficiency of transmission; (3) small size; (4) ease of design and manufacture; (5) ease of assembly and alignment; (6) ultrahigh vacuum compatibility. After careful consideration, the concept of an electrostatic miniature plane mirror analyzer[3.20] (PMA) was chosen. Figure 3.8 shows the schematic layout of such an analyzer. The input lens focuses the electron beam from the exit aperture of the hemispherical analyzer to the entrance aperture of the PMA. The lens is composed of only two elements. In order to satisfy the focal condition, the electron energy has to be accelerated by a constant (in this case, by a factor of 4). The base and the top plate form the body of the PMA. Four guiding plates are used to correct the fringing fields. They are evenly spaced between the top plate and the base, fed by a potential divider having five equal sections. The exit lens accelerates the electrons to 150 eV of kinetic energy and

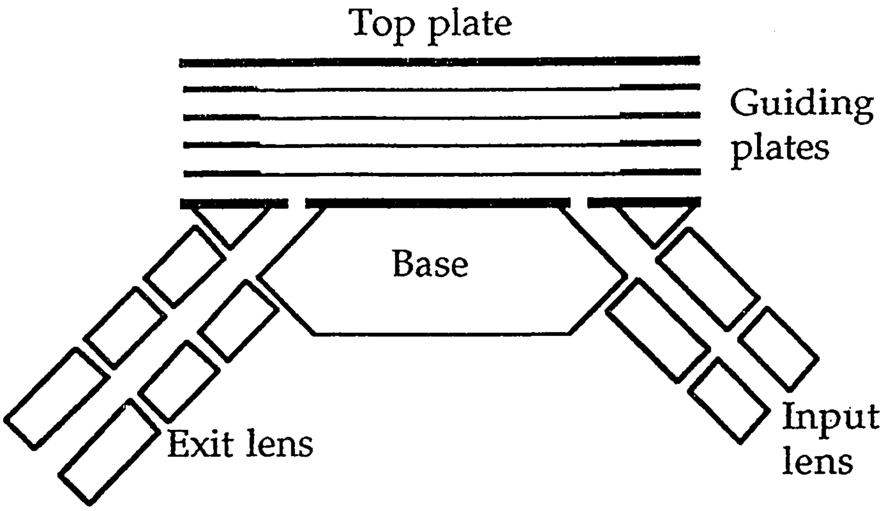

Figure 3.8 Layout of the plane mirror analyzer (PMA).

focuses the electron beam from the PMA, through the drift tube of the spin analyzer, to impinge onto the Au target. Electrical insulation between the lens component parts is maintained by sapphire balls. The plates of the PMA main body are held together by six ceramic posts and with ceramic spacers between the plates. Non-magnetic stainless steel screws are used to construct the PMA and lenses.

The advantages of the PMA are that it is simple, easy to design, manufacture, assemble, align, and it is very compact. A disadvantage is that it only focuses the beam in one direction and the beam diverges in the other direction. However, the divergence should be small since the electron path in the PMA is very short (the distance between the 2 mm × 2 mm entrance and exit apertures is only 20 mm). For an electron beam from the hemispherical analyzer with ±6 degrees divergence and with optimized voltage supplies on all the elements, the transmittance would be 88%.

Figure 3.9 is the layout of the low-energy diffuse scattering electron-spin polarimeter. Incident electrons are accelerated and focused through the drift tube, onto an evaporated polycrystalline gold target by the three element tube lens described above. The drift tube here serves several purposes: (1) to allow a drift region for the incident electron trajectories; (2) to define the inner collection angle $\theta_{in} = 30°$, which blocks the zeroth order backscattered electrons with scattering angle > 180° – 30° = 150° (zeroth order backscattered electrons do not yield any asymmetry due to the electron spin-orbit interaction); (3) to prevent electrons deflected back by the negatively biased focusing electrode E_1 from being collected at a quadrant anode on the opposite side of the detector and (4) to aid in defining the field needed for effective energy filtering.

After passing through the drift tube, the electrons strike the target. There are two targets on the assembly. These can be moved alternatively in and out of

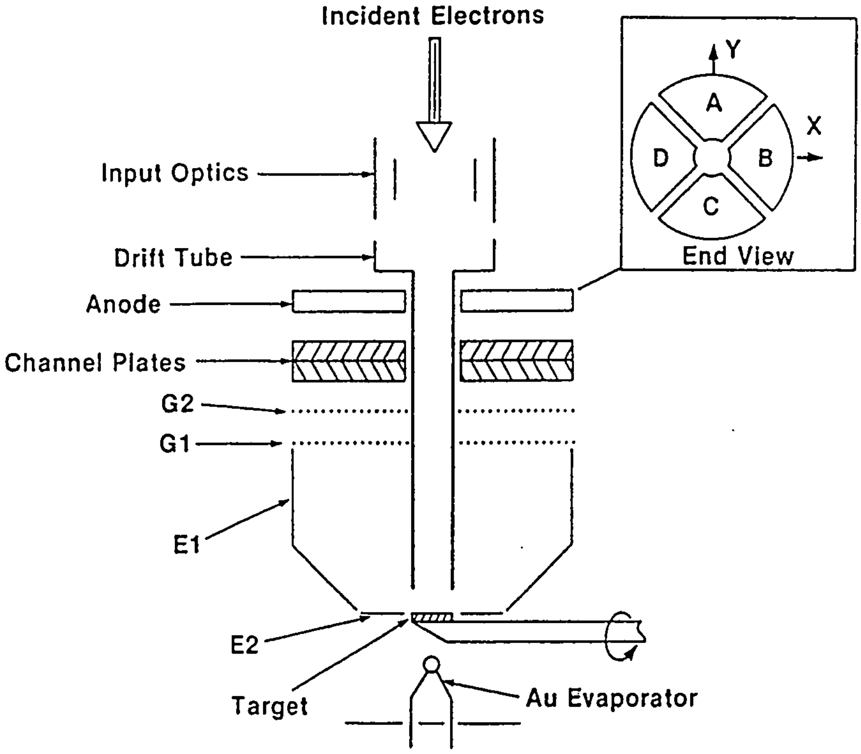

Figure 3.9 Layout of the low energy diffuse scattering electron spin polarimeter.

registration positions with a manipulator. Both targets have Al substrates. One of them is covered with graphite, which is used to check the system asymmetries since graphite does not exhibit a scattering asymmetry. The other target can have Au film evaporated on to it's surface after moving it out of the electron beam. The evaporation requires a vacuum in the pressure range better than 1×10^{-9} torr. Because the electron energy at the target is only 150 eV, the mean-free-path is only 5 Å.[3.21] Therefore, the electron scattering characteristics of the Au film are not particularly sensitive to the substrate material or to its preparation. The Au evaporator consists of a mini-basket constructed from 0.0010" diam. tungsten wire .

The drift tube and the target are at the same potential so that the scattering occurs in a nearly field-free region. A positive bias applied to the electrode E_2 coplanar with the target, combined with a negatively biased focusing electrode E_1 forms a simple optical lens, which serves two purposes: (1) to deflect electrons scattered through wider angles back toward the detector and hence increase the effective electron optical size of the detector; and (2) to shape the field so that the electron trajectories are more normal to grid G_1 thereby improving energy filtering in the grids.

Secondary electrons that are generated at the target do not carry the polarization information of the incident electrons and hence will degrade the signal. In order to prevent the secondary electrons from reaching the electron multiplier, a positive bias with respect to the target is applied to grid G_1 and a negative bias to G_2. The grids are constructed from stainless steel thin sheets prepared by photochemical machining (4×4 wires/mm^2, 0.025 mm-diam wire). Figure 3.10 shows a raytracing of the electron trajectories in the spin detector with optimized potentials applied to all components.

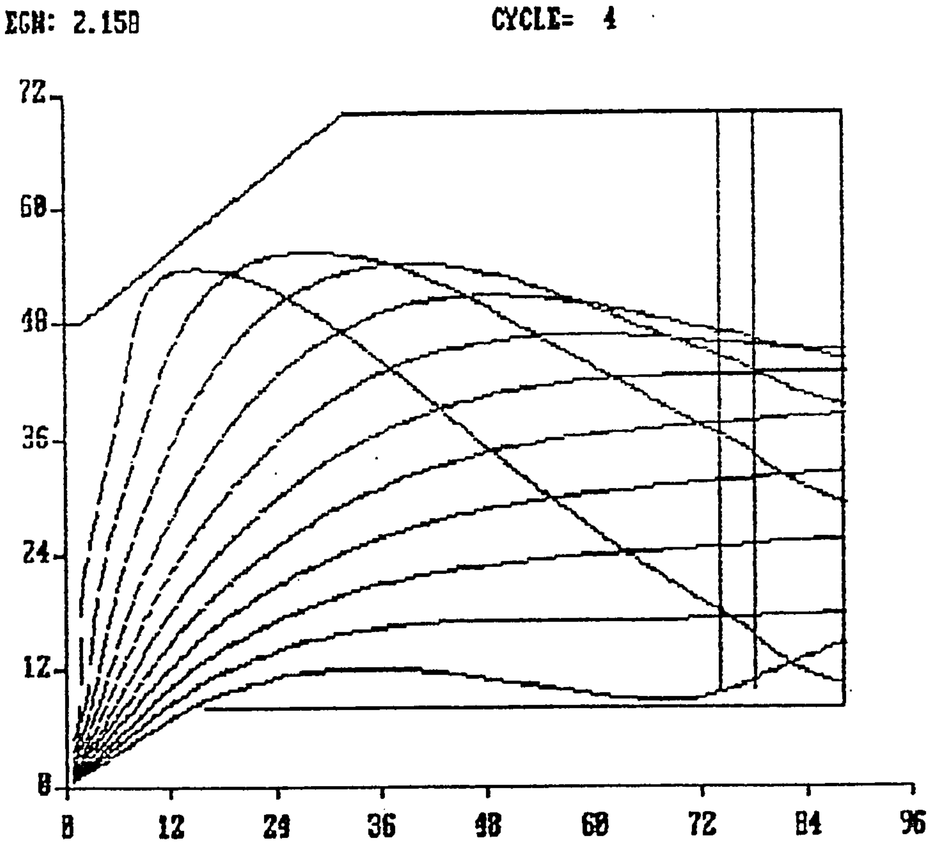

Figure 3.10 Raytracing results of the spin polarimeter.

Electrons that pass the retarding grid are accelerated into the electron multiplier assembly which collects and amplifies the signal. This assembly consists of a chevron group of three microchannel plates and a four quadrant anode. The channel plates are provided by the manufacturer with a 6-mm-diam hole in the center for the drift tube. Three microchannel plates are used to saturate the signals i.e. drive the signals into saturation and thereby improve stability. The pulse height distribution from the device yields a flat dip, close to zero intensity, between the background noise and the real signal. The noise can then be easily discriminated out of the signal by electronics, giving a more stable count rate for fixed high voltages applied to the channel plates.

The anode pattern is shown as the inset in figure 3.9. The four quadrants permit simultaneous measurement of the incident electron beam's two transverse spin polarization components, P_x and P_y. Again, since the electron beam has been deflected through 90 degrees, one pair of anodes arranged normal to the plane of the electron trajectory in the PMA yields the longitudinal spin polarization components of the electron beam P_x given by

$$P_x = \frac{1}{S}\frac{N_A - N_C}{N_A + N_C}. \qquad (3.12)$$

Here N_A and N_C are the count rates measured by anode quadrants A and C respectively, and S is the analyzing power. Similarly P_y is given by

$$P_y = \frac{1}{S}\frac{N_B - N_D}{N_B + N_D}. \qquad (3.13)$$

The assembly of the spin detector, consisting of the evaporator shield, E_1, E_2, G_1, G_2, the channel plates, and the anode, is held together by six ceramic posts and spacers equally spaced around the spin polarimeter. The size of the spin detector is 5" long by 3" wide. The spin detector and the PMA are mounted directly onto the hemispherical analyzer. All three components, the analyzer, the

PMA and the spin polarimeter, are linked together by the electron optical lenses and are held by an insulated support. Every single optical element has been simulated by ray-tracing and all the electron optical lens linkages were carefully designed based on the ray tracing results. They are mechanically well aligned and fixed to a 13" flange. This flange has three single pin SHV feedthroughs for the voltage supply to the chevron channelplates, a 20 pin feedthrough for the electron-optical elements, a separate four pin SHV feedthrough for the quadrant anodes, a viewport in line with the entrance lens of the hemispherical analyzer for aligning the analyzer with respect to the sample, and a rotary feedthrough for moving the targets in and out of the electron beam. The Au evaporator feedthrough (with a viewport on it) is also mounted on the flange. The whole apparatus is shielded with 1 mm thick μ-metal to screen external magnetic fields.

The input lens of the hemispherical analyzer and the hemispherical analyzer itself are controlled by the HAC300 control unit from VSW. All other electron-optical elements including all the lenses, components of the PMA and spin polarimeter, are controlled by an adjustable voltage divider that is driven by a 0-300 V floatable voltage power supply referenced to the Helmholz plate of the hemispherical analyzer.

3.5 Tests of the Electron-spin Polarization Analyzer

The tests of the electron-spin polarization analyzer were performed in three stages, including potential divider adjustments, x-ray photoemission tests, and the effective Sherman function calibration by means of spin-polarized XPS.

The first step was to optimize the potentials of the different elements of the analyzer for maximum count rate. The source of electrons for this step was the secondary electrons generated by shooting an electron beam of 2 keV kinetic energy on a Ag(100) single crystal surface from a standard electron gun. A series of measurements of the count rate were performed for a wide variety of bias potentials on the different elements.

For diffuse scattering electrons, 150 eV kinetic energy gave the highest analyzing power, i.e. the largest effective Sherman function S on the gold film target.[3.11] Obviously, the target potential must be set at 150 eV relative to the first energy of the hemispherical analyzer, as does the drift tube. Figure 3.11 shows the count rate as a function of the potential of the base of the PMA. The pass energy of the hemispherical analyzer was set at 25 eV in this case. The maximum count rate is at a PMA potential of 59 V. Figure 3.12 shows the count rate as a function of the potential applied to the center element of the three-element acceleration lens which connects the spin polarimeter and the PMA. The maximum count rate is at 57 V. Both results were in agreement with the raytracing calculations.

The potentials of retarding grids G_1 and G_2 were also adjusted. The count rate did not change significantly when the discrimination voltage ΔV (the potential difference between G_1 and G_2) was varied in the region from 40 V to 135 V with G_1 at 200 V. The anode count rate showed little change either when the potential of G_2 was varied up to 230 V with ΔV fixed at 135 V. With the potentials of the grids set at 225 V and 90 V for G_1 and G_2 respectively, $\Delta V = 135$ eV, which completely retards all the secondary electrons produced by the incident electrons impacting on the target. The secondary electrons do not yield any spin information for the incident electrons so their contribution to the signal should be minimized. The potential of G_1 was set at the highest possible value because the higher the potential on G_1 the more perpendicular are the electron trajectories through it. Table 3.3 lists the potential configurations for different elements of the spin polarimeter with respect to the first energy.

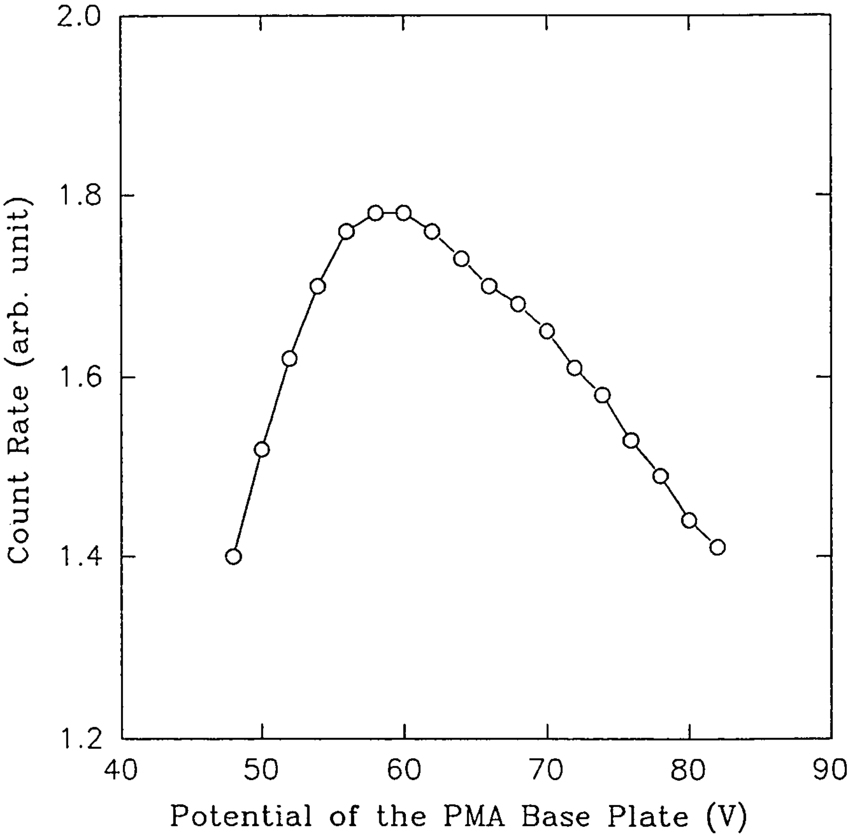

Figure 3.11 Count rate vs. the potential of the base plate of PMA.

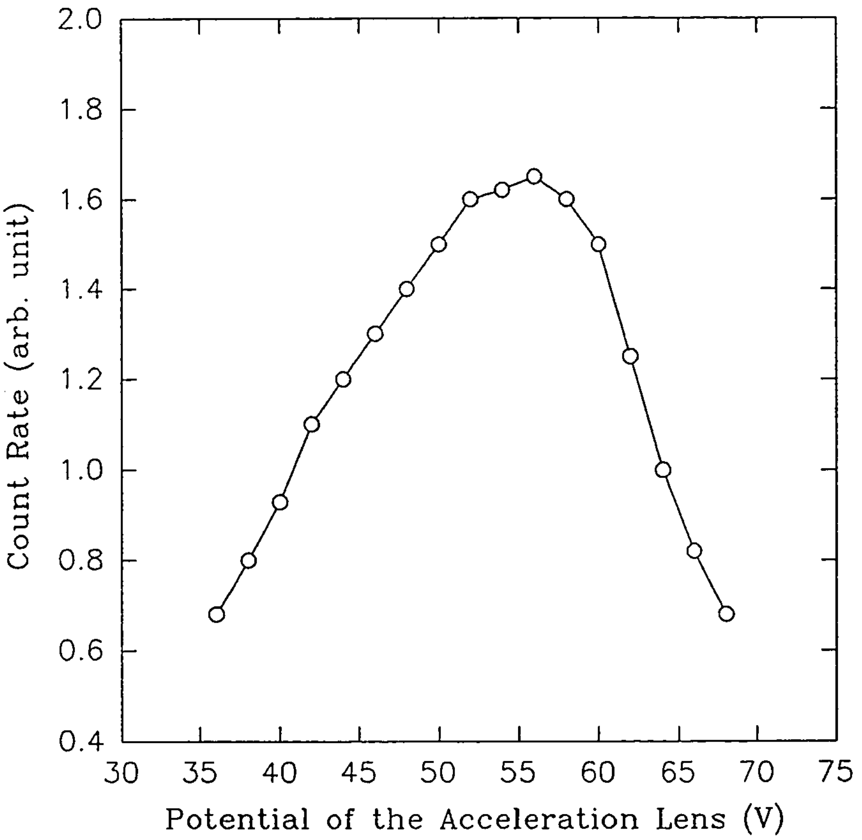

Figure 3.12 Count rate vs. the potential of the acceleration lens.

Elements	Potentials (V) (respect to first energy)
Base of PMA	59.0
Top plate of PMA	−12.3
Acceleration lens	56.0
Drift tube	150.0
Au target	150.0
Cu deflect plate	0.0
Grid 1	225.0
Grid 2	90.0
Target frame	150.0

Table 3.3 Potential configurations for the lenses.

Since the analyzer is dedicated to spin polarized XPS studies on synchrotron radiation beamlines, the second step of the tests were performed on the undulator based X1B beamline (refer to chapter 2 for the details of the beamline), the source of the soft x-ray photons. Different samples were tried including a clean Ag(100) crystal and a clean Cu(100) crystal. The base pressure of the chamber was below 3×10^{-10} torr. The purposes of the tests were: (1) to find the energy resolution of the analyzer; (2) to calibrate the energy of the analyzer; (3) to have a sense of the count rate with the photon source from X1B. Different pass energies of the analyzer were tried with different slit settings for the beamline. The latter determine the resolution of the photon source.

The resolution of the analyzer is given by[3.22]

$$\Delta E = \left(0.43\frac{d}{r_0} + \frac{\alpha_{\max}^2}{4} \right) E_0, \tag{3.14}$$

where d is the entrance and exit aperture widths of the analyzer, $r_0 = (r_1 + r_2)/2$, is the central radius of the analyzer, $\alpha_{\max}$ is the maximum divergence pencil angle in radians and E_0 is the pass energy of the analyzer. In the present case, d = 2 mm, r_0 = 50 mm and $\alpha_{\max}$ = 4 degrees. The energy resolution is then ΔE = 0.0184 E_0, which equals 0.46 eV for a pass energy of 25 eV. This matches the resolution of the beamline with slit settings of 100/100 μm, providing 85% of the total flux at first order into a photon spot size of ~ 0.7 × 0.7 mm. The latter is about the size of the analyzer focal point.

Figure 3.13 shows the Ag(100) 3d photoemission spectrum taken with the analyzer with a pass energy of 25 eV. The photon energy was 490 eV. With beamline slit settings at 50/50 μm, it yielded a count rate of 2.4×10^3 /s. After the standard Gaussian-Lorentzian deconvolution fitting analysis, the spectrum of Ag(100) 3*d*'s gave the resolution (FWHM) of ~ 0.5 eV. The results agree with

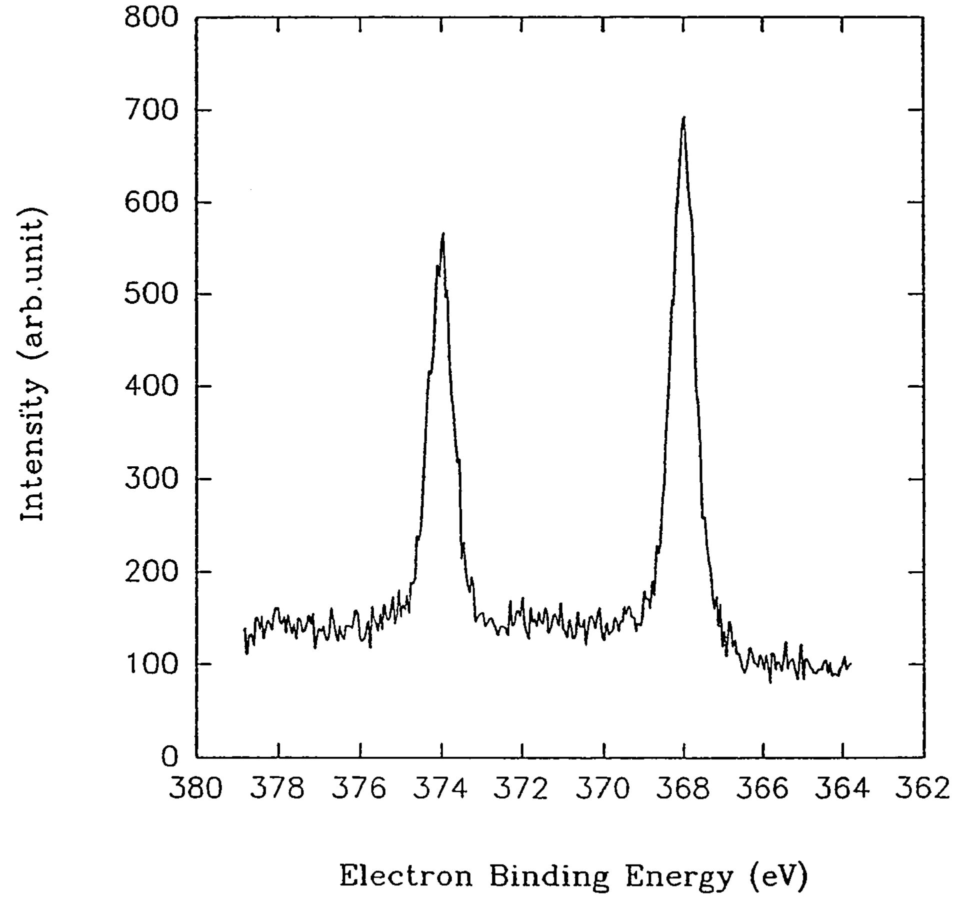

Figure 3.13 Ag(100) 3*d* XPS spectrum. hν = 490 eV.

the above theoretical estimation. The energy of the analyzer has been calibrated by comparing the 3p and 3d photoemission peaks from Cu(100) spectrum (see figure 3.14) with tabulated values.[3.23]

Spin-resolved 3p core level x-ray photoemission spectra on 3*d* transition metals Fe and Co have been well defined experimentally.[3.24-27] With the help of existing experimental data, the analyzing power S of the analyzer has been calibrated on the X1B beamline. The polarization of the signal is defined by

$$P=\frac{1}{S_{\mathrm{eff}}}\frac{N_{\uparrow}-N_{\downarrow}}{N_{\uparrow}+N_{\downarrow}}, \qquad (3.15)$$

where $N_{\uparrow}$ and $N_{\downarrow}$ are the number of counts measured by the relevant anode quadrants, S_{eff} is the effective Sherman function, i.e. the analyzer resolving power, which is a constant for a given analyzer. By varying the effective Sherman function and comparing to existing spectra, a $S_{\mathrm{eff}} = 0.05$ was obtained. This is comparable to the other polarimeters.

It is often found that the direction of spontaneous magnetization in a ferromagnetic thin film is oriented within the plane because of the shape anisotropy. In extremely thin films however the easy direction often turns to be along the surface normal of the film. This behavior can be explained by assuming an interface anisotropy that exists only at the interface atomic layer. It has been proposed for a long time that the source of spin anisotropy in a ferromagnet results from the spin-orbit interaction coupling the spin to the lattice.[3.28] Relevant experimental efforts focused on this issue include surface magneto-optic Kerr effect,[3.29] Mössbauer spectroscopy,[3.30] ferromagnetic resonance,[3.31] Brillouin scattering[3.32] and spin-polarized photoemission.[3.33] Most experimental studies have focused on the magnetization/polarization in terms of the thickness and/or temperature of the thin films even for those spin-polarized

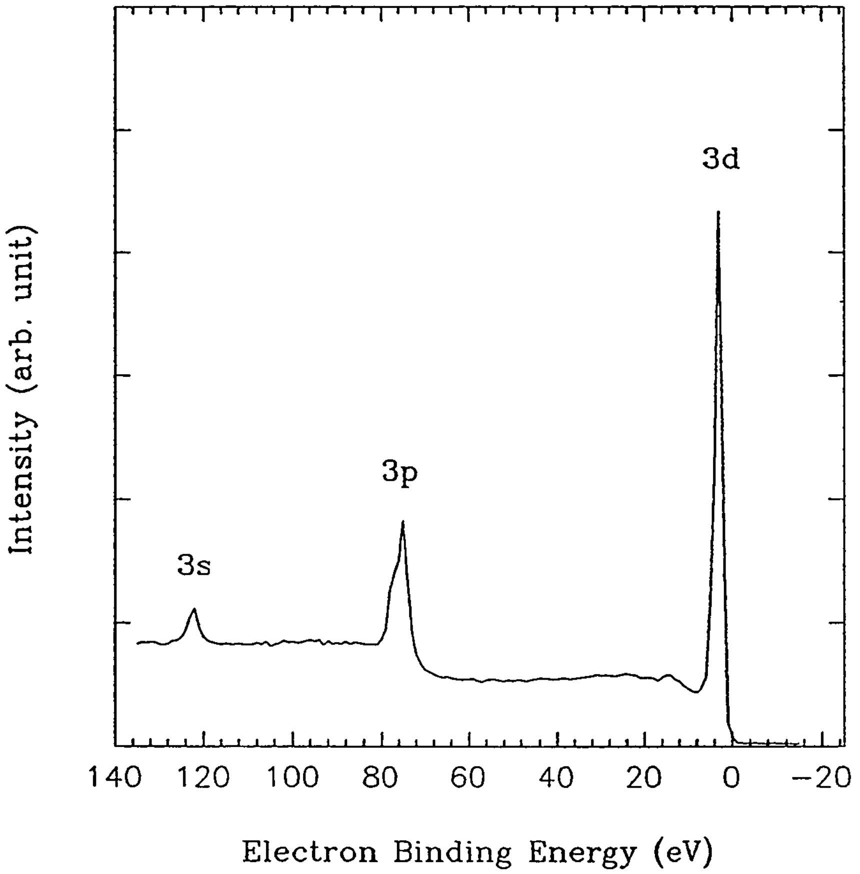

Figure 3.14 Photoemission spectrum of Cu. hv = 250 eV.

photoemission experiments. We know that spin-polarized photoemission spectroscopy can reveal localized information on the ferromagnetic electronic structure at surfaces and thin films. Because spin analyzers used in spin-polarized photoemission experiments often can not perform measurements of the longitudinal spin portion, they can not give direct information on the electron spin structure at normal emission. The spin analyzer we have constructed can perform both measurements of the longitudinal and transverse electron spin. It is the ideal analyzer for studying the spin anisotropy of ferromagnetic thin films and overlayers through spin-polarized XPS.

Figure 3.15 shows the perpendicular and parallel components of the magnetization versus the thickness of Fe film grown on Ag(100) at room temperature. Figure 3.15 (a) are the results obtained by means of the surface magneto-optic Kerr effect.[3.34] Figure 3.15 (b) are the results obtained by means of spin polarized secondary electron spectroscopy taken with our electron spin analyzer. The primary electron energy is 2 keV and the secondary electron energy is 45 eV. Since Fe *d*-band has more majority electrons than minority electrons, this yields the secondary electron population imbalance between the two spins. The fall in polarization for small thicknesses side is due to following two reasons: (1) The decrease of the Fe overlayer thickness results in an increase in the substrate signal which leads to an overall smaller secondary electron polarization. (2) Because the experiments are carried out at the same temperature, the decrease of the Fe overlayer thickness results in a decrease of the Curie temperature T_c [3.35,3.36] which results in a decline of the polarization signal at the small thickness side. The results are consistent with the results shown in figure 3.15 (a).[3.34] This proves that the analyzer has the ability to study the spin anisotropy systems.

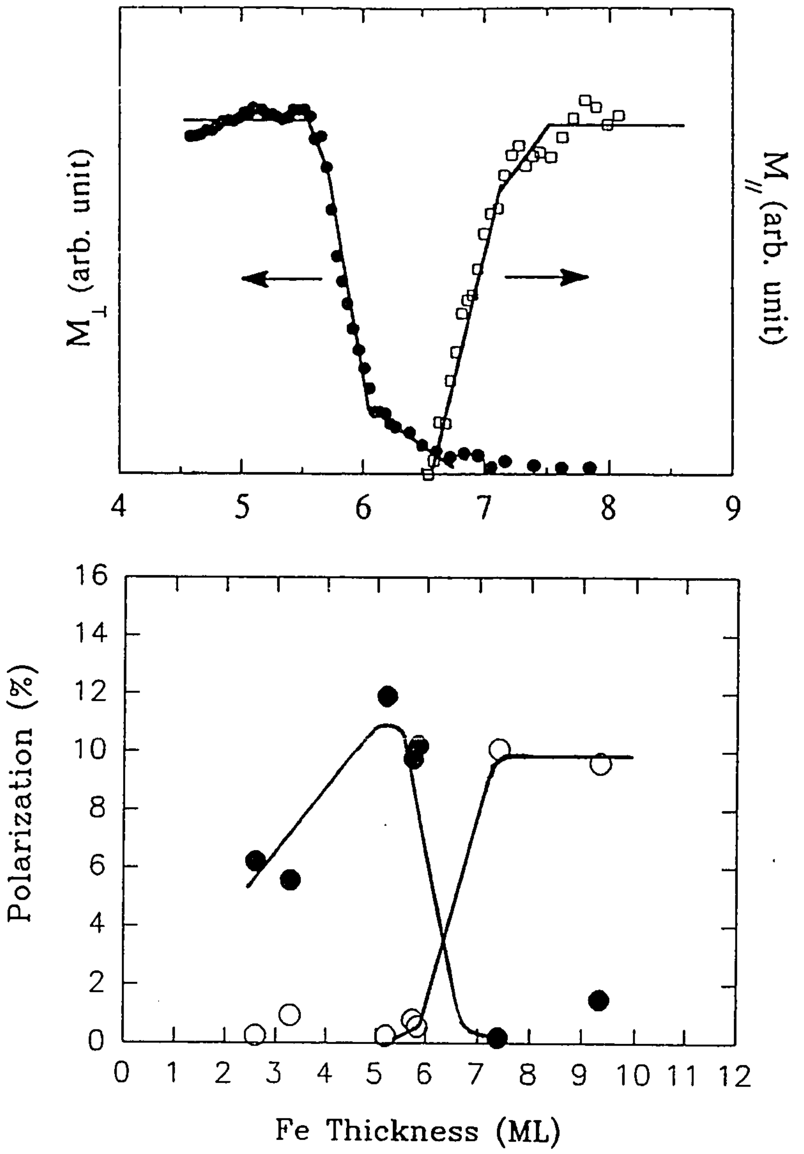

Figure 3.15 Perpendicular $M_\perp$ and parallel $M_{//}$ components of the magnetization vs. the thickness of Fe film grown on Ag(100) at room temperature. (a) the results obtained by means of the surface magneto-optic Kerr effect.[3.34] (b) the results obtained by means of the spin polarized secondary electron spectroscopy taken by electron spin analyzer. Solid dots are for $M_\perp$ and open dots are for $M_{//}$.

Chapter 4 Spin Polarized XPS Experimental Considerations

4.1 Introduction

The spin polarized x-ray photoemission spectrometer is dedicated to studies of electronic and magnetic properties of surfaces, interfaces and thin films. The basic photoemission system including the spin polarization photoelectron analyzer and the sample are enclosed in an ultrahigh vacuum chamber. This chamber also houses the necessary equipment to prepare and characterize the sample surface. The spin polarized XPS experiment needs not only a super intense, well collimated, monocromatized, tunable x-ray source, and a state of art spin-polarized electron analyzer as described in chapter 3, but also a series of advanced equipment allowing sample preparation, thin film growth, and surface and thin film characterization and magnetization.

Figure 4.1 is a schematic diagram of the complete spin polarized x-ray photoemission spectrometer system. The X1B beamline[4.1,4.2] has its own computer system which basically controls the focusing mirrors, the grating and the exit slit position. The computer also monitors the photon flux and scans the photon energy. The experimental chamber is connected directly to the end of the beamline via bellows. Since the photon energy is within the soft x-ray region the whole beamline is under ultrahigh vacuum.

Through the exit slit and the bellows, the monochromatic photon beam is focused onto a well prepared and magnetized sample to stimulate photoelectrons from the sample surface. These photoelectrons are then collected by the spin-polarization analyzer.

The experimental system will in general possess some instrumental asymmetry. This can be due to different amplification on different area of the

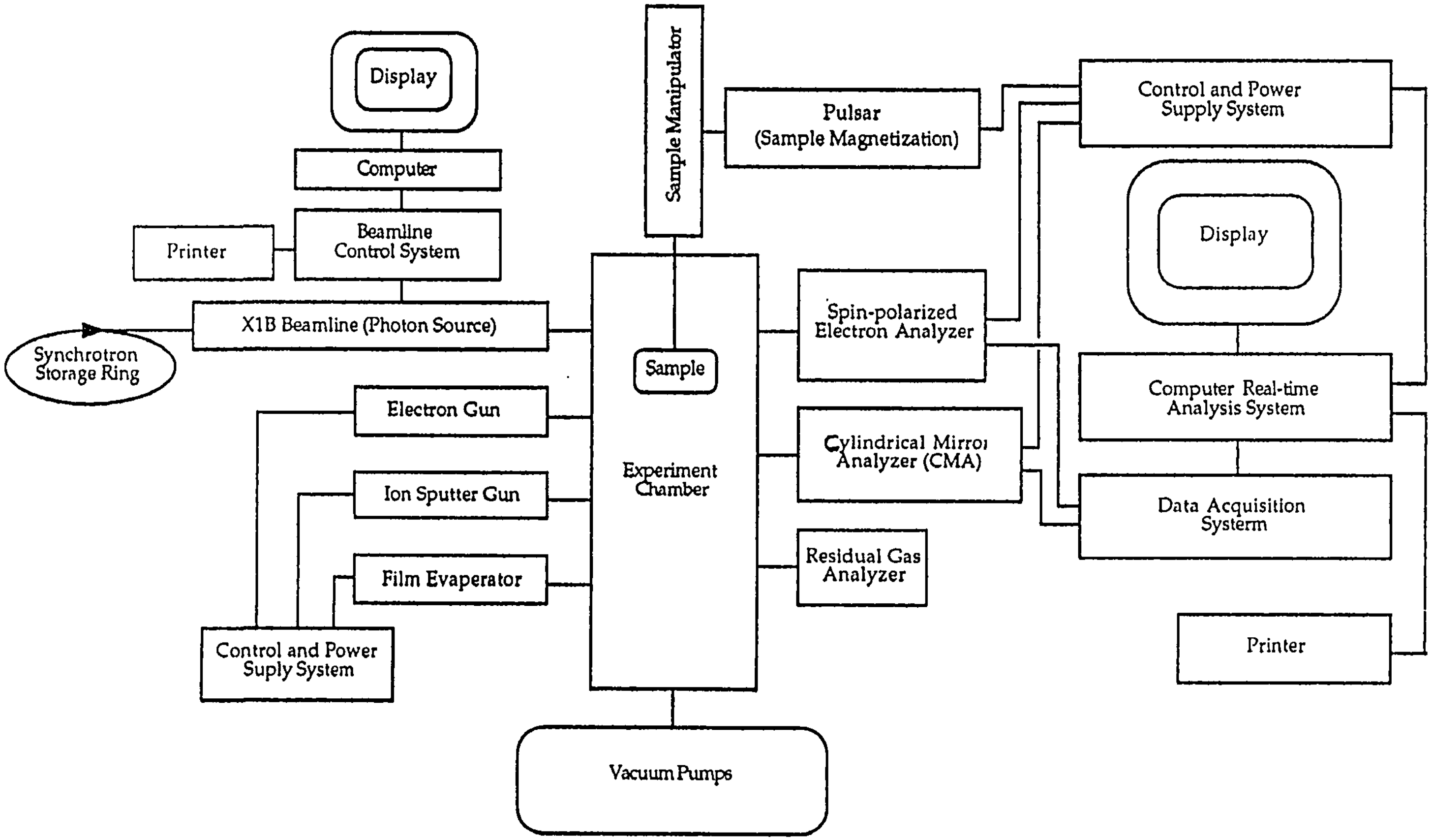

Figure 4.1 Diagram layout of the spin polarized x-ray photoemission spectrometer system.

channel plates, different capacitance of the anodes, imbalance of the different amplifiers on different channels, non-axial alignment of the electron beam upon the target, and inhomogeneity of the target surface. In order to eliminate the system asymmetry, the following method was used during the experiments. Each spin polarization measurement is derived from two scans, one with the sample magnetized 'up', producing two sets of data N_L^u and N_R^u, and one with the sample magnetized 'down', producing two sets of data N_L^d and N_R^d. Here N_L and N_R are the number of electrons scattered from the Au target in the spin analyzer and detected at the left and right anodes respectively. The instrumental asymmetry can then be canceled by combing the four sets of data and the true spin polarization is given by[4.3]

$$P = S_{\mathrm{eff}} \frac{\sqrt{N_L^u N_R^d} - \sqrt{N_L^d N_R^u}}{\sqrt{N_L^u N_R^d} + \sqrt{N_L^d N_R^u}}, \tag{4.1}$$

where S_{eff} is the effective Sherman function. If the incident beam does not move between 'up' and 'down' scans, the intensities combined in this way removes the instrumental asymmetry derived from the misalignment of the beam incident on the target together with any asymmetry caused by the imbalance of the electronics. With this method, the instrumental asymmetry will not affect the measured polarization even though the two scans may have different count rates. Assuming that there is no asymmetry that changes for the two magnetization directions, the instrumental asymmetry is given by

$$A_{\mathrm{INS}} = \frac{\sqrt{N_L^u N_L^d}}{\sqrt{N_R^u N_R^d}}. \tag{4.2}$$

The individual spin-up and spin-down spectra are given by

$$N^{\uparrow} = \langle N \rangle (1 + P), \qquad N^{\downarrow} = \langle N \rangle (1 - P), \tag{4.3}$$

where

$$\langle N\rangle = \frac{N_L^u + N_L^d + N_R^d + N_R^u}{4}. \tag{4.4}$$

The statistical errors in the polarization and spin intensities are calculate as (see appendix 5)

$$\Delta P = \frac{1}{\sqrt{4\langle N\rangle S_{\mathrm{eff}}^2}} \tag{4.5}$$

and

$$\Delta N^{\uparrow} = \frac{N^{\uparrow}\Delta P}{(1+P)}, \qquad \Delta N^{\downarrow} = \frac{N^{\downarrow}\Delta P}{(1-P)}, \tag{4.6}$$

where for the errors of N_i^j, the statistical errors $\sqrt{N_i^j}$ have been substituted.

4.2 Features of the Experimental System

The experimental system can be divided into four components: (1) spin-polarized XPS; (2) sample preparation and characterization; (3) ultra-high vacuum (UHV) pumping and monitoring; and (4) system control and data acquisition. The XPS level of the chamber includes a 2.75" conflat flange port for accommodating the incoming photon beam, the electron spin polarization analyzer, and an electron gun for the alignment and test of the analyzer. The photon beam port has a gate valve attached on it, which can be closed to keep the system under vacuum while the system is pulled on and off the beamline. The PHI model 04-015 5 kV auxiliary electron gun serves as a test source for the analyzer and also for secondary electron spectroscopy studies while the system is off the beamline. The analyzer is sealed in a separate 8" long by 10" diam vacuum chamber (refer to chapter 3 for details of the analyzer). This analyzer chamber is connected to the main chamber through a 4.5" conflat flange which allows the entrance lens of the analyzer to stick through and point at the sample.

Figure 4.2 shows the layout of the sample manipulator. It was originally designed to have *X*, *Y* and *Z* (vertical) linear drive movements, with the *XY* motion being table driven and the Z motion thimble driven. It also allows for $\phi = 270^\circ$ polar rotation (along Z direction) and $\theta = \pm 90^\circ$ azimuthal rotation (normal to Z direction) of the sample. In order to be used for the present experiments, the manipulator was further modified to include features allowing: (1) control of the sample temperature in the range of –100°C ~ 800°C; and (2) magnetization of the sample both in and normal to the plane of the surface.

The samples were mounted on a Varian button heater on the sample holder. The sample can be heated by a button heater to ~ 1000°C in 20 minutes. In order to cool the sample to lower temperatures a liquid nitrogen dewar was designed which was connected to the sample holder by two copper braids. In this way the sample can be cooled down to a temperature of –120°C from room temperature within 20 minutes. The temperature was monitored by a thermal couple attached to the surface edge of the sample.

Two sets of copper coils were mounted around the sample to serve as magnetizing coils. These coils were insulated with fiber glass sleeves and were further shielded by Al foil in order to avoid charging effects.

The sample preparation and characterization stage includes a sputter ion gun, resistive heating evaporators, leak valves for a gas inlet system, and a cylindrical mirror analyzer (CMA). The PHI model 04-162 2 kV sputter ion gun was used to clean the samples. The 0.015" diam W baskets containing the evaporants were used to grow thin films of Fe, Co, Mn and Cr by means of resistive heating evaporation. Except for Fe, these evaporant materials have relatively low-melting point compared to W and a good constant growth rate from a W basket with the resistive heating method. Fe forms an alloy with W and the evaporation rate drops very fast during the growth. To solve this

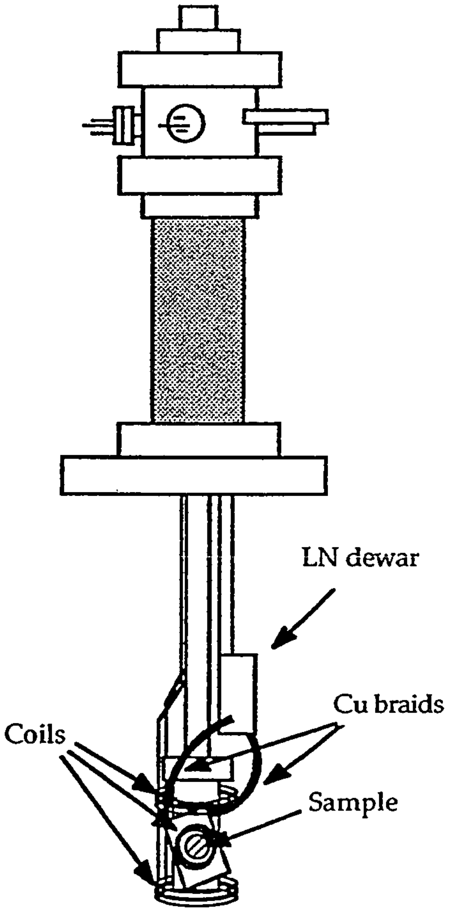

Figure 4.2 Layout of the sample manipulator.

problem and make it more stable, 0.010" Fe wire was wound around the W basket instead of putting bulk Fe in the basket.

Leak valves along with the gas inlet system were used to introduce gas into the chamber for sputtering the samples or doing surface chemical adsorption studies.

The PHI model 15-255G double pass cylindrical mirror analyzer (CMA) is the main apparatus for the Auger electron spectroscopy (AES) studies which characterize the sample surface cleanness and the thin film thicknesses. The general principles of the CMA can be found in any relevant books.[4.4,4.5]

The Auger effect is a process where a core hole of an atom at energy E_A is filled by an electron from a shallower level E_B together with the emission of another electron from level E_C with kinetic energy

$$E_k = E_A - E_B - E_C. \qquad (4.7)$$

The emitted electron is called the Auger electron. Figure 4.3 shows a schematic diagram of this process where E_A is E_{C1} and E_B E_C are E_{C2}. Low energy Auger electrons have a short mean free path, and hence the AES can be a powerful surface sensitive probe for surface composition, thin film coverage and growth morphology analysis.[4.6]

Normally the AES spectra are taken in a differential mode ($dI(E)/dE$ versus E) instead of the direct mode ($I(E)$ versus E) by superimposing a modulation on the AES signals and using a lock-in amplifier. The reason for doing this is that the intense and steeply sloping background of the secondary electrons in the energy distribution makes direct mode AES measurement extremely difficult. Quantitatively the ratio of the composition in a sample is proportional to the ratio of the AES cross section $\sigma(E)$ and the area of the peaks of the AES signal $I(E)$ rather than the amplitudes of $I(E)$. It is difficult to evaluate the areas of $I(E)$ peaks but in the differential mode, the ratio of the peak-to-peak

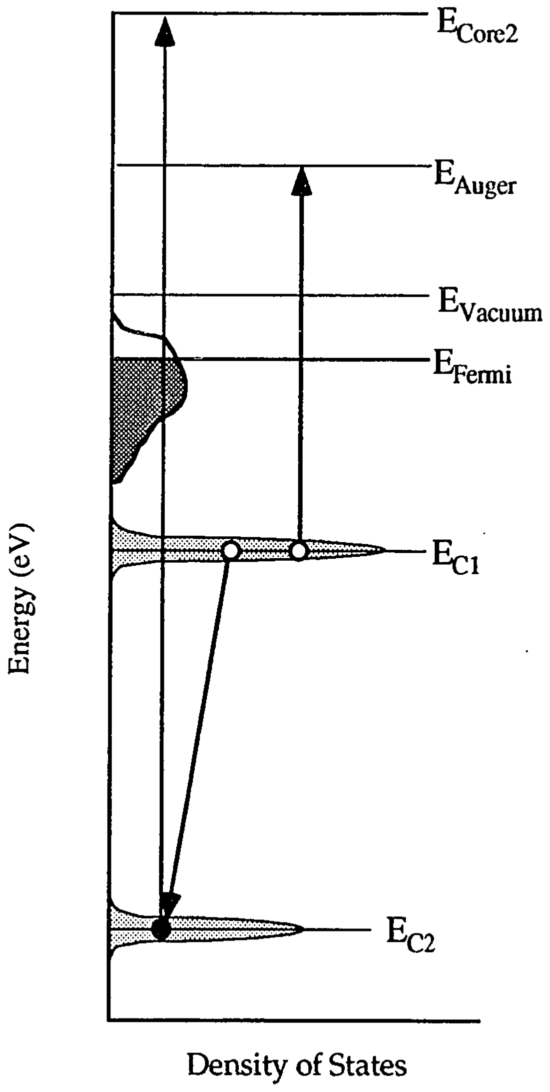

Figure 4.3 Schematic diagram of the Auger process.

height is proportional to the ratio of the area in the direct mode. It is much easier to measure these peak-to-peak heights rather than evaluate the area of a peak, especially when the peak has backgrounds and satellites as a normal AES signal does.

Figure 4.4 shows the AES spectra of a Ag sample before (upper) and after (lower) the cleaning treatment (several cycles of Ar bombardment and annealing). The primary electron energy was 2 keV and the peak-to-peak height of the modulation was 2 V. The positive excursion of the C peak is much weaker than the negative excursion which reflects the broad loss tail of the direct Auger peak. For this reason, it is common to label the peak energies in AES as the energy of the largest negative excursion in the differentiated spectrum.

Spin polarized XPS involves the detection of electrons emitted from the first several layers of atoms at the surface of the sample. This imposes the requirement that all experiments be conducted in an ultra-high vacuum (UHV) environment. The reason for this can be seen by considering the average number, $\bar{n}$, of gas molecules striking a unit area of a surface per second. It follows directly from kinetic theory that

$$\bar{n} \approx 2.89 \times 10^{22} \frac{P}{\sqrt{MT}} \qquad \mathrm{cm^{-2}s^{-1}} \qquad (4.8)$$

where P is the gas pressure measured in mbar. T is the absolute temperature and M the molecular weight. Taking M to have a mean value of 28 for air, at room temperature T = 300° K, the rate of coverage will be ~ 10^6 $S{\cdot}P$ monolayer per second, where S is the sticking coefficient. Hence for $S = 1$ and a pressure of 'air' of 10^{-9} torr (i.e. mm of Hg), approximately one hour passes before a monolayer of residual gas molecules in deposited on the sample. However, S is strongly dependent on the nature of the adsorbate, the substrate, and the substrate temperature. For the single crystal surfaces of silver and copper studied at room

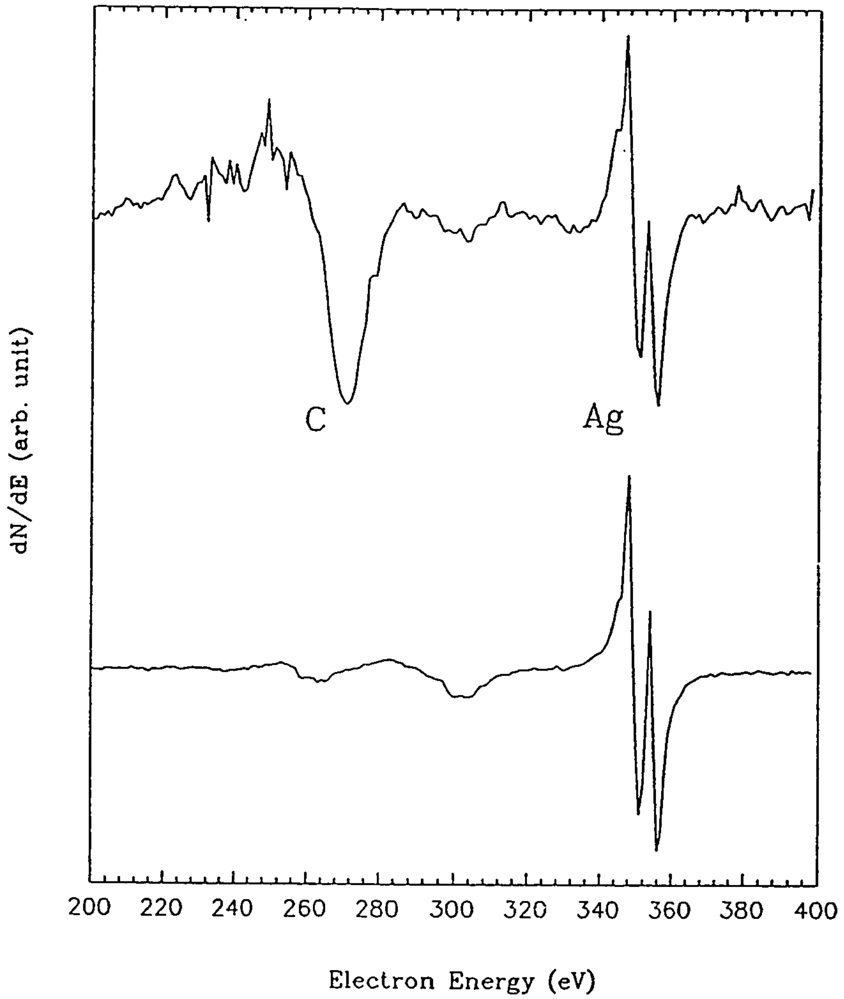

Figure 4.4 AES spectra of Ag(100) before (up) and after (down) treatment.

temperature, no significant surface contamination could be detected by AES and XPS after several hours with $P = 2\times10^{-10}$ torr and $T = 300$ K.

Apart from keeping the sample surface clean there are two other reasons why a vacuum is required for these experiments. Firstly, the beamline is under UHV and opens directly to the synchrotron radiation storage ring. This requires the experimental chamber which is directly linked to the beamline to maintain a pressure below 10^{-10} torr. Otherwise a differential pumping stage is necessary. Secondly, the microchannel plates in the spin detector cannot be operated at pressures greater than 10^{-6} torr. If the pressure exceeds this limit, ions may be produced by electron collisions with ambient gas molecules or with gas molecules desorbed from the channel walls. These ions can drift back to the channel input and create ion after-pulses.

The UHV pumping stage consists of an ion pump, a titanium sublimation pump (TSP), a turbomolecular pump and a roughing pump. The chamber was manufactured from high quality austentitic stainless steel (AISI 316LN) and all permanent joints were argon arc welded and flanges sealed by using copper conflat gaskets. The chamber was equipped with a residual gas analyzer (RGA) system and two Bayard-Alpert type ion gauges. The composition of the residual atmosphere was monitored by Vacuum Generators (VG) quadrupole mass spectrometer (type QX200).

Baking of the system begun after the system pressure was brought down to 10^{-7} torr by the Varian model TURBO-V200A turbomolecular pump along with the roughing pump. The ion pump (Varian 400 L/S diode model 912-7022) was turned on and the valve between the system and the turbo pump closed afterwards. The baking was turned off only after the system pressure reached ~ 1×10^{-7} torr with temperature at ~ 150°, all filaments had been out gassed, and the water vapor pressure was less then the carbon monoxide pressure as shown by the RGA. The base pressure after baking was ~ 3×10^{-10} torr. At base pressures of 3×10^{-10} torr the residual gas was composed mainly of hydrogen, essentially introduced by the μ-metal magnetic field shielding inside the chamber, water vapor and carbon monoxide. Cooling down the trap of the Varian titanium sublimation pump (TSP) with liquid nitrogen and flash the TSP would bring the pressure further down to 1.5×10^{-10} torr.

Stray magnetic fields existing around the system will deflect the electrons away from their proper trajectories. To prevent this problem, the experimental region and the analyzer region were screened by 1 mm μ-metal. Apart from the main source, the Earth's magnetic field, there was a large stray field from the ion pump. This was screened by 4 mm soft iron sheets. These procedures brought the field in the analyzer region down to less than 1 mG and in the experimental region to 40 mG. This could be brought down further by using Helmholtz coils to generate an equal and opposite field.

4.3 Control and Data Acquisition System

Figure 4.5 shows the schematic layout of the control and data acquisition system. Each analyzer and gun has its own control unit commercially available from the venders. The control system for the electron spin polarization analyzer can be divided into two sections: a low voltage and a high voltage section. For the low voltage section the potentials for the entrance lens and the hemispheres were controlled by the HAC-300 control unit available for the analyzer. The potentials for the exit lens, the plane mirror analyzer (PMA), acceleration lens and electron spin detector were controlled by a passive high-stability voltage divider driven by a HP model 64488 DC 0-600V/0-3A power supply. This latter supply was floating on top of the Helmholz plate potential introduced from the

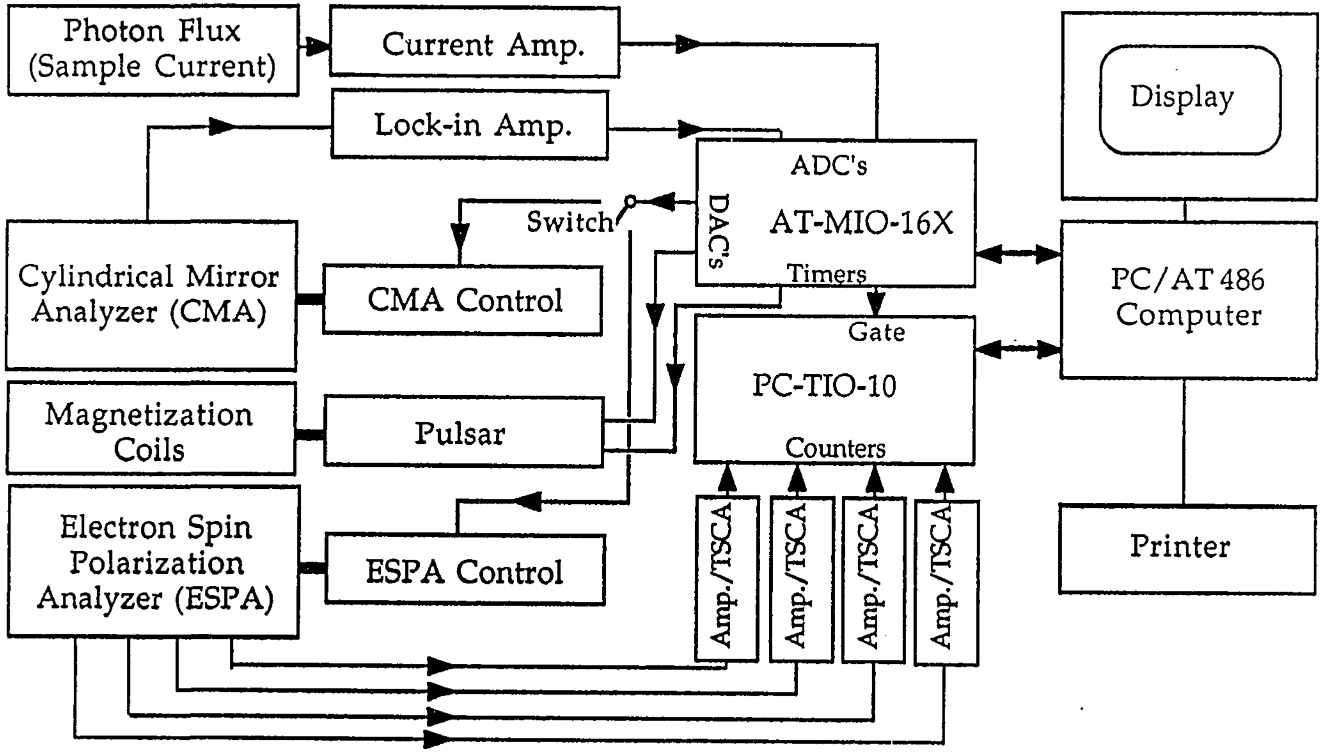

Figure 4.5 Schematic layout of the system control diagram.

HAC-300 control unit. The voltage divider is constructed with high precision metal resistors and high precision potential meters with a temperature stability better than 0.02% per °C. The energy of the analyzer can be controlled by a 0-10 V analog input. The high voltage section is composed of a passive voltage divider driven by a 0-5 kV/0-5 mA high voltage power supply that controls the voltage on the channel plates and the quadrant anodes. The signals from the latter anodes were decoupled through high pass capacitor-resistor bridges.

The PHI model 15-255G double pass cylindrical mirror analyzer (CMA) was controlled by the PHI model 20-810 analyzer control unit. Again the first energy can be operated by a 0-10 V analog input. The channeltron on the back of the CMA was powered by a high voltage power supply with a voltage divider box. A capacitor-resistor bridge was again used to decouple the signals from the channeltron.

The sample magnetization coils were controlled by a pulser made by the technical support group of the NSLS. This pulser contains a large capacitor, a trigger switch and a polarity control relay along with a 0-500 V/0-20 mA high voltage power supply. With the capacitor charged up to 100 V, the pulser can generate a peak current $I = 800$ A pulse with $T = 1.5$ ms width through a 20 turn coil of 2.5" diam. This yields ~ 1.5 kG magnetic field which is strong enough to magnetize the thin film sample. The pulser has two operation modes, a local mode and a remote mode. When the local control mode is used, the pulse polarity is controlled by a polarity switch and the device is triggered with a manual switch. When the remote control mode is used, the pulse polarity is controlled by a 0 V or 5 V input for positive or negative polarity respectively. The pulse is triggered by the rising edge of a 0–5V pulse through the trigger input.

The control and data acquisition system for the instrument were based on a Gateway model 200 PC/AT 486 compatible computer with two plug-in boards: a National Instruments model AT-MIO-16X 16-bit high-resolution, multifunction analog, digital, and timing I/O board and a model PC-TIO-10 16-bit timing and digital I/O board. The AT-MIO-16X board has 2 independent 16-bit digital-to-analog converter (DAC) output channels, 3 independent 16-bit counter/timer input/output channels and 16 single-ended 16-bit analog-to-digital converter (ADC) input channels. The PC-TIO-10 board has 10 16-bit, 7 MHz counter/timer input/output channels. One of the DAC output channel from the AT-MIO-16X board was programmed to control the electron-spin polarization analyzer and the CMA. The other DAC was programmed to control the polarity of the pulser. The trigger of the pulser was controlled by one of the counter/timer channel from the AT-MIO-16X board. The photon flux and the AES analog signals from the current amplifier and the lock-in amplifier were read directly by the ADC input channels of the AT-MIO-16X board. The four channel pulse signals decoupled from the quadrant anodes of the electron polarization analyzer were amplified and scaled into the transistor-transistor logic (TTL) signals by four independent Canberra model 2015A amplifier/TSCA's, and counted by four of the counters on the PC-TIO-10 board. The four counters were gated by one of the counter/timers from the AT-MIO-16X. The maximum current the DAC channels can supply is 5 mA, while the impedance of the analyzer analog input for the CMA control is 5 kΩ. That yields a maximum current loading on the DAC up to 2 mA at 10 V, i.e. the same order as it can take. In order to protect the board, 1:1 operational amplifies were used to increase the input impedance to 1 MΩ.

The system control and data acquisition program is written entirely in LabVIEW icon based language provided by National Instruments. The functions the program contains include: (1) system tune-up or tune mode; (2) two modes of data acquisition (AES and XPS); and (3) capabilities to read, sum, smooth and plot previously stored data.

The tune mode is for tuning and balancing the four different signal channels from the analyzer. The system is equivalent to four independent rate meters plus an analog voltage meter recording the incident photon flux or AES signal. Shown in figure 4.6, the analyzer voltage may be adjusted through use of a mouse.

The data acquisition mode has two parallel subroutines. Subroutine one is for updating DAC and timer channels to control the analyzer and the pulser, and read the counter and ADC channels. Subroutine two is for data real time analysis and display. Subroutine one reads the data and sets the flag and starts another cycle. As soon as subroutine two reads the flag, it starts to do the real time analysis and plotting. During the scanning, file parameters may be written in without interrupting data acquisition. One may also tell the computer to pause, stop after the current scan and abort the acquisition or add more scans during the acquisition.

In the XPS mode, the pulser changes its polarity and is trigged before each scan. Each spectrum has 10 channels of data which includes electron energy, photon flux, N^u_L, N^u_R, $N^u_{L'}$, $N^u_{R'}$, N^d_L, N^d_R, $N^d_{L'}$ and $N^d_{R'}$ (refer to the introduction of this chapeter for the definitions of N) The program displays one large spectrum window and two smaller spectrum windows. Each window can show any of six spectra alternatively (see figure 4.7). They are photon flux, integrated XPS, transverse spin resolved XPS, longitudinal spin resolved XPS, transverse spin polarization and longitudinal spin polarization.

The read, sum, smooth and plot data mode simply reads, sums, smoothes, or displays earlier stored data, scales and moves spectra, and investigates the

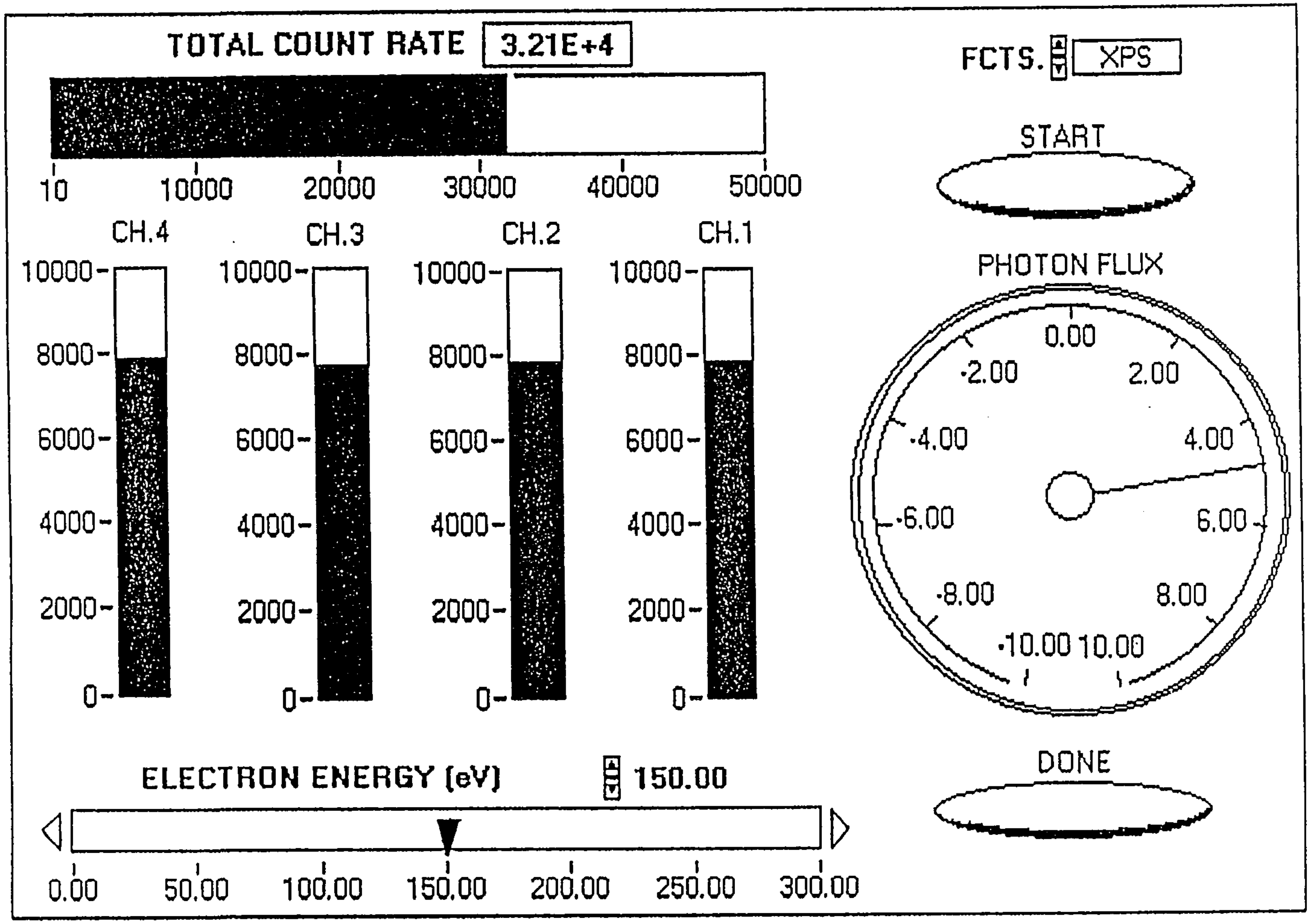
TOTAL COUNT RATE 3.21E+4

FCTS. XPS

ELECTRON ENERGY (eV) 150.00

Figure 4.6 Tune mode of the program.

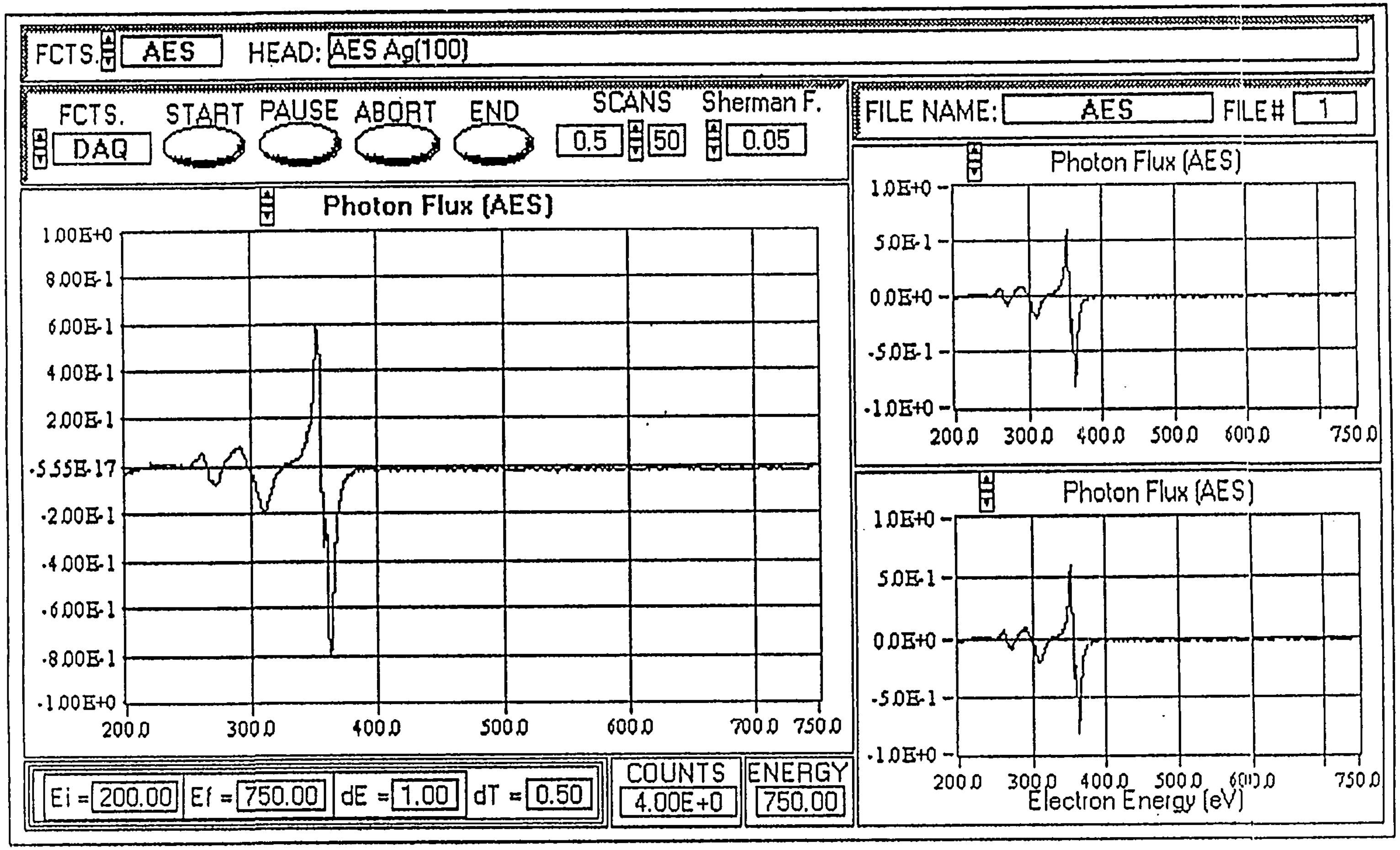

FCTS. AES
HEAD: AES Ag(100)

FCTS. DAQ

SCANS 0.5 50

Sherman F. 0.05

FILE NAME: AES
FILE# 1

Ei = 200.00
Ef = 750.00
dE = 1.00
dT = 0.50

COUNTS 4.00E+0

ENERGY 750.00

Figure 4.5 Schematic layout of the system control diagram.

contents of individual channels. The spectra windows are organized the same as that of the real time displays.

Chapter 5. XPS Study of Fe and Co 3*p* Spin Polarized Spectra

5.1 Introduction

Some of the 3*d* transition metals such as Fe and Co have been intensly studied due to their ferromagnetic properties. As an example, for pure α-Fe with the bcc structure, the local magnetic moment of each Fe atom in the bulk is 2.2 Bohr magnetons (μ_B) and the ferromagnetic spin alignment is maintained up to a Curie temperature T_C = 1043 K. For the bulk hcp structure Co, the local magnetic moment on each atom site is 1.6 μ_B. On the other hand, the magnetic properties of the surfaces and interfaces are less well known. Indeed it is still very difficult to obtain reliable information on individual atoms at surface or interface sites.

On the theoretical side, using the so called full potential linearized augmented plane wave method, Freeman's group[5.1-5.4] has systematically carried out a theoretical calculation of the electronic and magnetic properties of thin films with a thickness of several layers. Their results show that the magnetic moment of the top layer is considerably larger than the bulk value. In the case of Fe(100) for example, it is calculated to be 2.98 Bohr magnetons (μ_B). On the experimental side, during the last decade, a number of experiments to measure the ferromagnetic properties of thin films have been developed. In order to obtain information from surface of thin film systems, the method chosen for the experiment must be (1) surface sensitive and (2) element specific. The conventional methods such as neutron scattering or Mössbauer spectroscopy are not so effective for the study of surfaces.

Spin polarized core level x-ray photoelectron spectroscopy (XPS) is a probe which meets both the surface sensitive and element specific requirements. It also has the potential for providing information on local magnetic moments in ferromagnetic systems. The reasons for choosing to study Fe and Co 3*p* core levels are: (1) The magnetism of the ferromagnetic transition metals Fe and Co is the archetype for the study of the whole subject of metallic magnetism. It would seem necessary, if not sufficient, to understand the properties of these pure metals before attempting to understand those of more complex ferromagnetic transition metal systems. (2) The photoemission cross section of the 3*p* core level electrons is much larger than that of 3*s* core level electrons.[5.5] This is crucial for the study of thin film systems such as a monolyer of Cr or Mn on Fe, where for instance, the 3*s* spin polarized XPS signal is so small that it is practically impossible to obtain useful information with current apparatus. (3) Since 3*p* core level spin polarized XPS spectra for Fe and Co have been experimentally measured, study of these elements provides a good test and calibration of a newly established system.

Based on the core hole atomic multiplet structure and the *d* electron orbital quenching due to delocalization or translational symmetry, a simple model for the description of *p* core level spin polarized photoelectron spectra of 3*d* transition metals is described. Using this simple model, experimental results from Fe and Co grown on Ag(100) and Cu(100) respectively are examined. Through study and analysis of the data, we can obtain a better understanding on the spin polarized XPS process which hopefully will yield new information on the local magnetic structure.

5.2 Experimental Procedures

The spin polarized XPS experiments reported in this thesis were carried out on thin films epitaxially grown on non-magnetic single crystal substrates. Thin film samples were chosen because they are easy to magnetize and have a negligible stray magnetic field. Two samples were used in the experiments as substrates, Cu(100) and Ag(100).

The Cu(100) single crystal sample was a 10 mm diameter by 3 mm thick disk and the Ag(100) single crystal sample was a 15 mm diameter by 4 mm thick disk. Before being mounted on the sample manipulator, the samples were first mechanically polished with alumina powder of sizes 5 μm, 1 μm, 0.3 μm, and, eventually, with deagglomerated alumina powder of size 0.05 μm. The surfaces should be shiny with no visual scratches observable after polishing. The samples were then cleaned by acetone and methanol in the ultra-sonic bath tank for three hours and one hour successively. Finally the samples were mounted on button heaters, attached to the sample holder of the manipulator, and introduced in to the ultrahigh vacuum chamber.

With the pressure in the experimental chamber in the 10^{-10} torr range the Cu(100) sample was first annealed to 600°C for one hour. The sample was then sputtered with 1.5 keV Ar ion beam of 10 $\mu A/cm^2$ at 45° incident angle for an hour and annealed at 600°C for 20 minutes. This sputtering-annealing cycle was repeated 8 to 10 times until no carbon and oxygen or surface contamination peaks were seen in both the Auger and XPS spectra. For the Ag(100) sample the energy of the Ar ion sputtering beam was 1 keV instead of 1.5 keV and the annealing temperature was 400°C instead of 600°C.

Resistive heating methods were used to grow the thin films. The growth rate of each evaporant was calibrated by AES before each experiment. Also, the film thickness was calibrated by AES before and after each experiment.

If we have a sample **B** covered with n monolayers of **A**, the AES peak-to-peak ratio will be

$$r = \frac{I^{\mathrm{A}}(E)}{I^{\mathrm{B}}(E')} = \frac{I_{\mathrm{o}}^{\mathrm{A}}(E)}{I_{\mathrm{o}}^{\mathrm{B}}(E')} \frac{1 - e^{-na/\lambda(E)}}{e^{-na/\lambda(E)}} = R\left(e^{na/\lambda(E)} - 1\right), \qquad (5.1)$$

where $I_o^A(E)$ and $I_o^B(E')$ are the AES peak-to-peak heights of the clean surfaces for **A** and **B** at energy E and E', respectively, $\lambda(E)$ is the electron mean-free-path of **A** at energy E, a is the monolayer thickness of **A**, and $R = I_o^A(E)/I_o^B(E')$. Therefore, if $\lambda(E)$, R, and a are known, the number of monolayers of **A** can be derived from the peak-to-peak ratio of the AES spectra. The constants d and $\lambda(E)$ for different materials usually can be found in the papers.[5.6, 5.7] The ratio R can be estimated from the AES handbook[5.8] of normalized AES spectra.

Figure 5.1 shows the growth of Fe on Ag(100) at room temperature. The R value was estimated from spectra in the handbook[5.8] and the constants $a = 1.43$ Å[5.6] and $\lambda(E) = 12.3$ Å[5.7] (at $E = 700$ eV) were used. Since Fe forms an alloy with W and the melting point of the alloy is higher than W, we can see from figure 5.1 that the growth rate is no longer a constant but decreases exponentially. Two identical Fe sources were mounted adjacent to each other. Calibration of one provided a rough estimate of the growth rate from the other.

The Co evaporator source consisted of a 5 mm diameter by 3 mm thick disk with 99.995% purity, obtained from AESAR Johnson Matthey Inc. The Fe sources were 0.005" wires with 99.995% purity, supplied from the same company. Both sources were cleaned by ethanol (or methanol) in an ultra-sonic bath before being put into the W baskets made of 0.015" wire, and introduced into the ultrahigh vacuum chamber. The sources were out-gassed over night during the baking.

Before taking each spin polarized spectrum, fresh Au was evaporated on the target of the spin detector. For simple systems such as Co and Fe films, the film was grown on the substrate until no substrate signal was seen in the spectrum. A typical 3p spin polarized XPS spectrum for the simple systems takes approximately one hour. AES spectra were taken both before and after each XPS

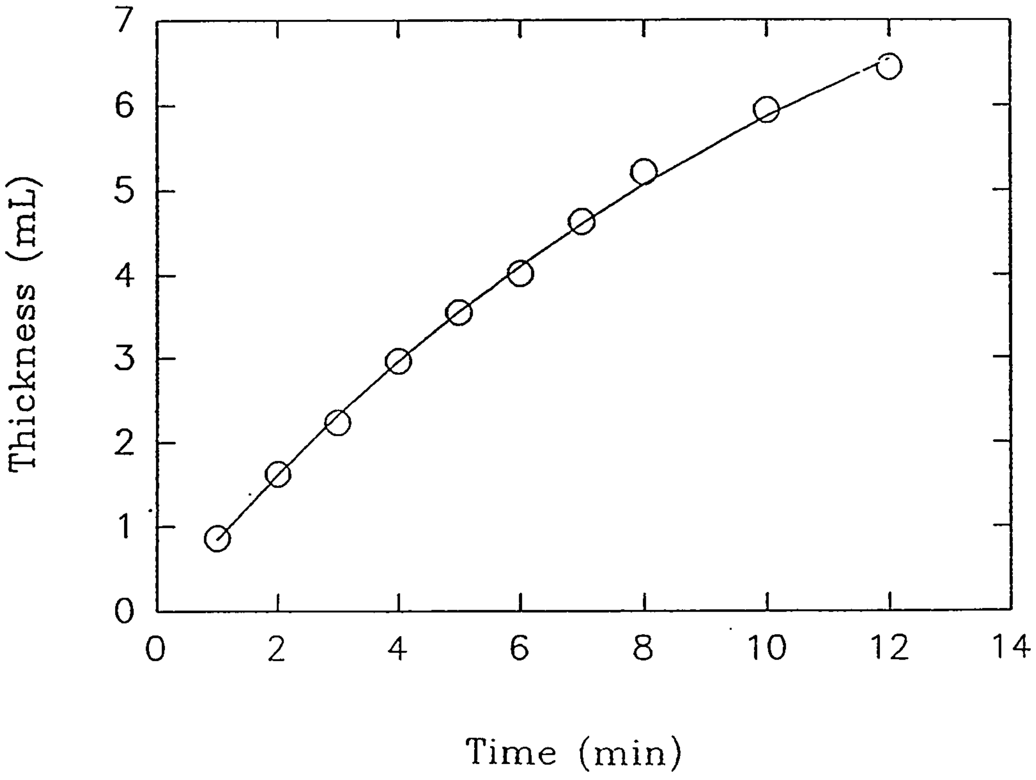

Figure 5.1 Overlayer growth rate of Fe on Ag(100) at room temperature.

spectrum. With the base pressure of the chamber at 2 × 10^{-10} torr, there were no significant sample contamination during the experimental time period.

5.3 Fe and Co 3*p* Core Level Spin Polarized XPS Spectra

Previous spin polarized core level XPS spectra performed at 145 eV[5.9-12] photon energy have shown that the Fe and Co 3*p* core level spectra are spin dependent. Our data for a photon energy of 250 eV are shown in figure 5.2 and 5.3. These spectra are recorded from Fe and Co thin films grown on Ag(100) and Cu(100) respectively. The thickness of the films were over 20 Å. The spectra were taken in normal emission, with the photon incident at 45°. The samples were in-plane *p*-polarized, i.e. the magnetization direction was perpendicular to the polarization of the photon beam and parallel to the sample plane. Because of the relatively high kinetic energies of the 3*p* photoelectrons, the backgrounds are flat on both sides of the spectra.

The experimental results again show that, for both materials, the 3*p* core level spectra are spin dependent. The peak energies and line shapes of the majority and minority 3*p* energy distribution curves differ significantly for each set of spectra. The line shapes of minority curves are narrower and lie at lower binding energy while the line shapes of majority curves are broader and lie at higher binding energies. The splitting is 0.45 eV for Fe and 0.2 eV for Co. The linewidths of the peaks in the two spin channels differ more in Fe than in Co. For the Fe spectra, the full width at half maximum (FWHM) of the majority peak is 2.5 eV and that of the minority is 1.7 eV. For the Co spectra, the FWHM of the majority peak is 2.4 eV and that of the minority is 2.0 eV. These parameters are in agreement with the previous experimental results obtained by the other groups.[5.9-12]

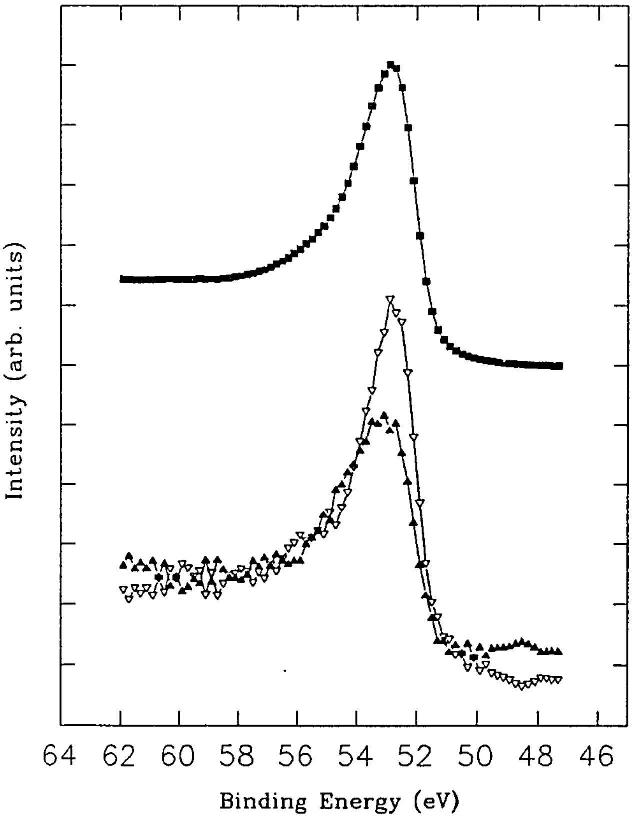

Figure 5.2 Spin polarized XPS spectra of Fe 3*p* from Fe/Ag(100). hν = 250 eV. Solid squires: spin integrated curve, open triangles: minority spin curve, solid triangles: majority spin curve.

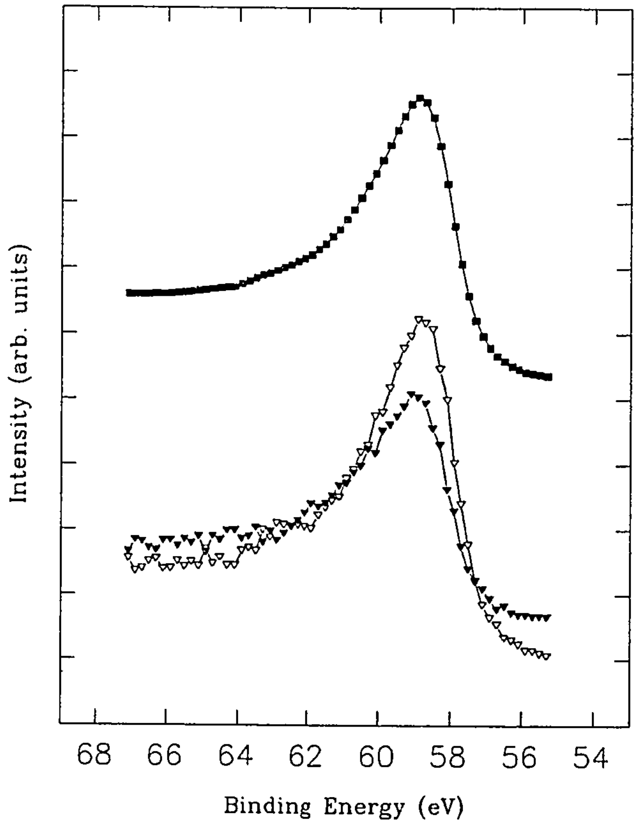

Figure 5.3 Spin polarized XPS spectra of Co $3p$ from Co/Cu(100). hν = 250 eV. Solid squires: spin integrated curve, open triangles: minority spin curve, solid triangles: majority spin curve.

5.4 Introduction to the Model of *p* Core Level Spin Polarized XPS

In chapter 1 section 3, we have already discussed the 3*s* core level spin polarized XPS spectra. There we indicated that there should be three peaks involved in the spectra, two in the majority channel with broader line shapes and one in the minority channel with narrower line shape. The latter is degenerate with one of the majority peaks lying at lower binding energy. Consequently, using a single Doniach-Sunjic line shape[5.13] to fit the lower binding energy peaks with different line widths[5.14, 5.15] is clearly inappropriate. The interpretation of the *s* level splitting is based essentially on the different electrostatic exchange interaction of spin parallel and antiparallel states of the remaining core electron with the unpaired valence electrons. Bagus *et al.*[5.16] have incorporated the effect of correlation and showed it to be of great significance in explaining the splittings in 3*s* core level spectra.

The simple exchange interaction mechanism which is so useful for *s* levels is rather inadequate for *p* levels. The reason is that the orbital angular momenta participate in the interaction. In the atomic case, the *p* electrons can couple with various parent terms of the ion giving more than two final terms with the same orbital and spin angular momenta as would be obtained through coupling of the *p* hole with the ground state term only. It is then necessary to consider all final terms since the eigenstates will be combinations of the final terms having the same orbital and spin angular momenta. Further more, those configurations of the ion which form appropriate final terms should be also included.

In the case of a 3*p* hole, the interactions mainly include the *p-d* interactions, the *d-d* interactions, and the spin-orbit interaction of a *p* hole and the crystal field. Among these interactions, the *p-d* interactions are predominant in giving the multiplet structure in the spectra.[5.17] Fortunately, due to the orbital quenching,[5.18] we can neglect the valence *d* level electron orbital angular momentum for the 3*d* transition metals in this *p*-*d* interaction.

The electron spin polarization measurement yields information on the electron spin components. The photoelectron spin polarization determines the spin in the final state. The total momentum operator commutes with the Hamiltonian for the final state upon photoionization, but the core hole spin, valence electron spin and orbital operators do not. In order to obtain the total angular momentum dependence of the photoelectron spin in the final state, the spin component of the core electrons must be traced through the whole coupling procedure.

In order to simplify the picture, we exclude the crystal field effect. Thus, upon magnetization, the total angular momentum of the *d* electrons in this scheme is the total spin angular momentum of the *d* electrons $S_d = \sum_i s_i$, where we sum over the individual spins. The total angular momentum component of these *d* electrons will be $M_{S_d} = S_d$, This can be expanded further into different *d* electron configurations with integral number half.[5.19]

Within a single configuration, the *p* hole splits further into two peaks, ${}^{2S_d+2}P$ and ${}^{2S_d}P$, due to spin angular momentum coupling. If $\psi(j,m_j)$ is the wave function after coupling, we have for ${}^{2S_d+2}P$

$$\psi\left(S_d+\frac{1}{2},S_d+\frac{1}{2}\right)=\varphi(S_d,S_d)\alpha \tag{5.2}$$

$$\psi\left(S_d+\frac{1}{2},S_d-\frac{1}{2}\right)=\sqrt{\frac{1}{2S_d+1}}\varphi(S_d,S_d)\beta \tag{5.3}$$

and for ${}^{2S_d}P$

$$\psi\left(S_d-\frac{1}{2},S_d-\frac{1}{2}\right)=\sqrt{\frac{S_d}{2S_d+1}}\varphi(S_d,S_d)\beta, \tag{5.4}$$

where $\varphi(S_d, S_d)$ is the spin angular momentum wave function of the d electrons; α and β are the spin part of the core electron wave function corresponding to $m_s = 1/2$ and $-1/2$ respectively.

We now introduce the orbital component of the core hole. The coupling of the spin and orbital angular momenta yields for the ${}^{2S_d+2}P$ multiplet

$$\Psi\left(S_d+\frac{3}{2}, S_d+\frac{3}{2}\right) = \varphi(S_d, S_d)\phi(1,1)\alpha \tag{5.5}$$

$$\Psi\left(S_d+\frac{3}{2}, S_d+\frac{1}{2}\right) = \sqrt{\frac{3}{2S_d+3}}\varphi(S_d, S_d) \left(\sqrt{\frac{2}{3}}\phi(1,0)\alpha + \sqrt{\frac{1}{3}}\phi(1,1)\beta\right) \tag{5.6}$$

$$\Psi\left(S_d+\frac{3}{2}, S_d-\frac{1}{2}\right) = \sqrt{\frac{3}{(S_d+1)(2S_d+3)}}\varphi(S_d, S_d) \left(\sqrt{\frac{1}{3}}\phi(1,-1)\alpha + \sqrt{\frac{2}{3}}\phi(1,0)\beta\right) \tag{5.7}$$

$$\Psi\left(S_d+\frac{3}{2}, S_d-\frac{3}{2}\right) = \sqrt{\frac{3}{(S_d+1)(2S_d+1)(2S_d+3)}} \varphi(S_d, S_d)\phi(1,-1)\beta \tag{5.8}$$

$$\Psi\left(S_d+\frac{1}{2}, S_d+\frac{1}{2}\right) = \sqrt{\frac{1}{2S_d+3}}\varphi(S_d, S_d) \left(\sqrt{2S_d+1}\phi(1,0)\alpha - \sqrt{\frac{1}{2S_d+1}}\phi(1,1)\beta\right) \tag{5.9}$$

$$\Psi\left(S_d+\frac{1}{2}, S_d-\frac{1}{2}\right) = \sqrt{\frac{1}{2S_d+3}}\varphi(S_d, S_d) \left(2\phi(1,-1)\alpha + \frac{2S_d-1}{2S_d+1}\phi(1,0)\beta\right) \tag{5.10}$$

$$\Psi\left(S_d+\frac{1}{2},S_d-\frac{3}{2}\right)=\sqrt{\frac{8S_d}{(2S_d+1)^2(2S_d+3)}}\varphi(S_d,S_d)\phi(1,-1)\beta \tag{5.11}$$

$$\Psi\left(S_d-\frac{1}{2},S_d-\frac{1}{2}\right)=\sqrt{\frac{S_d}{S_d+1}}\varphi(S_d,S_d)$$

$$\left(\phi(1,-1)\alpha-\frac{\sqrt{2}}{2S_d+1}\phi(1,0)\beta\right) \tag{5.12}$$

$$\Psi\left(S_d-\frac{1}{2},S_d-\frac{3}{2}\right)=\sqrt{\frac{S_d(2S_d-1)}{(2S_d+1)^2(S_d+1)}}\varphi(S_d,S_d)\phi(1,-1)\beta \tag{5.13}$$

were the $\Psi(J,m_J)$ represent the wave function after the spin-orbit coupling. For the ${}^{2S_d}P$ multiplet we find

$$\Psi\left(S_d+\frac{1}{2},S_d+\frac{1}{2}\right)=\sqrt{\frac{2S_d}{2S_d+1}}\varphi(S_d,S_d)\phi(1,1)\beta \tag{5.14}$$

$$\Psi\left(S_d+\frac{1}{2},S_d-\frac{1}{2}\right)=\sqrt{\frac{4S_d}{(2S_d+1)^2}}\varphi(S_d,S_d)\phi(1,0)\beta \tag{5.15}$$

$$\Psi\left(S_d+\frac{1}{2},S_d-\frac{3}{2}\right)=\sqrt{\frac{2S_d}{S_d(2S_d+1)^2}}\varphi(S_d,S_d)\phi(1,-1)\beta \tag{5.16}$$

$$\Psi\left(S_d-\frac{1}{2},S_d-\frac{1}{2}\right)=\sqrt{\frac{2S_d(2S_d+1)}{(2S_d+1)^2}}\varphi(S_d,S_d)\phi(1,0)\beta \tag{5.17}$$

$$\Psi\left(S_d-\frac{1}{2},S_d-\frac{3}{2}\right)=\sqrt{\frac{4S_d}{(2S_d+1)^2}}\varphi(S_d,S_d)\phi(1,-1)\beta \tag{5.18}$$

$$\Psi\left(S_d-\frac{3}{2},S_d-\frac{3}{2}\right)=\sqrt{\frac{2(S_d-1)}{2S_d+1}}\varphi(S_d,S_d)\phi(1,-1)\beta. \tag{5.19}$$

In the absence of a magnetic field, the ${}^{2S_d+2}P$ peak will split into ${}^{2S_d+2}P_{S_d+3/2}$, ${}^{2S_d+2}P_{S_d+1/2}$, and ${}^{2S_d+2}P_{S_d-1/2}$, with binding energies in ascending order. However the intensity of XPS spectra must be proportional to

$$I(J,m_J)=\sum_m\left|\langle j_1m_1;j_2m_2\,|\,jm\rangle\right|^2=\sum_m\left|\langle j_1m_1;j_2m-m_1\,|\,jm\rangle\right|^2 \tag{5.20}$$

where $\langle j_1m_1;j_2m_2\,|\,jm\rangle=\langle j_1m_1;j_2m-m_1\,|\,jm\rangle$ is the standard CG coefficient. For the majority energy distribution curve, $m_s=-1/2$ (β), we have

$$I_{\mathrm{maj}}\left(S_d+\frac{3}{2}\right)=\frac{S_d+2}{(S_d+1)(2S_d+1)} \tag{5.21}$$

$$I_{\mathrm{maj}}\left(S_d+\frac{1}{2}\right)=\frac{1}{2S_d+1} \tag{5.22}$$

$$I_{\mathrm{maj}}\left(S_d-\frac{1}{2}\right)=\frac{S_d}{(S_d+1)(2S_d+1)} \tag{5.23}$$

and for the minority energy distribution curve, $m_s=+1/2$ (α), we have

$$I_{\mathrm{min}}\left(S_d+\frac{3}{2}\right)=\frac{S_d+2}{S_d+1} \tag{5.24}$$

$$I_{\mathrm{min}}\left(S_d+\frac{1}{2}\right)=1 \tag{5.25}$$

$$I_{\mathrm{min}}\left(S_d-\frac{1}{2}\right)=\frac{S_d}{S_d+1} \tag{5.26}$$

Therefore the intensity ratios between the three peaks corresponding to the majority spin are the same as the ratios between the three peaks corresponding to the minority spin. i.e.

$$R_\sigma=I_\sigma\left(S_d+\frac{3}{2}\right):I_\sigma\left(S_d+\frac{1}{2}\right):I_\sigma\left(S_d-\frac{1}{2}\right)=(S_d+2):(S_d+1):S_d \tag{5.27}$$

where $R_\sigma=R_{\mathrm{maj}}$, R_{min}, and $R_{\mathrm{maj}}+R_{\mathrm{min}}$; $I_\sigma=I_{\mathrm{maj}}$, I_{min}, and $I_{\mathrm{maj}}+I_{\mathrm{min}}$.

The ratios of the same majority and minority spin components are equal. i.e.

$$R(S_d+k)=\frac{I_{\mathrm{maj}}(S_d+k)}{I_{\mathrm{min}}(S_d+k)}=\frac{1}{2S_d+1} \tag{5.28}$$

where $k = 3/2$, $1/2$, and $-1/2$.

Again in the absence of a magnetic field, the ${}^{2S_d}P$ peak splits into three peaks, ${}^{2S_d}P_{S_d+1/2}$, ${}^{2S_d}P_{S_d-1/2}$, and ${}^{2S_d}P_{S_d-3/2}$, with binding energies in ascending order. As before the intensity of the different components will be

$$I_{\mathrm{maj}}\left(S_d+\frac{1}{2}\right)=\frac{2(S_d+1)}{2S_d+1} \tag{5.29}$$

$$I_{\mathrm{maj}}\left(S_d-\frac{1}{2}\right)=\frac{2S_d}{2S_d+1} \tag{5.30}$$

$$I_{\mathrm{maj}}\left(S_d-\frac{3}{2}\right)=\frac{2(S_d-1)}{2S_d+1} \tag{5.31}$$

Contrary to the ${}^{2S_d+2}P$ multiplet, the ${}^{2S_d}P$ multiplet does not have minority components. The intensity ratios between the peaks are now

$$R_\sigma=I_\sigma\left(S_d+\frac{1}{2}\right):I_\sigma\left(S_d-\frac{1}{2}\right):I_\sigma\left(S_d-\frac{3}{2}\right)=(S_d+1):S_d:(S_d-1) \tag{5.32}$$

where $R_\sigma = R_{\mathrm{maj}}$ in this case.

The ratio of the total intensities of the majority curve and minority curve for both ${}^{2S_d+2}P$ and ${}^{2S_d}P$ peaks is

$$R_{\mathrm{maj/min}}=\frac{\sum I_{\mathrm{maj}}\left({}^{2S_d+2}P\right)+\sum I_{\mathrm{maj}}\left({}^{2S_d}P\right)}{\sum I_{\mathrm{min}}\left({}^{2S_d+2}P\right)}=1 \tag{5.33}$$

as we expected since the spin of the core level electrons is paired off.

In this simple picture, the Hamiltonian for an N-electron system in this approximation is,

$$H = H^0 + V^0 + V^1 \qquad (5.34)$$

where $H^0 = \sum_{i=1}^{N}\left[\frac{p^2(i)}{2m} - \frac{Ze^2}{r_i}\right]$ represents the one electron terms, $V^0 = \sum_{i<j}\frac{e^2}{r_{ij}}$ is Coulomb or two electron terms, and $V^1 = \sum_{i=1}^{N}\xi(i)S(i)\cdot L(i)$ is the spin-orbit interaction. By using the LSM-coupling scheme, the energy estimated for the diagonal matrix elements of H is then

$$E = E_0 + \sum_k f_k F^k(nln'l') + \sum_k g^k G^k(nln'l') +$$
$$\frac{1}{2}[J(J+1) - L(L+1) - S(S+1)]\zeta(SL) \qquad (5.35)$$

where f_k and g_k are constants, F^k and G^k are the Slater exchange integrals, and $\zeta(SL)$ is the radial spin-orbit factor. If we treat the d electrons as in a single configuration, the splitting between the ${}^{2S_d+2}P$ peaks and ${}^{2S_d}P$ peaks is[5.20]

$$\Delta E = (2S_d + 1)\left(a_1 G^1(3p,3d) + a_3 G^3(3p,3d)\right) \qquad (5.36)$$

where a_i are constants and G^i are the Slater exchange integrals between the $3p$ electrons and the $3d$ electrons. The evaluation of the integrals is not trivial, since the real form of the d electron wave functions are hybridized with s and p electrons.

The splittings among the ${}^{2S_d+2}P_J$ peaks and ${}^{2S_d}P_J$ peaks caused by the spin-orbit interaction are[5.21]

$$\Delta E_J = E_J - E_{J-1} = J\zeta(3p) \qquad (5.37)$$

where $\zeta(3p)$ is the radial factor of the $3p$ electron.

For $3d$ transition metals, the d electrons are hopping from site to site with averaged total spin imbalance S at the site of each atom. The neutron diffraction process takes ~ 10^{-12} s, about the order of the moment fluctuation time, and hence the measured results represent averaged moments. The XPS process, however occurs in only 10^{-15} s. Therefore configuration interaction will influence core level XPS, and will lead to more satellite lines in the spectra. The total spin angular momentum in this case then is the coupling of the spin angular momentum of the core hole and the configuration spin angular momentum of *d* electrons at the site instead of that of the localized *d* electrons.

The multiplet splittings of *p* levels have been explicitly calculated for 3*d* transition metals in the Hartree-Fock approximation.[5.17, 5.22, 5.23] The results qualitatively agree with spin integrated XPS experimental data but quantitatively the agreement is poor.

Let us examine the Fe and Co 3*p* spin polarized XPS spectra by using our simple model described above. Although the configuration interaction plays an significant roll in determining the energy destribution of a spectrum, it has been shown that there exists always a predominant configuration.[5.16] In order to simplify the picture, we consider only a single dominant configuration by choosing $\mu = 2S_d = 2$ for Fe and $\mu = 2S_d = 1$ for Co. We will describe the picture within a single *d* electron configuration. Substituting into equations (5.21) — (5.26) and (5.29) — (5.31), we obtain the intensities for both spin majority and minority peaks of Fe and Co 3*p* spin polarized XPS spectra.

Figure 5.4 shows the Fe and Co 3*p* spectra generated by the calculated values within the Hartree-Fock approximation. To simplify the picture, a broadening of Lorentzian line shape is used instead of an asymmetric (Doniac-Sunjic) line shape.[5.13] Numerical values of Slater-Condon parameters for the *p-d* interactions are from Watson's work[5.24] and those of the 3*p* spin-orbit interaction parameters are from Satoko and Sugano's work.[5.25] Since the full-width-half-maximum of the overall minority curve of the experimental data is

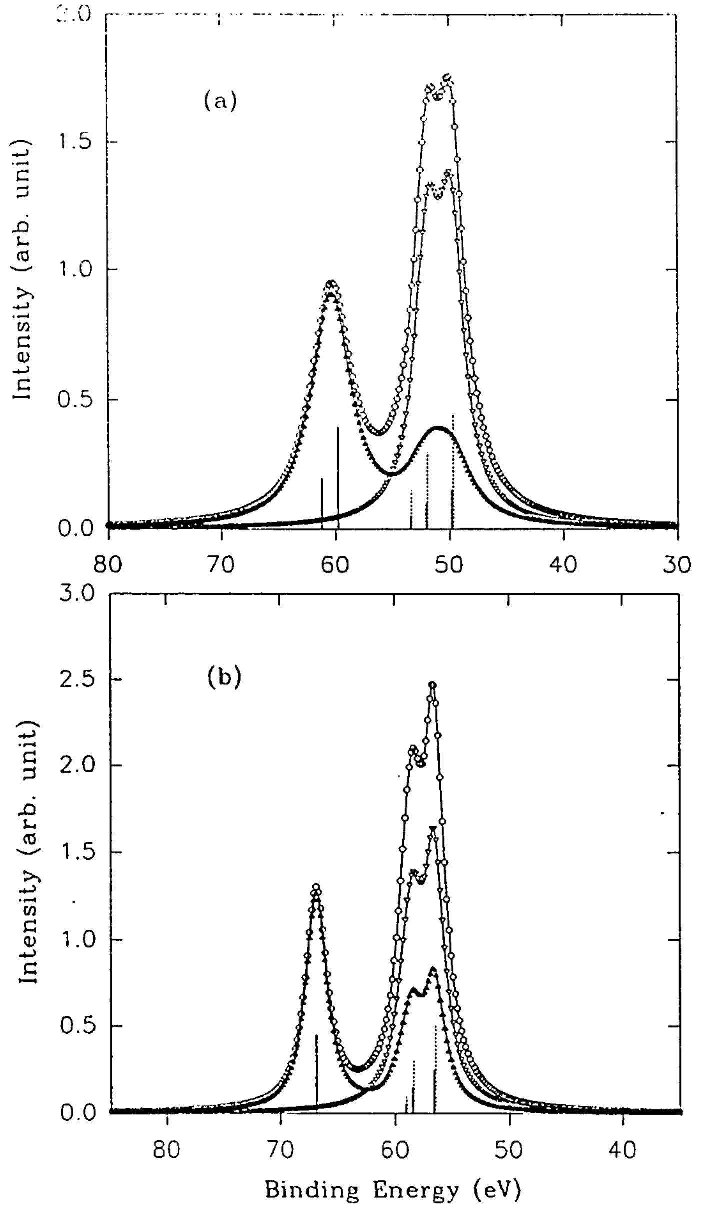

Figure 5.4 Calculated spin polarized $3p$ core level XPS spectra of (a) Fe and (b) Co with Hartree-Fock approximation. The parametes used in the calculation are as follows: G^1, G^3, and ζ_{3p} are 12.78, 7.63, and 1.17 eV for Fe and 13.76, 8.23, and 1.41 eV for Co.[5.24,5.25] Dashed (solid) lines show minority (majority) spectra lines. Open dots: spin integrated curve, open triangles: minority spin curve, solid triangles: majority spin curve.

1.7 eV, the Lorentzian linewidth Γ = 1.4 eV is chosen. The integrated spectra in figure 5.4 are similar to those obtained in previous calculations.[5.17, 5.22, 5.23] The overall majority-minority splitting reflects the center-of-weight splitting between the majority peaks and minority peaks. It clearly shows that the Hartree-Fock approximation over estimates the interactions between the electrons. This again indicates that the configuration interaction reduces multiplet splitting significantly, for the case of 3*s* spectra, by a factor of two comparing with the results from the Hartree-Fock approximation calculations.[5.16] Due to screening and configuration interaction, the real interactions between the valence electrons and 3*p* core level electrons in solids may be reduced by a factor of ten.

Figure 5.5 (b), (c), and (d) show the Fe spectra in figure 5.4 (a) with the interactions scaled down by a factor of 2, 5, and 10 respectively. Figure 5.6 shows the Fe spectra with the interactions scaled down by a factor of 12. This is in reasonable agreement with the experimental data show in figure 5.2, which shows an overall majority-minority splitting of 0.45 eV. The splitting caused by the exchange interaction is therefore 0.75 eV

Figure 5.7 shows the Co 3*p* spectra generated by the calculated values broadened with a Lorentzian of Γ = 1.8 eV. The multiplet splittings have bee scaled down by a factor of 12 as we did for Fe in order to compare to the experimental data, which yields a exchange splitting of 0.58 eV. The results are in agreement with the experimental data show in figure 5.3 with overall majority-minority splitting of 0.2 eV.

Therefore, within our simple model, the intensity distribution and the splitting between the majority and minority curves of the 3*p* spin polarized XPS spectra do reflect the exchange interaction between the *d* electrons and *p* electrons. Since the exchange interaction is proportional to the local magnetic

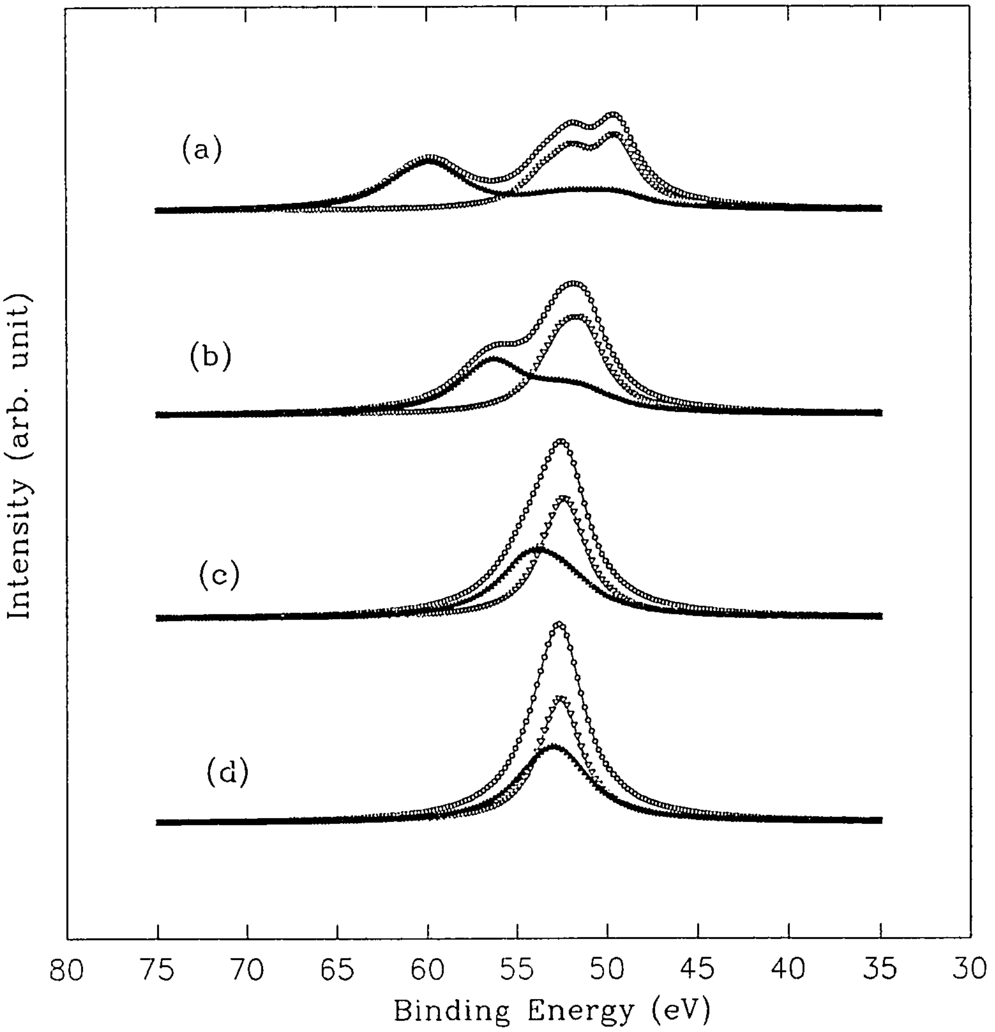

Figure 5.5 Calculated spin polarized $3p$ core level XPS spectra of Fe with interactions scaled down with different factors (see text). Open dots are spin integrated curves, solid triangles are majority curves and open triangles are minority curves.

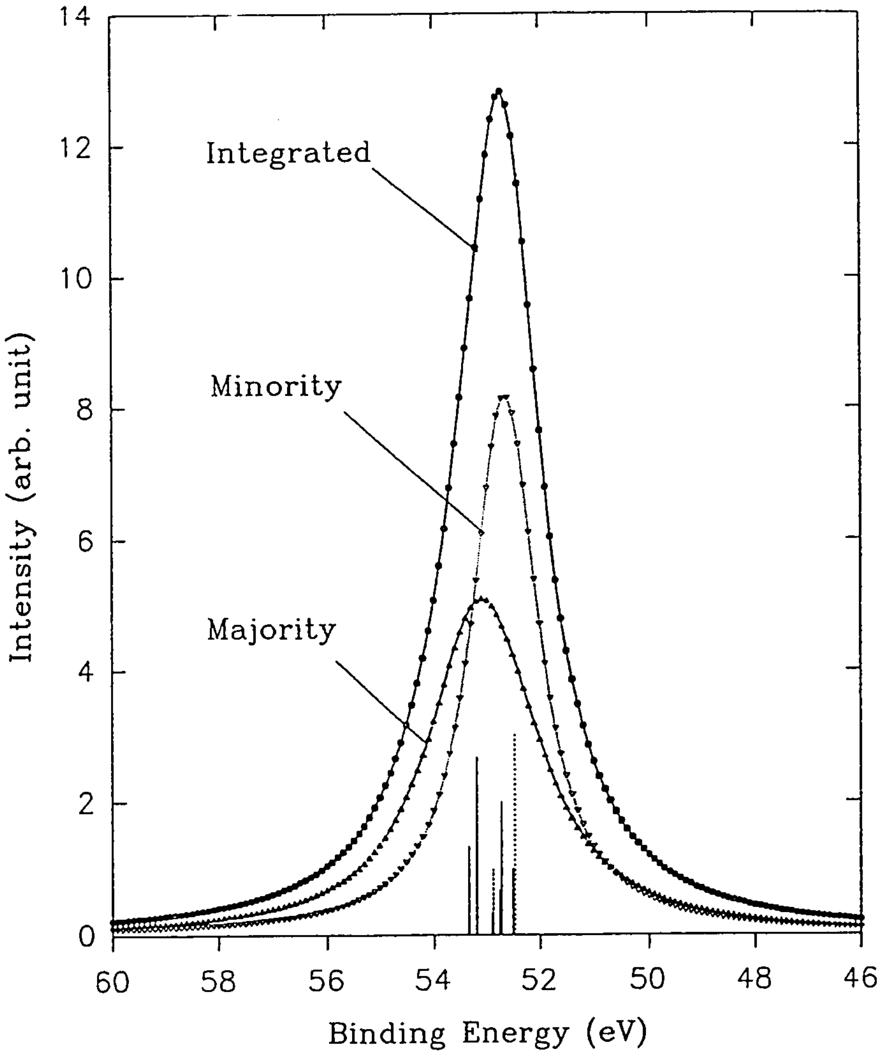

Figure 5.6 Calculated spin polarized $3p$ core level XPS spectra of Fe. Dashed (solid) lines show minority (majority) spectra lines.

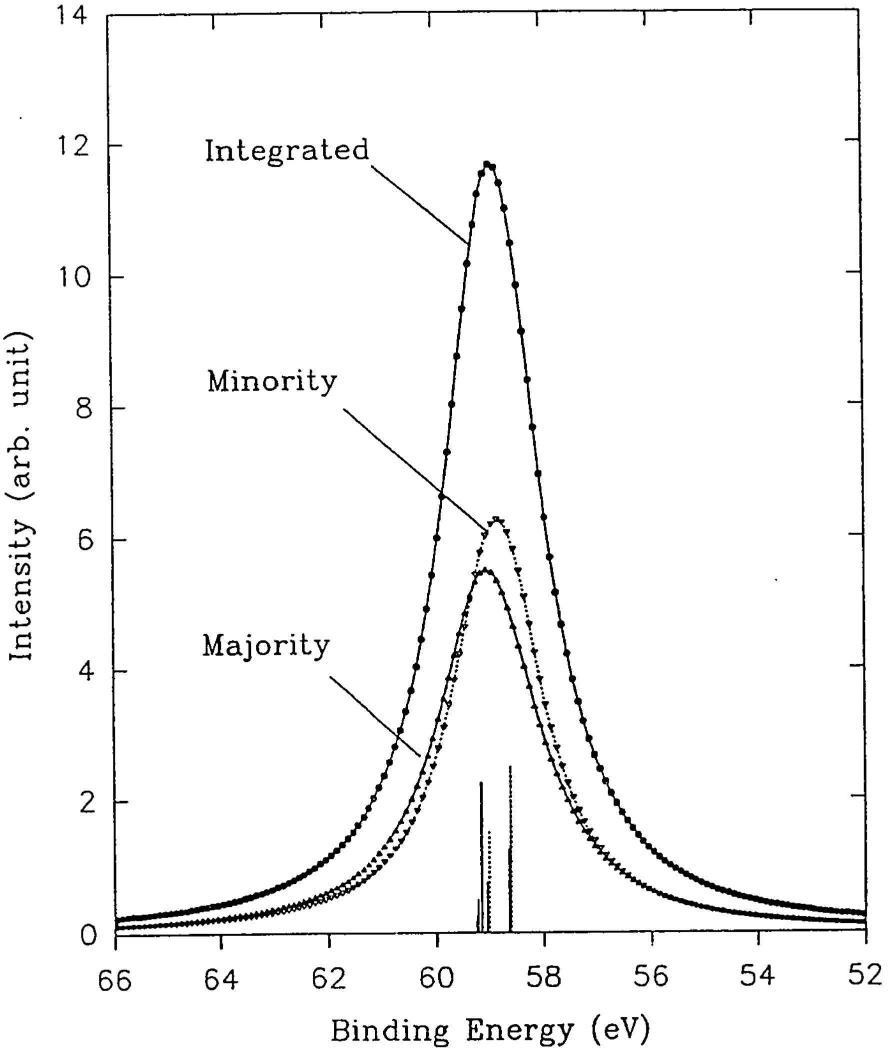

Figure 5.7 Calculated spin polarized 3*p* core level XPS spectra of Co. Dashed (solid) lines show minority (majority) spectra lines.

moment, some estimate of the moment can be obtained from the lineshape and the splitting of the majority and minority curves.

If we now consider the $2p$ core level, the spin-orbit interaction of the p hole is one order of magnitude larger than the other interactions. The spectra consist of two main peaks due to the spin-orbit splitting of the p level and these peaks are broadened by the other interactions to have a width of about 1 eV.[5.17] Within the same picture, the p hole spin-orbit interaction first splits the into two main peaks, the $p_{1/2}$ and the $p_{3/2}$ multiplets. The p-d interaction further splits the $p_{1/2}$ multiplet into two peaks and the $p_{3/2}$ into four peaks in both the majority and minority curves. The details of the $2p$ core level spectra intensity ratios are described in appendix 6. In this case, the splitting between the majority and minority peaks for both $p_{1/2}$ and $p_{3/2}$ reflect the intensity competition between the majority and minority peaks.

Figure 5.8 shows the Fe $2p_{1/2}$ core level spin polarized XPS spectra generated by the calculated values broadened with a Lorentzian of $\Gamma = 2$ eV. Exchange interaction of 0.3 eV is chosen by scaling down the parameters obtained from Watson's work[5.24] a factor of 12 again. This yields the overall majority-minority splitting of -0.1 eV. The minus sign here indicates that the majority peak lies at lower binding energy. Figure 5.9 shows the spectra calculated Fe $2p_{3/2}$. The Lorentzian of $\Gamma = 1.7$ eV, and the same exchange splitting of 0.3 eV are chosen. The overall majority-minority splitting becomes 0.48 eV. This is quite significant because it shows that the overall majority-minority curve splitting of $2p_{3/2}$ spectra is larger than that of $3p$ spectra though the exchange splitting of $2p_{3/2}$ spectra is much smaller than that of $3p$'s. It can, in principle, be proved experimentally.

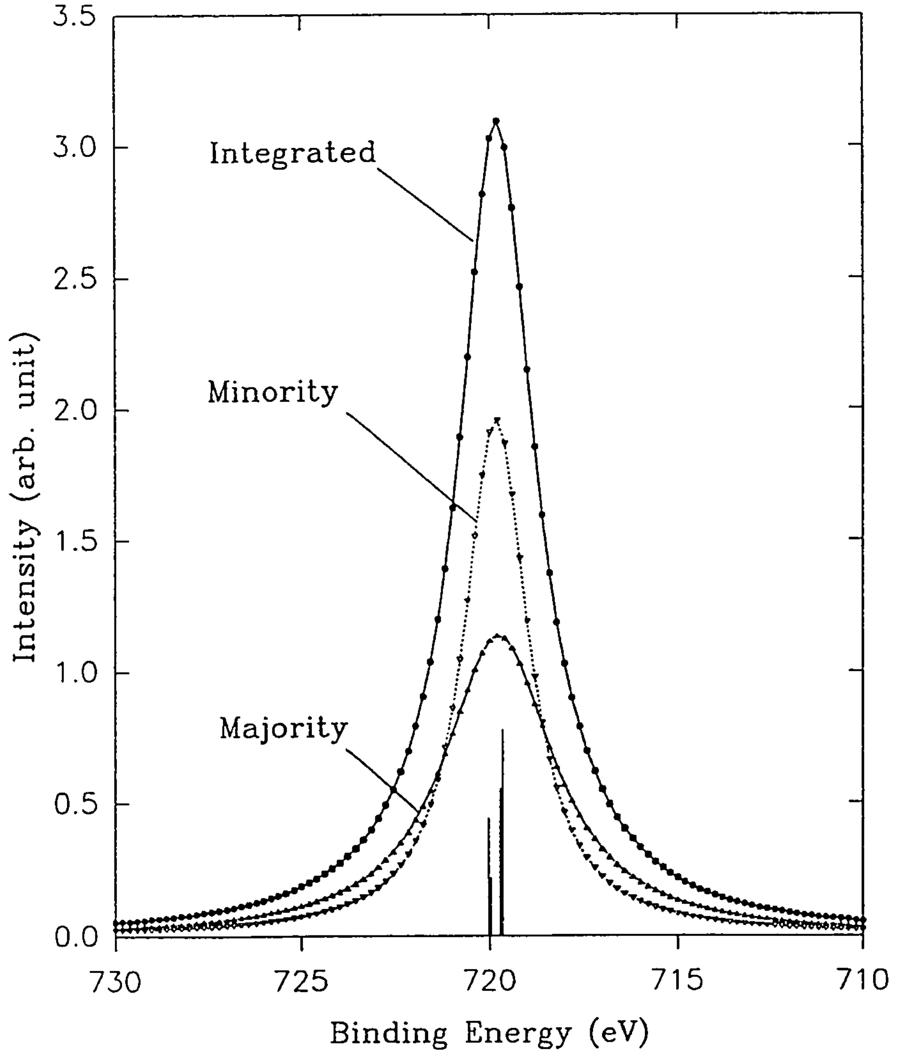

Figure 5.8 Calculated spin polarized $2p_{1/2}$ core level XPS spectra of Fe. Dashed (solid) lines show minority (majority) spectra lines.

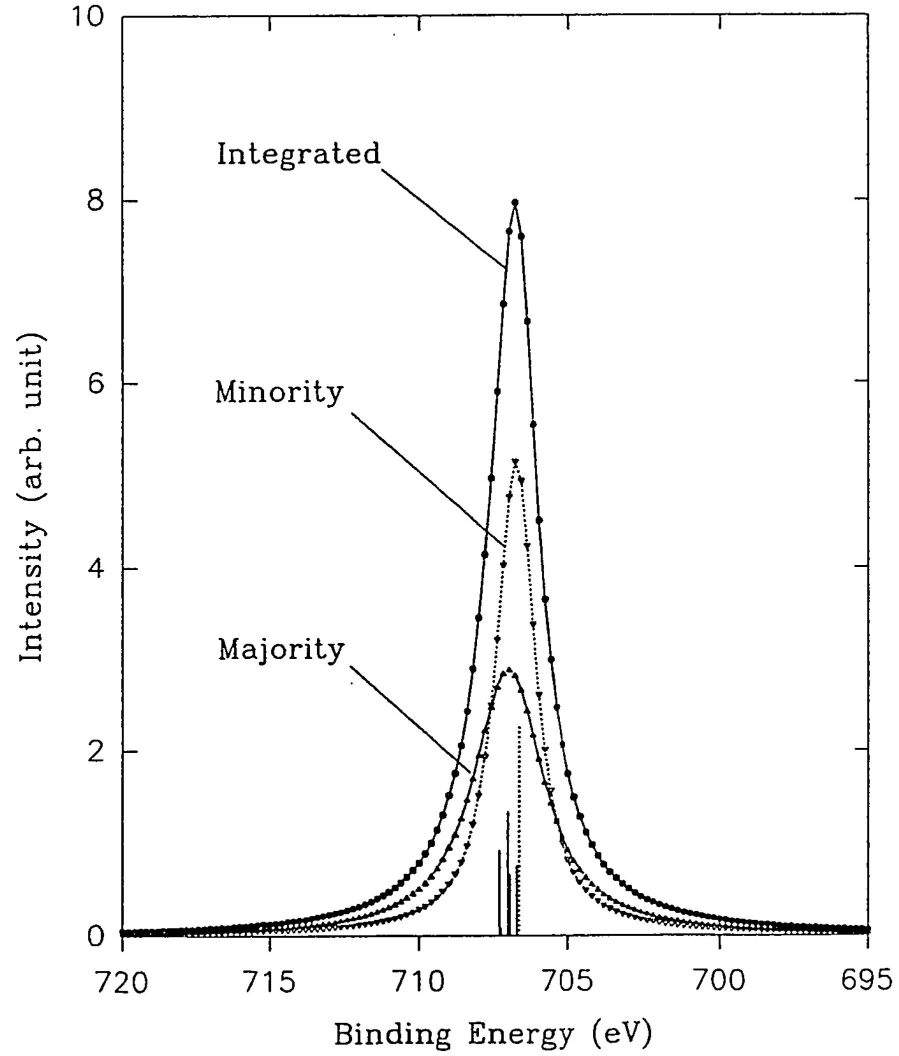

Figure 5.9 Calculated spin polarized $2p_{3/2}$ core level XPS spectra of Fe. Dashed (solid) lines show minority (majority) spectra lines.

Chapter 6. Magnetic Properties of Cr and Mn Overlayers on Fe(100)

6.1 Introduction

Magnetic coupling phenomena in surface, interface and thin film structures has attracted considerable attention in recent years[6.1] because artificial layered structures present novel magnetic properties. An example of this is the coupling of antiferromagnetic (AFM) thin film Cr on ferromagnetic (FM) Fe. Walker *et al.*[6.2] studied the magnetic ordering at the surface of epitaxial Cr overlayers on Fe(100) with spin polarized electron-energy-loss spectroscopy (SPEEL). The authors found that an exchange asymmetry in the scattering oscillates with the thickness of the Cr overlayer and that the spin-flip spectrum broadens toward lower energy with increasing thickness This indicates that the surface Cr layer has a net ferromagnetic moment and that successive layers order antiferromagnetically and that the Cr has a surface-enhanced magnetic moment. The same system has also been studied with scanning electron microscopy with polarization analysis (SEMPA)[6.3] and valence band spin polarized photoemission spectroscopy,[6.4] The same conclusions were obtained. Unfortunately, these probes only yield the averaged magnetic information of both the Cr and Fe. One other way to approach the problem is to study sandwich or superlattice systems of Fe/Cr/Fe. It has been demonstrated with different techniques that the epitaxial Fe/Cr/Fe(100) system exhibits Fe AFM coupling for certain Cr thicknesses.[6.5-11]

It has been known for decades that bcc structured bulk Cr is AFM with Néel temperature T_N = 311 K.[6.12] Its AFM ground state is modulated by an incommensurate spin density wave (SDW). The periodicity of the SDW in each of the ⟨100⟩ directions is approximately 21 lattice spacings. The magnetic moment at the maximum of the SDW is 0.59 Bohr magnetons. The AFM SDW demands nearest-neighbor atoms to possess antiparallel magnetic moments. The incommensurate AFM SDW of Cr exhibits a great richness of phenomena and has been studied for many years.[6.13]

Figure 6.1 shows the magnetic lattice of the bcc Cr AFM state. In this structure, atoms in the corner positions have moments pointing in one direction and the atoms in the body-centered positions have moments in the opposite direction. This simple AFM structure requires that moments in the ⟨100⟩ planes are ferromagnetically aligned. Naturally, from figure 6.1, one would think that if we put one monolayer Cr on Fe(100) surface, the Cr monolayer is expected to be ferromagnetically aligned and antiferromagnetically coupled to Fe(100) substrate as shown in figure 6.2, since the lattice parameter of Cr is almost identical to that of Fe.

Victora and Falicov[6.14] have carried out a theoretical calculation of the electronic and magnetic structures of Cr surfaces and Cr monolayers on Fe(100). The theoretical results indicate that the Cr monolayer on a FM Fe(100) surface is FM, with a large local magnetic moment $\mu = 3.63$ Bohr magnetons, and is aligned antiferromagnetically with respect to the bulk Fe substrate. The large local magnetic moment of the Cr monolayer on Fe(100) is presumably due to the combination of (100)-surface-band narrowing and the strong AFM Fe-Cr interaction. The same system has been calculated by other groups[6.4,6.15] and the local magnetic moment of the order of $\mu = 3.1$ Bohr magnetons has been predicted.

Blügel *et al.*[6.16,6.17] carried out calculations based on the full-potential linearized augmented-plane-wave method for the whole transition metal series as overlayers on Ag(100) and Pd(100). From these calculations, the authors conclude that V, Cr, and Mn overlayers on Ag(100) and Pd(100) favor an

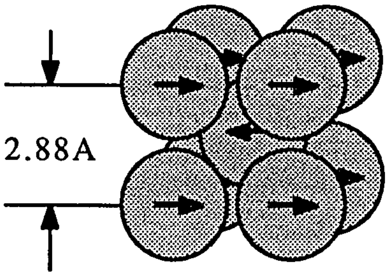

Figure 6.1 Real space spin lattice of bcc Cr structure.

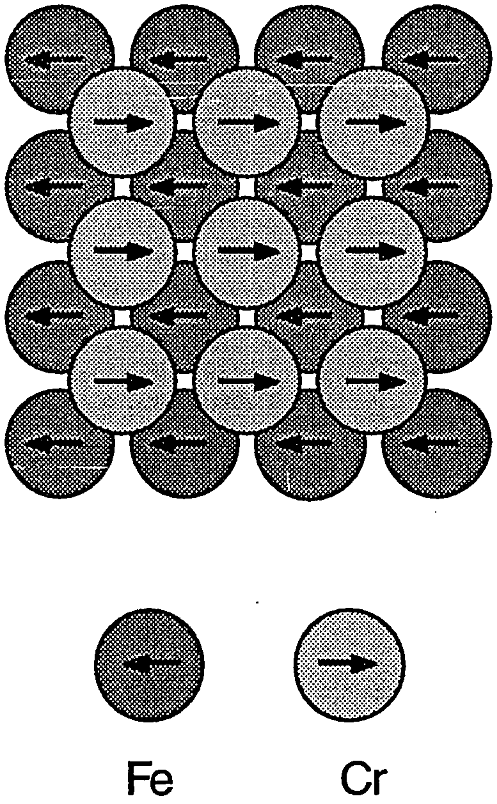

Figure 6.2 Real space spin lattice structure of monolayer Cr on Fe(100).

antiferromagnetic structure in plane. There have been no calculations for Mn overlayers on Fe(100) thus far. However, in the periodic table, the position of the Mn is between Cr and Fe. It will be therefore interesting to see how Mn overlayers behave on Fe(100).

As discussed in the previous chapter, the spin polarized $3p$ core level spectra from FM Fe and Co have a single peak in each spin direction. The minority curve is narrower and lies at lower binding energy. Since the *p-d* interactions are predominant in giving the multiplet structure in the $3p$ XPS spectra, the splitting between the majority peak and minority peak should somehow reflect the local magnetic moment through the exchange interactions between valence *d* electrons and *p* electrons. Within the simple picture we presented in chapter 5, the local moments should be proportional to the $3p$ splittings. Since the $3p$ binding energies of Cr and Mn are different from that of Fe, core level XPS can yield localized information from different elements. Therefore, a spin polarized XPS study of Cr/Fe(100) and Mn/Fe(100) should be able to conclude if the Cr or Mn monolayer on Fe(100) is ferromagnetically or antiferromagnetically coupled to Fe substrate. If antiferromagnetically coupled, the Cr or Mn core levels should order their excitation energies oppositely to those of Fe.

Jungblut *et al.*[6.18] have previously carried out a spin polarized experiment on the $3p$ core level of Cr overlayers deposited on Fe(100). The only $3p$ data shown in the paper is with 2.2 Å Cr on Fe. This is equivalent to 1.6 monolayer as the thickness of one monolayer for Cr is 1.44 Å. If the first layer of Cr is ferromagnetically ordered and aligned antiferromagnetically with respect to the Fe substrate, the second layer of Cr will align ferromagnetically with respect to the Fe substrate.[6.2] The net polarization will be reduced by the presence of the second layer. However Jungblut *et al* concluded that the Cr is ferromagnetically ordered and aligned antiferromagnetically with respect to Fe substrate, in agreement with theoretical calculation. The authors' argument was based on the 'integral polarization' of the Cr 3*p* core level spectra, i.e. $P_{\text{total}} = (I_{\text{maj}} - I_{\text{min}})/(I_{\text{maj}} + I_{\text{min}})$, which they claimed to be 13% and opposite to Fe 3*p* polarization. This argument is incorrect since the total spin of 3*p* core level electrons is paired off and cancels each other out, yielding $P_{\text{total}} = 0$ as was discussed early in this work.

6.2 Experimental Procedures

In section 2 of chapter 5, we have described the details of our experimental procedure. For bimetallic systems such as Cr or Mn monolayer(s) on Fe, the thick Fe film (normally more than 20 Å) was first epitaxially grown on the Ag(100) substrate. The thin Cr or Mn films were then grow on top of the Fe. The Cr and Mn sources were polycrystalline of size ~ 5 × 4 × 2 mm, from the Material Science Division of Applied Science Department, Brookhaven National Laboratory. The purities were claimed to be better than 99.99%. The Mn source was chemically etched by 2% nitric + 98% ethanol in the ultra-sonic bath tank at room temperature. Before being introduced into the ultrahigh vacuum chamber, all sources were cleaned by ethanol (or methanol) along with the W baskets. The sources were out-gassed over night during the baking.

Resistive heating methods were used to grow thin films. The growth rate of the evaporants were calibrated by AES before each experiment. Also, the film thickness was calibrated by AES before and after each experiment. The details of the film thickness calibration have been described in chapter 5. Unlike Fe, Cr and Mn do not form alloys with W. Therefore, the growth rates of Cr and Mn with the resistive heating method are near constant. In this case, there is another way to find out the ratio R. Assuming that the overlayer growth rate is a constant c, from equation (5.1) we have

$$r(t) = R\left(e^{c \cdot t} - 1\right). \qquad (6.1)$$

By doing several measurements of $r(t)$ in terms of overlayer growth time, R can be obtained by fitting the data with equation (6.1). Figure 6.3 shows the overlayer growth rate of Cr on Fe(100) at room temperature by using this method. The constants a = 1.44 Å[6.19] and $\lambda(E)$ = 10 Å[6.20] (at E = 550 eV) were used. The R for the solid dots was obtained by fitting and that of the open dots was obtained from the handbook.[6.21] Both data match each other fairly well. This indicates that it is reasonable to use the R value from the handbook, especially when the overlayer growth rate is not a constant such as Fe from a W basket.

Since the XPS signal intensity from the sub-monolayer Cr or Mn were only 10% of that from the substrate, it took ten times longer to obtain a signal-to-noise ratio equivalent to the thick Fe film. Further more, in order to cover both components of the peaks, with the same energy resolution, one has to take more points in the spectrum. In practice, a 3*p* spin polarized XPS spectrum from the submonolayer system takes five to six hours. Therefore the spectrum was obtained by summing two sets of data in order to reduce the effects of contamination. Changes in the Fe 3*p* peaks were used to see if the sample was contaminated.

6.3 Magnetic Properties of Cr and Mn Monolayers on Fe(100)

Experiments were carried out with different Cr and Mn film thicknesses. Figure 6.4 shows a typical 3*p* core level spin polarized XPS spectra from Cr and Fe. The upper spectrum is the spin integrated 3*p* spectrum from one monolayer

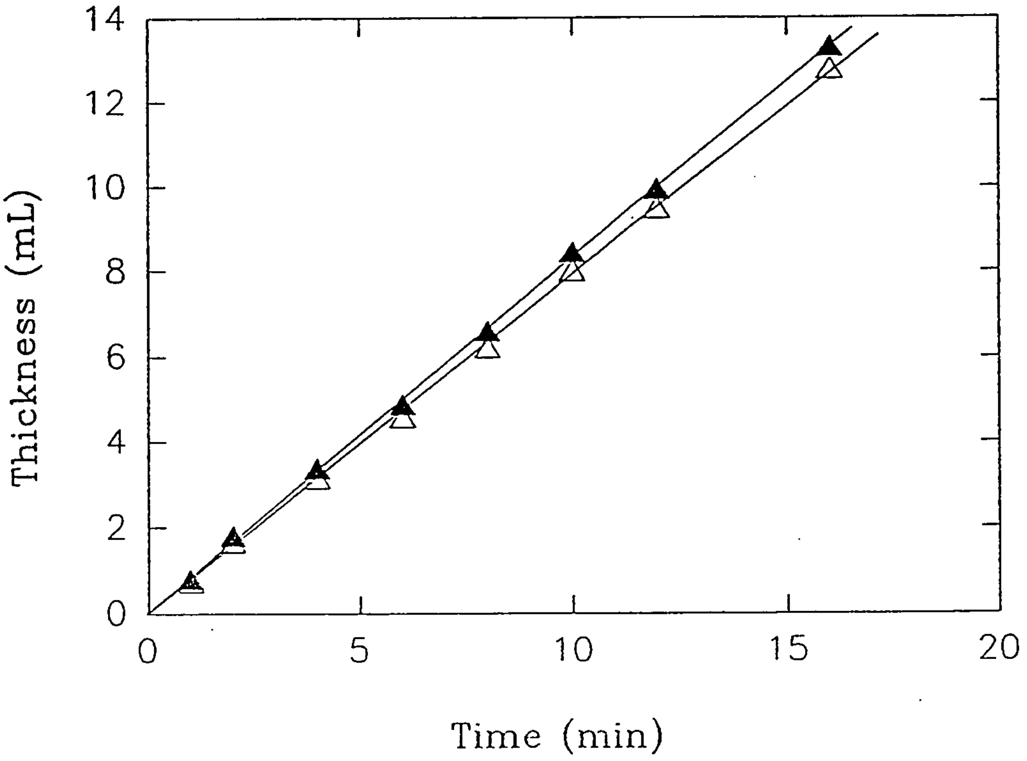

Figure 6.3 Overlayer growth rate of Cr on Fe(100) at room temperature. Solid triangles are from the fitting and open triangles are from the handbook (see text).

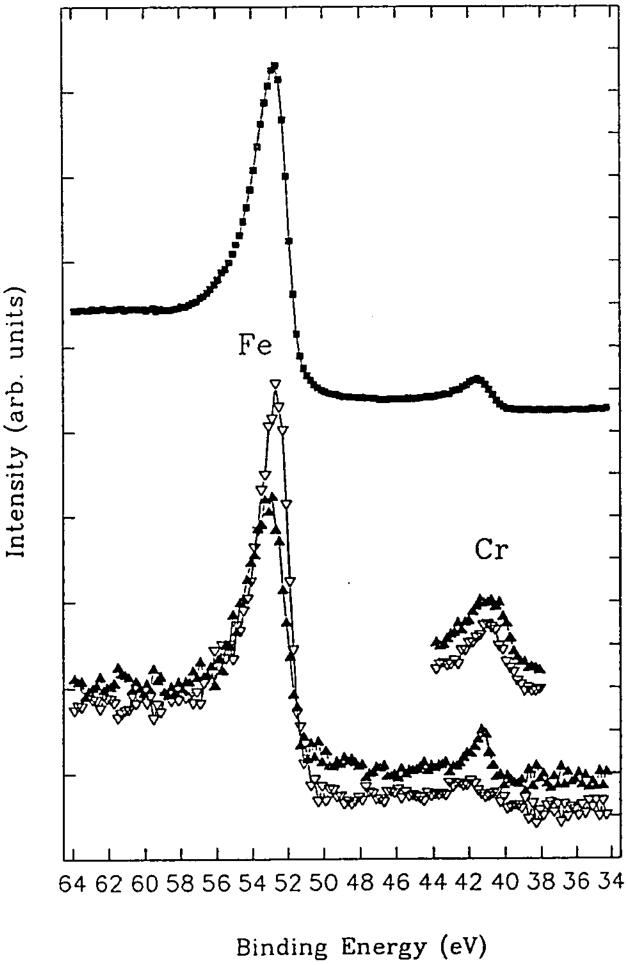

Figure 6.4 Spin polarized $3p$ core level XPS spectra of Fe and Cr from thin film Cr/Fe(100) at room temperature. Top: integrated spectrum, middle: 2.5 Å Cr, bottom: 1 Å Cr. Open triangles: minority spin curve, solid triangles: majority spin curve. hν = 250 eV.

Cr on Fe(100). The lower spectra are the spin polarized 3*p* spectra from Fe and a 1.0 Å Cr overlayer. The big peaks at the higher binding energy (left) are the Fe 3*p* emission and the smaller peaks are the Cr 3*p* emission. Also shown are spin resolved spectra from 2.3 Å Cr on Fe(100). In both cases, the Fe 3*p* spectra show no detectable changes when compared with the spectra from a clean Fe sample.

Figure 6.5 shows expanded Cr 3*p* spectra from 1.0 Å Cr on Fe(100). The measured overall splitting between the peaks of the two Cr 3*p* spin channels is 0.85 eV. The majority spin curve has a full width at half maximum (FWHM) of 1.2 eV, the minority spin curve of 2.6 eV. The absolute value of the linewidth-ratio of the curves in two spin channels is bigger in Cr than in Fe, but with reversed signs, meaning, the minority-spin peak is broader in Cr while the majority-spin peak is broader in Fe.

If we reverse the majority and minority spins in Cr, the Cr 3*p* spectra is similar to the 3*p* spectra of Fe and Co. This means that the order of the Cr core level excitation energies is opposite to those of Fe. This is direct evidence showing that the monolayer Cr on Fe(100) surface is antiferromagnetically coupled to the Fe substrate. The observation of spin polarization in the Cr peak is evidence of ferromagnetic alignment within the layer.

Figure 6.6 shows a 3*p* core level spin polarized XPS spectra from the system of Mn monolayer on Fe(100). The lower spectra are the spin polarized 3*p* spectra. The peak of a binding energy of 47.2 eV corresponds to the Mn 3*p* peak. The upper spectrum is the spin integrated 3*p* spectrum. The Fe 3*p* curves do not show any detectable changes when compared with the spectra from a clean Fe sample. Spin polarized Mn 3*p* spectra from Mn/Fe(100) with different Mn film thicknesses both at room temperature and at –120°C produced no measurable net spin polarization. Figure 6.7 shows the expanded Mn 3*p* spectra from 1.0 Å Mn on Fe(100). The majority and the minority curves are identical within the

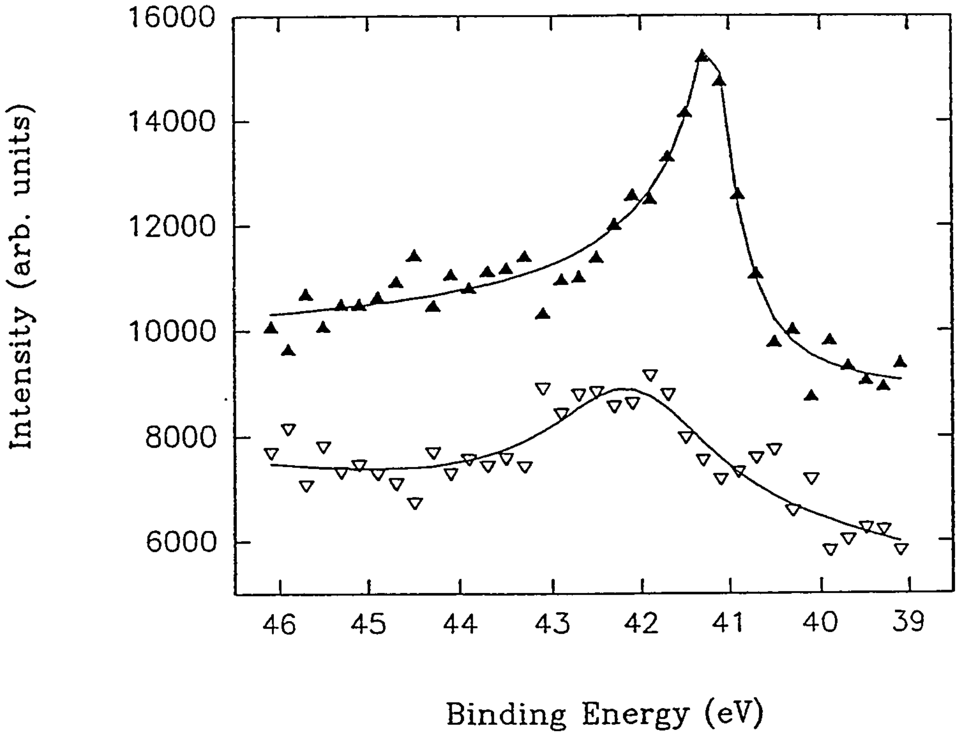

Figure 6.5 Spin polarized 3*p* core level XPS spectra of Cr from 1 Å Cr/Fe(100) at room temperature. Open triangles: minority spin curve, solid triangles: majority spin curve. hv = 250 eV.

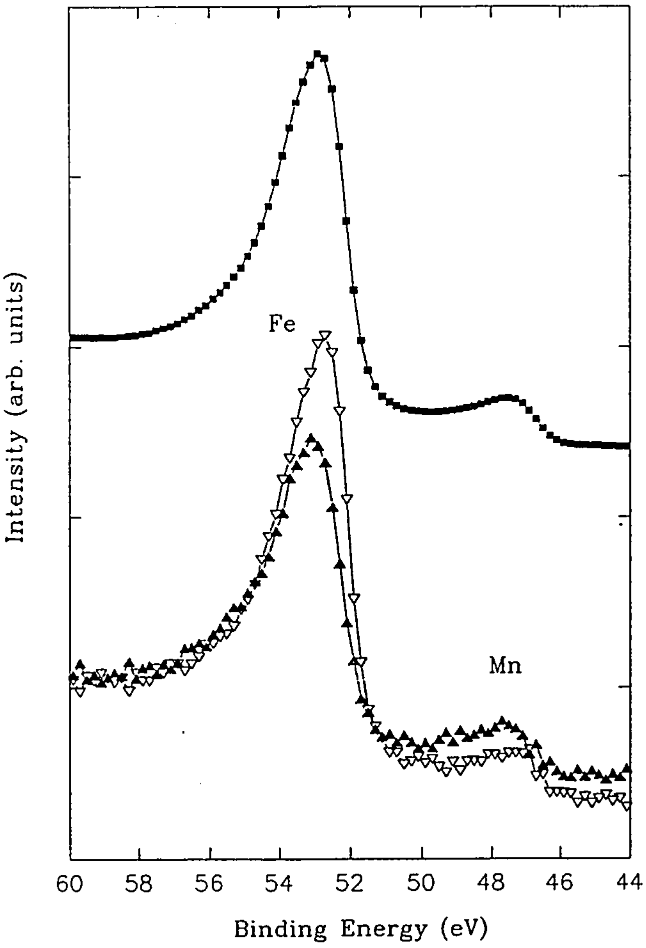

Figure 6.6 Spin polarized 3*p* core level XPS spectra of Fe and Mn from thin film Mn/Fe(100) at room temperature. Top: integrated spectrum, bottom: 1 Å Mn. Open triangles: minority spin curve, solid triangles: majority spin curve. hν = 250 eV.

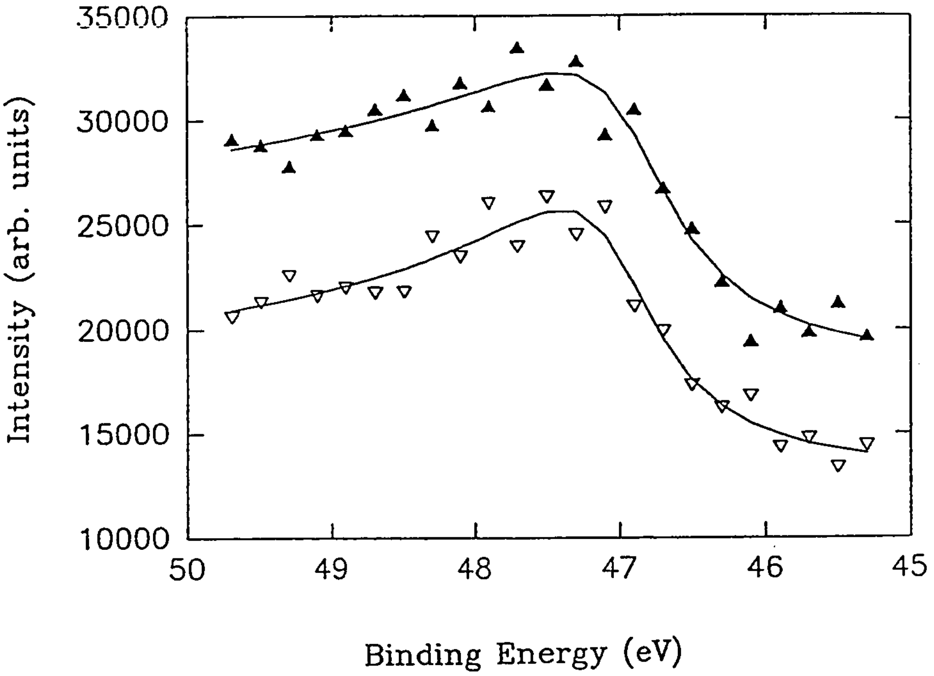

Figure 6.7 Spin polarized 3*p* core level XPS spectra of Mn from 1 Å Mn/Fe(100) at −120°C. Open triangles: minority spin curve, solid triangles: majority spin curve. hν = 250 eV.

experimental error except for a shift due to the background spin polarization. This result indicates that the Mn monolayer(s) on Fe(100) does not appear to form a ferromagnetic structure above temperature –120°C. However, based on our experimental results, we do not know if the Mn overlayer forms an antiferromagnetic structure or does not have any magnetic order at all.

In chapter 5, we have discussed a simple model for describing the *p* core level spin polarized XPS spectra. The overall majority-minority splitting reflects the center-of-weight splitting between the majority peaks and minority peaks, which is determined by the peak intensities and the exchange interactions. Figure 6.8 shows the Cr 3*p* spectra generated with Lorentzian line shapes base on the simple model. The linewidth of 0.8 eV was used since the full-width-half-maximum of the overall minority curve of the experimental data is 1.2 eV. The results in figure 6.8 agree with the experimental data show in figure 6.5, which has an overall majority-minority splitting of 0.85 eV. The splitting caused by exchange interaction is adjusted by the experiment data, yields 0.92 eV in this case.

We know that the local magnetic moment for bulk Co is 1.6 μ_B, and Fe is 2.1 μ_B. The local moment on a site is proportional to the number of spin imbalanced valence electrons. In chapter 5, we have described the Fe and Co 3*p* core level spin polarized XPS spectra with a simple model, which results the exchange interaction of 0.58 eV for Co and 0.75 eV for Fe. If we still believe that the exchange splitting between the $^{2S_d+2}P$ and ^{2S_d}P multiplets caused by exchange interaction between the core electrons and unbalanced valence electrons is proportional to the number of spin unbalanced valence electrons, then the exchange interaction of 0.92 eV for Cr 3*p* yields a local moment of ~ 3 μ_B. This value is consistent with that of the theoretical calculation.[6.4,6.14-15]

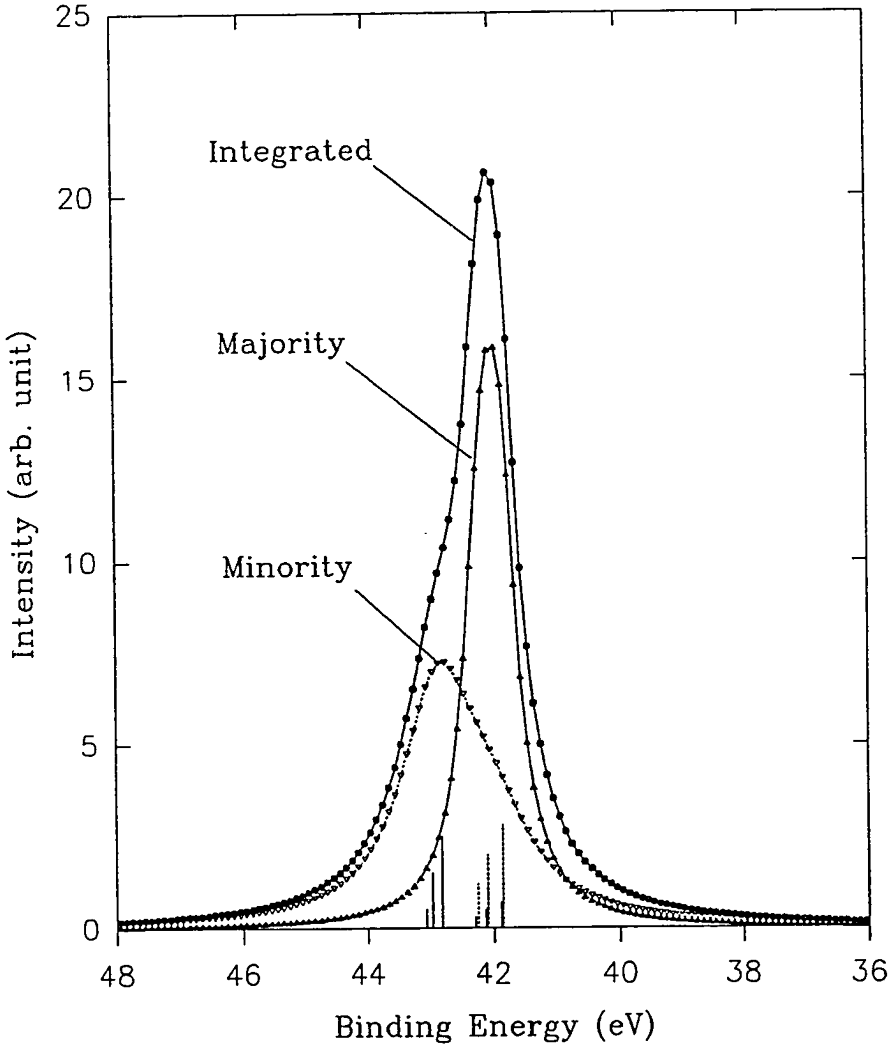

Figure 6.8 Calculated spin polarized $3p$ core level XPS spectra of Cr. Dashed (solid) lines show minority (majority) spectra lines.

For Cr 3*p* spectra of 2.3 Å, corresponds to 1.65 monolayers of Cr on Fe(100), two curves of different spin channels are identical within the experiment statistic errors. This is because the second layer of Cr aligned antiferromagnetically with respect to the first layer of Cr and ferromagnetically aligned with respect to the Fe substrate. So the polarization of the first layer will be reduced by the second layer and can not be measured.

SUMMARY

The theoretical and experimental problems of spin polarized XPS study has been summarized and discussed.

A new electron spectrometer for spin polarized x-ray photoelectron spectroscopy (XPS) study has been presented. With a plane mirror analyzer (PMA) connected in between the hemispherical electron energy analyzer and the low energy diffuse scattering electron spin polarimeter, this analyzer can simultaneously measure both transverse and longitudinal electron spin polarization components. The operating characteristics of the spectrometer is demonstrated on X1B, an undulator based soft x-ray beamline at the National Synchrotron Light Source (NSLS) with simple ferromagnetic systems such as Fe and Co, and the results are consistent with existing data.

More complex systems of Cr and Mn thin films on Fe(100) have been studied experimentally with the spectrometer on X1B beamline. The spin polarized core level photoemission from a Cr monolayer on Fe(100) shows that the Cr monolayer is ferromagnetically aligned within the plane but antiferromagnetically aligned with respect to the Fe substrate. With the deposition of a second monolayer of Cr, it is no longer possible to measure a net spin polarization in the Cr 3*p* level. This is consistent with a picture in which the Cr layers couple antiferromagnetically with respect to each other. Spin polarized Mn 3*p* spectra of Mn overlayer on Fe(100) with different Mn film thicknesses at both room temperature and –120° C show no measurable net polarization. The results indicate that the Mn overlayer on Fe(100) can not form ferromagnetic structure above temperature T = –120°C.

A simple model for the description of core level spin polarized photoelectron spectra of 3*d* transition metals has been used. The model is based on the core hole atomic multiplet structure, and the *d* electron orbital moment quenching due to delocalization. Within a single configuration, the model demonstrates that: (1) *s* level has three peaks: one minority peak and two majority peaks with one at lower binding energy degenerated with that of the minority peak; (2) in a jj coupling scheme, $2p_{1/2}$ level has four peaks: two minority peaks degenerate with two majority peaks, and $2p_{3/2}$ level has eight peaks in general: four minority peaks degenerate with four majority peaks; (3) the picture of 3*p* level is less clear but in an LS coupling scheme, 3*p* level has three minority peaks and, in general, six majority peaks with three at lower binding energies degenerated with those of the minority peaks; and (4) the overall splitting between majority curve and minority curve reflects the *p-d* electron interactions and the competition between the peak intensities decided by the CG coefficients.

The experimental results of monolayer Cr on Fe(100) are interpreted in terms of this simple model, which yields the local magnetic moment of ~ 3 Bohr magnetons which is consistent with the theoretical predictions.

Measurements of 3*s* and 2*p* levels are suggested for future experiments of thin film studies. For 3*s* level, the spin-orbit interactions are not involved. The spectra reflect the exchange interaction between the remaining *s* core level electron and valence *d* electrons. Therefore, the picture of the 3*s* level is simpler than that of the *p* levels. However it is difficult to conduct the 3*s* level measurement, since the 3*s* spin polarized XPS signal from a thin film is very small.

Spin-orbit interaction of a 2*p* electron is one order of magnitude larger than the *d-p* electron interactions. The 2*p* spectra should have two main peaks in each spin channel due to the strong *p* level spin-orbit interaction. The picture of the 2*p* level is simpler than that of the 3*p* level because like 3*s* level, for each of the main peaks, the *p* level spin-orbit interactions are not involved. Furthermore, like the 3*p* level, the photoemission cross section of the 2*p* level electrons is much larger than that of the 3*s* level electrons. However, the measurements of the 2*p* levels require an intense photon source with energy range up to 1 keV.

With the availability of more intense photon sources at the range of 400 eV - 1 keV, the current experimental set up could be fully utilized to conduct the 3*s* level and the 2*p* level measurements which would lead to a better understanding of the magnetic properties of thin films.

APPENDICES

Appendix 1. 3*d* Transition Metal Spin Polarized *s* Core Level Spectra Intensity Ratios

Without loss of generality, the atomic configuration of an initial state can be written as $n_l l^k(S_lL_l)$, where n and l are the principal and the orbital quantum numbers for the valence electrons, k is the number of the valence electrons, and S_l and L_l are the total spin and orbital angular momenta of the valence electrons respectively. For 3*d* transition metals, the total spin of all the unbalanced valence electrons are well aligned in an atom. Therefore $M_{L_l} = S_l$ and the initial state wave function becomes

$$\Psi_i\left(S_lM_{S_l},L_lM_{L_l}\right)=\Psi_i\left(S_lS_l,L_lM_{L_l}\right), \tag{A 1.1}$$

where M_{S_l} and M_{L_l} are the angular momentum components of S_l and L_l. Upon photoionization, the final state configuration can be written as $n_l l^k(S_lL_l)nl'(SL)$. For *s* level photoionization, $l' = 0$. Thus the initial state and the final state have the same orbital angular momentum. The total spin angular momentum is then the coupling of the S_l and $s = 1/2$, the total spin angular momentum of the valence electrons and the spin angular momentum of the core hole. The intensity of XPS spectra must then be proportional to

$$I(S,m_s)=\left|\left\langle S_lM_{S_l};sm_s\middle|SM_S\right\rangle\right|^2=\left|\left\langle S_lS_l;\frac{1}{2}M_S-S_l\middle|SM_S\right\rangle\right|^2, \tag{A 1.2}$$

where $\langle j_1m_1;j_2m_2|jm\rangle=\langle j_1m_1;j_2m-m_1|jm\rangle$ is the standard CG coefficient. Therefore, for the majority energy distribution curve, $m_s = -1/2$, we have

$$I_{\text{maj}}\left(S_l+\frac{1}{2}\right)=I\left(S_l+\frac{1}{2},-\frac{1}{2}\right)=\left|\sqrt{\frac{S_l-\left(S_l-\frac{1}{2}\right)+\frac{1}{2}}{2S_l+1}}\right|^2=\frac{1}{2S_l+1}, \qquad \text{(A 1.3)}$$

$$I_{\text{maj}}\left(S_l-\frac{1}{2}\right)=I\left(S_l-\frac{1}{2},-\frac{1}{2}\right)=\left|\sqrt{\frac{S_l+\left(S_l-\frac{1}{2}\right)+\frac{1}{2}}{2S_l+1}}\right|^2=\frac{2S_l}{2S_l+1}. \qquad \text{(A 1.4)}$$

For the minority curve, $m_s = +1/2$, we have

$$I_{\text{min}}\left(S_l+\frac{1}{2}\right)=I\left(S_l+\frac{1}{2},\frac{1}{2}\right)=\left|\sqrt{\frac{S_l+\left(S_l+\frac{1}{2}\right)+\frac{1}{2}}{2S_l+1}}\right|^2=1, \qquad \text{(A 1.5)}$$

$$I_{\text{min}}\left(S_l-\frac{1}{2}\right)=I\left(S_l-\frac{1}{2},\frac{1}{2}\right)=\left|-\sqrt{\frac{S_l-\left(S_l+\frac{1}{2}\right)+\frac{1}{2}}{2S_l+1}}\right|^2=0. \qquad \text{(A 1.6)}$$

So the majority curve has two peaks and the intensity ratio between $S_l + 1/2$ and $S_l - 1/2$ peaks is

$$R_{\text{maj}} = \frac{I_{\text{maj}}(S_l + 1/2)}{I_{\text{maj}}(S_l - 1/2)} = \frac{1}{2S_l} \qquad \text{(A 1.7)}$$

The minority curve has only one peak which is degenerate with the $I_{\text{maj}}(S_l + 1/2)$ majority peak. The ratio of the majority and minority curves is

$$R_{\text{maj/min}} = \frac{I_{\text{maj}}(S_l + 1/2) + I_{\text{maj}}(S_l - 1/2)}{I_{\text{min}}(S_l + 1/2) + I_{\text{min}}(S_l - 1/2)} = 1 \qquad \text{(A 1.8)}$$

as we expect since the spin of the core level electrons are paired off. Finally, the intensity ration between $S_l + 1/2$ and $S_l - 1/2$ peaks is

$$R_{\text{total}} = \frac{I_{\text{maj}}(S_l + 1/2) + I_{\text{min}}(S_l + 1/2)}{I_{\text{maj}}(S_l - 1/2) + I_{\text{min}}(S_l - 1/2)} = \frac{S_l + 1}{S_l}, \qquad \text{(A 1.9)}$$

the same as given by van Vleck.[1.7]

Those results can be extended to the delocalized situation by the following arguments.

For *s* level photoionization, the orbital momentum of the remaining *s* level electron $l' = 0$. The initial state and the final state have the same orbital angular momentum. Therefore, the total spin angular momentum is the coupling of spin angular momentum of the remaining *s* level electron $s = 1/2$ and the total spin angular momentum of the localized *d* electrons S_l. In the delocalized case, the *d* electrons are hopping from site to site with averaged total spin imbalance *S* at the site of each atom. The neutron diffraction process takes ~ 10^{-12} s (about the order of the moment fluctuation time); and therefore the averaged moment would be measured. This cannot occur in the XPS process which takes only 10^{-15} s. Therefore the *d* electron configuration interaction will produce more satellite lines on the core level spectra. The total spin angular momentum in this case is the coupling of the spin angular momentum of the remaining *s* level electron $s = 1/2$ and the configuration spin angular momentum of the *d* electrons, *S*, at the site instead of the localized *d* electrons S_l. Therefore the intensity ratios of equations (A 1.7) — (A 1.9) are valid even for the delocalized case for different *d* electron configurations.

Appendix 2. 3*d* Transition Metal Spin Polarized 2*p* Core Level Spectra Intensity Ratios

In the 2*p* case, the spin-orbit interaction of *p* hole is one order of magnitude larger than the others. The spectra consist of two main peaks due to the spin orbit splitting of the *p* level and these peaks are broadened by the other interactions to have the width of about 1 eV. With core hole spin orbit coupling, we have, for $p_{1/2}$,

$$\varphi\left(\frac{1}{2},\frac{1}{2}\right) = -\sqrt{\frac{1}{3}}\phi(1,0)\alpha + \sqrt{\frac{2}{3}}\phi(1,1)\beta \qquad \text{(A 2.1)}$$

$$\varphi\left(\frac{1}{2},-\frac{1}{2}\right) = -\sqrt{\frac{2}{3}}\phi(1,-1)\alpha + \sqrt{\frac{1}{3}}\phi(1,0)\beta \qquad \text{(A 2.2)}$$

and for $p_{3/2}$,

$$\varphi\left(\frac{3}{2},\frac{3}{2}\right) = \phi(1,1)\alpha \qquad \text{(A 2.3)}$$

$$\varphi\left(\frac{3}{2},\frac{1}{2}\right) = \sqrt{\frac{2}{3}}\phi(1,0)\alpha + \sqrt{\frac{1}{3}}\phi(1,1)\beta \qquad \text{(A 2.4)}$$

$$\varphi\left(\frac{3}{2},-\frac{1}{2}\right) = \sqrt{\frac{1}{3}}\phi(1,-1)\alpha + \sqrt{\frac{2}{3}}\phi(1,0)\beta \qquad \text{(A 2.5)}$$

$$\varphi\left(\frac{3}{2},-\frac{3}{2}\right) = \phi(1,-1)\beta \qquad \text{(A 2.6)}$$

where $\phi(l,m_l)$ are the orbit part of the wave functions; α and β are the spin part of the wave function for $m_s = 1/2$ and $-1/2$ respectively; $\varphi(j,m_j)$ are the wave functions after spin-orbit coupling.

Secondly, the *d* electron spin-orbit couplings can be neglected, as for the same arguments above. Therefore, for 3*d* transition metals, we can consider the total angular momentum of the *d* electrons felt by the core hole as the averaged total spin angular momentum of the d electrons on the site S_d. The total spin of all the unpaired valence electrons will be well aligned for ferromagnetic transition metals, and hence $m_{S_d} = S_d$. The angular momentum coupling of the core hole and the valence d electrons then gives (let $\varphi(S_d, S_d) = 1$), for $p_{1/2}$

$$\psi\left(S_d + \frac{1}{2}, S_d + \frac{1}{2}\right) = -\sqrt{\frac{1}{3}}\phi(1,0)\alpha + \sqrt{\frac{2}{3}}\phi(1,1)\beta \qquad \text{(A 2.7)}$$

$$\psi\left(S_d + \frac{1}{2}, S_d - \frac{1}{2}\right) = \sqrt{\frac{1}{2S_d+1}}$$

$$\left(-\sqrt{\frac{2}{3}}\phi(1,-1)\alpha + \sqrt{\frac{1}{3}}\phi(1,0)\beta\right) \qquad \text{(A 2.8)}$$

$$\psi\left(S_d - \frac{1}{2}, S_d - \frac{1}{2}\right) = \sqrt{\frac{2S_d}{2S_d+1}}$$

$$\left(-\sqrt{\frac{2}{3}}\phi(1,-1)\alpha + \sqrt{\frac{1}{3}}\phi(1,0)\beta\right) \qquad \text{(A 2.9)}$$

and for $p_{3/2}$,

$$\psi\left(S_d + \frac{3}{2}, S_d + \frac{3}{2}\right) = \phi(1,1)\alpha \qquad \text{(A 2.10)}$$

$$\psi\left(S_d + \frac{3}{2}, S_d + \frac{1}{2}\right) = \sqrt{\frac{3}{2S_d+3}}$$

$$\left(\sqrt{\frac{2}{3}}\phi(1,0)\alpha + \sqrt{\frac{1}{3}}\phi(1,1)\beta\right) \qquad \text{(A 2.11)}$$

$$\psi\left(S_d + \frac{3}{2}, S_d - \frac{1}{2}\right) = \sqrt{\frac{3}{(2S_d+2)(2S_d+3)}}$$

$$\left(\sqrt{\frac{1}{3}}\phi(1,-1)\alpha + \sqrt{\frac{2}{3}}\phi(1,0)\beta\right) \qquad \text{(A 2.12)}$$

$$\psi\left(S_d+\frac{3}{2},S_d-\frac{3}{2}\right)=$$

$$\sqrt{\frac{3}{(2S_d+1)(S_d+1)(2S_d+3)}}\phi(1,-1)\beta \qquad \text{(A 2.13)}$$

$$\psi\left(S_d+\frac{1}{2},S_d+\frac{1}{2}\right)=\sqrt{\frac{2S_d}{(2S_d+3)}}$$

$$\left(\sqrt{\frac{2}{3}}\phi(1,0)\alpha+\sqrt{\frac{1}{3}}\phi(1,1)\beta\right) \qquad \text{(A 2.14)}$$

$$\psi\left(S_d+\frac{1}{2},S_d-\frac{1}{2}\right)=\sqrt{\frac{8S_d}{(2S_d+1)(2S_d+3)}}$$

$$\left(\sqrt{\frac{1}{3}}\phi(1,-1)\alpha+\sqrt{\frac{2}{3}}\phi(1,0)\beta\right) \qquad \text{(A 2.15)}$$

$$\psi\left(S_d+\frac{1}{2},S_d-\frac{3}{2}\right)=\sqrt{\frac{6}{(2S_d+1)(2S_d+3)}}\phi(1,-1)\beta \qquad \text{(A 2.16)}$$

$$\psi\left(S_d-\frac{1}{2},S_d-\frac{1}{2}\right)=\sqrt{\frac{2S_d(2S_d-1)}{(2S_d+1)(2S_d+2)}}$$

$$\left(\sqrt{\frac{1}{3}}\phi(1,-1)\alpha+\sqrt{\frac{2}{3}}\phi(1,0)\beta\right) \qquad \text{(A 2.17)}$$

$$\psi\left(S_d-\frac{1}{2},S_d-\frac{3}{2}\right)=\sqrt{\frac{6S_d}{(2S_d+1)(2S_d+2)}}\phi(1,-1)\beta \qquad \text{(A 2.18)}$$

$$\psi\left(S_d-\frac{3}{2},S_d-\frac{3}{2}\right)=\sqrt{\frac{2(S_d-1)}{2S_d+1}}\phi(1,-1)\beta \qquad \text{(A 2.19)}$$

where $\psi(J,m_J)$ are the wave functions after the core hole and the valence *d* electrons coupling.

The $p_{1/2}$ peak splits into two peaks, $I\left(S_d + \frac{1}{2}\right)$ and $I\left(S_d - \frac{1}{2}\right)$, due to the exchange interaction between the core hole and valence electrons. The $I\left(S_d + \frac{1}{2}\right)$ peak is of lower binding energy compared with $I\left(S_d - \frac{1}{2}\right)$ peak as the corresponding final state is with lower energy. For the majority spin components, $m_s = -1/2$ (β), we have

$$I_{\text{maj}}\left(S_d + \frac{1}{2}\right) = \frac{4S_d + 3}{3(2S_d + 1)} \tag{A 2.20}$$

$$I_{\text{maj}}\left(S_d - \frac{1}{2}\right) = \frac{2S_d}{3(2S_d + 1)} \tag{A 2.21}$$

and for the minority spin spin components, $m_s = +1/2$ (β), we have

$$I_{\text{min}}\left(S_d + \frac{1}{2}\right) = \frac{2S_d + 3}{3(2S_d + 1)} \tag{A 2.22}$$

$$I_{\text{min}}\left(S_d - \frac{1}{2}\right) = \frac{4S_d}{3(2S_d + 1)} \tag{A 2.23}$$

Therefore the total intensity ratio between the two peaks of $p_{1/2}$ is

$$R_{\text{total}} = \frac{I_{\text{maj}}\left(S_d + \frac{1}{2}\right) + I_{\text{min}}\left(S_d + \frac{1}{2}\right)}{I_{\text{maj}}\left(S_d - \frac{1}{2}\right) + I_{\text{min}}\left(S_d - \frac{1}{2}\right)} = \frac{S_d + 1}{S_d} \tag{A 2.24}$$

The intensity ratio of the majority curve between the two peaks is

$$R_{\text{maj}} = \frac{I_{\text{maj}}\left(S_d + \frac{1}{2}\right)}{I_{\text{maj}}\left(S_d - \frac{1}{2}\right)} = 2 + \frac{3}{2S_d} \tag{A 2.25}$$

and that of the minority curve between the two peaks is

$$R_{\min} = \frac{I_{\min}\left(S_d + \frac{1}{2}\right)}{I_{\min}\left(S_d - \frac{1}{2}\right)} = \frac{1}{2} + \frac{3}{4S_d} \qquad \text{(A 2.26)}$$

The ratios of the majority and minority curves are

$$R\left(S_d + \frac{1}{2}\right) = \frac{I_{\text{maj}}\left(S_d + \frac{1}{2}\right)}{I_{\min}\left(S_d + \frac{1}{2}\right)} = \frac{4S_d + 3}{2S_d + 3} \qquad \text{(A 2.27)}$$

$$R\left(S_d - \frac{1}{2}\right) = \frac{I_{\text{maj}}\left(S_d - \frac{1}{2}\right)}{I_{\min}\left(S_d - \frac{1}{2}\right)} = \frac{1}{2} \qquad \text{(A 2.28)}$$

The ratio of the total majority and minority intensities for $p_{1/2}$ is

$$R_{\text{maj/min}}\left(p_{1/2}\right) = \frac{\sum I_{\text{maj}}\left(p_{1/2}\right)}{\sum I_{\min}\left(p_{1/2}\right)} =$$

$$\frac{I_{\text{maj}}\left(S_d + \frac{1}{2}\right) + I_{\text{maj}}\left(S_d - \frac{1}{2}\right)}{I_{\min}\left(S_d + \frac{1}{2}\right) + I_{\min}\left(S_d - \frac{1}{2}\right)} = 1 \qquad \text{(A 2.29)}$$

The $p_{3/2}$ peak splits into four peaks, $I\left(S_d + \frac{3}{2}\right)$, $I\left(S_d + \frac{1}{2}\right)$, $I\left(S_d - \frac{1}{2}\right)$, and $I\left(S_d - \frac{3}{2}\right)$, with binding energies in ascending order, reflecting the exchange interaction between the core hole and valence electrons. For the majority spin components, $m_s = -1/2$ (β), we have

$$I_{\text{maj}}\left(S_d + \frac{3}{2}\right) = \frac{S_d + 2}{(S_d + 1)(2S_d + 1)} \quad \text{(A 2.30)}$$

$$I_{\text{maj}}\left(S_d + \frac{1}{2}\right) = \frac{2(S_d + 3)}{3(2S_d + 1)} \quad \text{(A 2.31)}$$

$$I_{\text{maj}}\left(S_d - \frac{1}{2}\right) = \frac{S_d(4S_d + 7)}{3(S_d + 1)(2S_d + 1)} \quad \text{(A 2.32)}$$

$$I_{\text{maj}}\left(S_d - \frac{3}{2}\right) = \frac{2(S_d - 1)}{2S_d + 1} \quad \text{(A 2.33)}$$

and for the minority spin components, $m_s = +1/2$ (β), we have

$$I_{\text{min}}\left(S_d + \frac{3}{2}\right) = \frac{S_d + 2}{S_d + 1} \quad \text{(A 2.34)}$$

$$I_{\text{min}}\left(S_d + \frac{1}{2}\right) = \frac{4S_d}{3(2S_d + 1)} \quad \text{(A 2.35)}$$

$$I_{\text{min}}\left(S_d - \frac{1}{2}\right) = \frac{S_d(2S_d - 1)}{3(S_d + 1)(2S_d + 1)} \quad \text{(A 2.36)}$$

$$I_{\text{min}}\left(S_d - \frac{3}{2}\right) = 0 \quad \text{(A 2.37)}$$

Therefore the total intensity ratios between the four peaks of $p_{3/2}$ are

$$R_{\text{total}} = I\left(S_d + \frac{3}{2}\right) : I\left(S_d + \frac{1}{2}\right) : I\left(S_d - \frac{1}{2}\right) : I\left(S_d - \frac{3}{2}\right) = (S_d + 2):(S_d + 1):S_d:(S_d - 1) \quad \text{(A 2.38)}$$

where $I = I_{\text{maj}} + I_{\text{min}}$.

The intensity ratios of the majority curve between the four peaks are

$$R_{\text{maj}} = I_{\text{maj}}\left(S_d + \frac{3}{2}\right) : I_{\text{maj}}\left(S_d + \frac{1}{2}\right) : I_{\text{maj}}\left(S_d - \frac{1}{2}\right) : I_{\text{maj}}\left(S_d - \frac{3}{2}\right) = 3(S_d + 2):2(S_d + 1)(S_d + 3):S_d(4S_d + 7):$$

$$6(S_d - 1)(S_d + 1) \tag{A 2.39}$$

The intensity ratios of the minority curve between the four peaks are

$$R_{\min} = I_{\min}\left(S_d + \frac{3}{2}\right) : I_{\min}\left(S_d + \frac{1}{2}\right) : I_{\min}\left(S_d - \frac{1}{2}\right) : I_{\min}\left(S_d - \frac{3}{2}\right) =$$

$$3(2S_d + 1)(S_d + 2) : 4S_d(S_d + 1) : S_d(2S_d - 1) : 0 \tag{A 2.40}$$

The ratios of the majority and minority curves are

$$R\left(S_d + \frac{3}{2}\right) = \frac{I_{\text{maj}}\left(S_d + \frac{3}{2}\right)}{I_{\min}\left(S_d + \frac{3}{2}\right)} = \frac{1}{2S_d + 1} \tag{A 2.41}$$

$$R\left(S_d + \frac{1}{2}\right) = \frac{I_{\text{maj}}\left(S_d + \frac{1}{2}\right)}{I_{\min}\left(S_d + \frac{1}{2}\right)} = \frac{S_d + 3}{2S_d} \tag{A 2.42}$$

$$R\left(S_d - \frac{1}{2}\right) = \frac{I_{\text{maj}}\left(S_d - \frac{1}{2}\right)}{I_{\min}\left(S_d - \frac{1}{2}\right)} = \frac{4S_d + 7}{2S_d - 1} \tag{A 2.43}$$

$$R\left(S_d - \frac{3}{2}\right) = \frac{I_{\text{maj}}\left(S_d - \frac{3}{2}\right)}{I_{\min}\left(S_d - \frac{3}{2}\right)} = \infty \tag{A 2.44}$$

The ratio of the total majority and minority intensities for $p_{3/2}$ is

$$R_{\text{maj/min}}\left(p_{3/2}\right) = \frac{\sum I_{\text{maj}}\left(p_{3/2}\right)}{\sum I_{\min}\left(p_{3/2}\right)} = 1 \tag{A 2.45}$$

Equations (A 6.30) and (A 6.46) yield the ratio of the total majority and minority intensities for both $p_{1/2}$ and $p_{3/2}$ which is

$$R_{\mathrm{maj/min}} = \frac{\sum I_{\mathrm{maj}}\left(p_{1/2}\right) + \sum I_{\mathrm{maj}}\left(p_{3/2}\right)}{\sum I_{\mathrm{min}}\left(p_{1/2}\right) + \sum I_{\mathrm{min}}\left(p_{3/2}\right)} = 1 \qquad \text{(A 2.46)}$$

as we expected since the spin of the core level electrons are paired off.

REFERENCES

1.1 H. Hertz, Ann. Physik **31**, 983 (1887).

1.2 A. Einstein, Ann. Physik **17**, 132 (1905).

1.3 K. Siegbahn, C. Nordling, A. Fahlman, R. Nordberg, K. Hamrin, J. Hedman, G. Johansson, T. Bergmark, S. E. Karlsson, I. Lindgren, and B. Lindberg, *ESCA, Atomic, Molecular and Solid State Structure Studied by Means of Electron Spectroscopy* (Nova Acta Regiae Societatis Scientiarum Upsaliensis, 1967), Ser. IV, Vol. 20.

1.4 C. S. Fadley, D. A. Shirley, A. J. Freeman, P. S. Bagus, and J. V. Mallow, Phys. Rev. Lett. **23**, 1397 (1969).

1.5 C. S. Fadley and D. A. Shirley, Phys. Rev. A **2**, 1109 (1970).

1.6 S. Hüfner and G. K. Wertheim, Phys. Rev. B **7**, 2333 (1973).

1.7 J. H. van Vleck, Phys. Rev. **45**, 405 (1934).

1.8 F. R. McFeely, S. P. Kowalczyk, L. Ley, and D. A. Shirley, Solid State Commun. **15**,1051 (1974).

1.9 C. Binns, C. Norris, G. P. Willianms, M. G. Barthes, and H. A. Padmore, Phys. Rev. B **34**, 8221 (1986).

1.10 H. I. Starnberg, M. T. Johnson, D. Pescia, and H. P. Hughes, Surf. Sci. **178**, 336 (1986).

1.11 S. Hüfner and G. K. Wertheim, Phys. Rev. Lett. **51A**, 299 (1975).

1.12 P. C. Kemeny and N. J. Shevchik, Solid State Commun. **17**, 255 (1975).

1.13 G. van der Laan, J. Zaanen, G. A. Sawatzky, T. Karnatak, and J.-M. Esteva, Phys. Rev. B **33**, 4253 (1986).

1.14 Y. Kakehashi, K. Becher, and P. Fulde, Phys. Rev. B **29**, 16(1984).

1.15 B. W. Veal and A. P. Paulikas, Phys. Rev. B **31**, 5399 (1985).

1.16 Y. Kakehashi, Phys. Rev. B **32**, 1607 (1985).

1.17 J. F. van Acker, Z. M. Stadnik, J. C. Fuggle, H. J. W. M. Hoekstra, K. H. J. Buschow, and G. Stroink, Phys. Rev. B **37**, 6827 (1988).

1.18 J. H. Wood and G. W. Pratt, Jr., Phys. Rev. **107**, 995 (1957).

1.19 J. C. Slater, *Quantum Theory of Atomic Structure* (McGraw-Hill, New York, 1960). Vol. II.

1.20 L. D. Landau, Soviet Phys. JEPT **3**, 920 (1957)

1.21 P. S. Bagus, A. J. Freeman, and F. Sasaki, Phys. Rev. Lett. **30**, 850 (1973).

1.22 S. P. Kowalczyk, L. Ley, R. A. Pollak, F. R. McFeeley, and D. A. Shirley, Phys. Rev. B **7**, 4009 (1973).

1.23 F. R. Mcfeely, S. P. Kowalczyk, L. Ley, and D. A. Shirley, Solid State Commun. **15**, 1051 (1974).

1.24 J. C. Carver, G. K. Schweitzer, and T. A. Carlson, J. Chem. Phys. **57**, 973 (1972).

1.25 G. K. Wertheim, S. Hüfner, and H. J. Guggenheim, Phys. Rev. B **7**, 556 (1973).

1.26 C. Binns, C. Norris, G. P. Williams, M. G. Barthes, and H. A. Padmore, Phys. Rev. B **34**, 8221 (1986).

1.27 A. Kotani, Y. Toyozawa, J. Phys. Soc. Jpn. **37**, 912 (1974).

1.28 Y. Kakehashi and A. Kotani, Phys. Rev. B **29**, 4292 (1984).

1.29 S. -J. Oh, G. -G. Gweon, and J. -G. Park, Phys. Rev. Lett. **68**, 2850 (1992).

1.30 C. Carbone and E. Kisker, Solid State Commun. **65**, 1107 (1988).

1.31 T. Kachel, C. Carbone, W. Heinen, and W. Gudat, BESSY Annual Report 1989, P. 178 (unpublished).

1.32 B. Sinkovic, P. D. Johnson, N. B. Brookes, A. Clark, and N. V. Smith, Phys. Rev. Lett. **65**, 1647 (1990).

1.33 W. Clemens, E. Vescovo, T. Kachel, C. Carbone, and W. Eberhardt, Phys. Rev. B **46**, 4198 (1992).

1.34 C. Carbone, T. Kachel, R. Rochow, and W. Guldat, Z. Physik B **79**, 325 (1990).

1.35 F. U. Hillebrecht, T. Jungblut, and E. Kisker, Phys. Rev. Lett. **65**, 2450 (1992).

1.36 J. C. Fuggle and S. F. Alvarado, Phys. Rev. A **22**, 1615 (1980).

1.37 L. Corliss, J. Hastings, and R. Weiss, Phys. Rev. Lett. **3**, 211 (1959).

1.38 R. H. Victora and L. M. Falicov, Phys. Rev. B **31**, 7335 (1985).

1.39 C. L. Fu and A. J. Freeman, Phys. Rev. B 33, 1755 (1986).

1.40 P. D. Johnson, Proceedings of the VUV X Conference, Paris 27 – 31 July 1992, World Scientific Publishing.

1.41 R. Jungblut, Ch. Roth, F. U. Hillebrecht, and E. Kisker, J. Appl. Phys. **70**, 5923 (1991); R. Jungblut, Ch. Roth, F. U. Hillebrecht, and E. Kisker, Surface Sci. **269**, 615 (1992).

1.42 T. G. Walker, and A. W. Pang, H. Hopster, and S. G. Alvarado, Phys. Rev. Lett. **69**, 1121 (1992).

2.1 S. Krinsky, IEEE Trans. Nucl. Sci. **NS-30**, 3078 (1978).

2.2 C. Bckley, H. Rarback, T. Alforque, K. Shu, H. Ade, S. Hellmann, N. Iskander, J. Kirz, S. Lindaas, I. McNulty, M. Oversluizen, E. Tang, D. Attwood, R. DiGennaro, M. Howells, C. Jacobsen, Y. Vladimirsky, S. Rothman, D. Kern, and D. Sayre, Rev. Sci. Instrum. **60**, 2444 (1989).

2.3 C. T. Chen, Nucl. Instrum. Methods A **256**, 595 (1987).

2.4 C. T. Chen and F. Sette, Rev. Sci. Instrum. **60**, 1616 (1989).

2.5 W. Eberhardt, K. J. Randall, J. Feldhaus, A. M. Bradshaw, R. F. Garrett, and M. L. Knotek, Phys. Scr. **41**, 745 (1990).

2.6 S. L. Hulbert and S. Sharma, Nucl. Instr. Meth. Phys. Res. A **266**, 491 (1988).

2.7 H. Haber, J. Opt. Soc. Am. **40**, 153 (1950).

2.8 N. Noda, T. Namioka, and M. Seya, J. Opt. Soc. Am. **64**, 1031 (1974).

2.9 W. T. McKinney and M. R. Howells, Nucl. Instr. and Meth. **172**, 149 (1980).

2.10 H. Tarback, C. Jacobsen, J. Kirz, and I. McNulty, Nucl. Instrum. Methods A**266**, 96 (1988).

2.11 M. Tronc, G. C. King, and F. H. Read, J. Phys. B **12**, 137 (1979).

2.12 M. Tronc, G. C. King, and F. H. Read, J. Phys. B **13**, 999 (1980).

2.13 R. N. S. Sodhi and C. E. Brion, J. Electron. Spectrosc. **34**, 363 (1984).

2.14 M. Domke, A. Puschmann, T. Mandel, C. Xue, E. Hudson, D. A. Shirley, G. Kaindl, H. Petersen, and P. Kuske, BESSY Jahresbericht 1990, BESSY GmbH, Berlin, 1991, p. 99.

2.15 Y. Ma, C. T. Chen, G. Meigs, K. Randall, and F. Sette, Phys. Rev. A **44**, 1848 (1991).

2.16 A. P. Hitchcock and C. E. Brion, J. Electron. Spectrosc. **18**, 1 (1980).

2.17 W. Eberhardt, J. -E. Rubensson, K. J. Randall, J. Feldhaus, A. L. D. Kilcoyne, A. M. Bradshaw, Z. Xu, Y. Ma, and P. D. Johnson. Physica Scripta **t41**, 143 (1992).

2.18 K. J. Randall, A. K. D. Kilcoyne, H. -M. Koppe, J. Feldhaus, A. M. Bradshaw, Z. Xu, P. D. Johnson, Y. Ma, J. -E. Rubesson, and W. Eberhardt, Proceedings of the VUV X Conference, Paris 27 – 31 July 1992, World Scientific Publishing.

3.1 N. F. Mott, Proc. R. Soc. A **124**, 425 (1929); A **135**, 429 (1932).

3.2 J. Kessler, *Polarized Electrons* (Springer-Verlag, Berlin-Heidelber-New York, 1976).

3.3 C. G. Shull, C. T. Chase, and F. E. Myers, Phys. Rev. **63**, 29 (1943).

3.4 E. Kisker, G. Baum, A. H. Mahan, W. Raith, and B. Reihl, Phys. Rev. B **18**, 2256 (1978).

3.5 K. Jost, F. Kaussen, and J. Kessler, J. Phys. E **14**, 735 (1981).

3.6 L. A. Hodge, T. J. Moravec, F. B. Dunning, and G. K. Walters, Rev. Sci. Instrum. **50**, 5 (1979).

3.7 L. G. Gray, M. W. Hart, F. B. Dunning, and G. K. Walters, Rev. Sci. Instrum. **55**, 88 (1984).

3.8 D. M. Campbell, C. Hermann, G. Lampel, and R. Owen, J. Phys. E **18**, 664 (1985).

3.9 J. Kierschner and R. Feder, Phys. Rev. Lett. **42**, 1008 (1979).

3.10 D. Tillmann, R. Thiel, and E. Kisker, Z. Phys. B **77**, 1 (1989).

3.11 M. R. Scheinfein, J. Unguris, M. H. Kelley, D. T. Pierce, and R. J. Celotta, Rev. Sci. Instrum. **61**, 2501 (1990).

3.12 A. M. Bincer, Phys. Rev. **107**, 1434 (1957).

3.13 G. W. Ford and C. J. Mullin Phys. Rev. **108**, 477 (1957).

3.14 C. Møller, Ann. Phys. **14**, 532 (1932).

3.15 M. Eminyan and G. Lampel, Phys. Rev. Lett. **45**, 1171 (1980).

3.16 D. T. Pierce, S. M. Girvin, J. Unguris, and R. J. Celotta, Rev. Sci. Instrum. **52**, 1437 (1981).

3.17 J. Unguris, D. T. Pierce, and R. J. Celotta, Rev. Sci. Instrum. **57**, 1314 (1986).

3.18 W. B. Herrmannsfeldt, *EGUN-AN ELECTRON OPTICS AND GUN DESIGN PROGRAM*, National Technical Information Service, U. S. Dept. of Commerce (1988)

3.19 C.E. Kuyatt and J.A. Simpson, Rev. Sci. Instrum. **38**, 103 (1967)

3.20 G. A. Harrower, Rev. Sci. Instrum. **26**, 850 (1955).

3.21 S. Tanuma, C. J. Powell, and D. R. Penn, Surface and Interface Analysis, **11**, 577 (1988).

3.22 R.E. Imhof, A. Adms, and G.C. King, J. Phys. E **9**, 138 (1976)

3.23 M. Cardona and L. Ley, *Photoemission from Solids I* (Springer-Verlag, Berlin-Heidelber-New York, 1978).

3.24 C. Carbone and E. Kisker, Solid State Commun. **65**, 1107 (1988).

3.25 T. Kachel, C. Carbone, W. Heinen, and W. Gudat, BESSY Annual Report 1989, P. 178 (unpublished).

3.26 B. Sinkovic, P. D. Johnson, N. B. Brookes, A. Clark, and N. V. Smith, Phys. Rev. Lett. **65**, 1647 (1990).

3.27 W. Clemens, E. Vescovo, T. Kachel, C. Carbone, and W. Eberhardt, Phys. Rev. B **46**, 4198 (1992).

3.28 J. H. van Vleck, Phys. Rev. **52**, 1178 (1937).

3.29 C. Liu, E. T. Moog and S. D. Bader, Phys. Rev. Lett. **60**, 2422 (1988).

3.30 B. Heinrich, K. B. Urquhart, A. S. Arrott, J. F. Cochran, K. Myrtle and S. T. Purcell, Phys. Rev. Lett. **59**, 1756 (1987).

3.31 N. C. Koon, B. T. Jonker, F. A. Volkening, J. J. Krebs and G. A. Prinz, Phys. Rev. Lett. **59**, 2463 (1987).

3.32 J. R. Dutcher, B. Heinrich, J. F. Cochran, D. A. Steigerwald and W. F. Egelhoff, Jr., J. Appll. Phys. **63**, 3464 (1988).

3.33 D. Pescia, M. Stampanoni, G. L. Bona, A. Vaterlaus, R. F. Willis and F. Meier, Phys. Rev. Lett. **58**, 2126 (1987).

3.34 Z. Q. Qiu, J. Pearson, and S. D. Bader, Phys. Rev. Lett. **70**, 1006 (1993).

3.35 C. Liu and S. C. Bader, J. appl. Phys. **67**, 5758 (1990).

3.36 K. Binder and P. C. Hohenberg, IEEE Trans. Mag. MAG-**12**, 66 (1976).

4.1 K. J. Randall, J. Feldhaus, W. Erlebach, A. M. Bradshaw, W. Eberhardt, Z. Xu, Y. Ma, and P. D. Johnson, Rev. Sci. Instrum. **63**, 1367 (1992).

4.2 K. J. Randall, J. Feldhaus, W. Erlebach, A. M. Bradshaw, W. Eberhardt, Z. Xu, Y. Ma, and P. D. Johnson, *Synchrotron Radiation News*, **4**, 16 (1991).

4.3 J. Kessler, *Polarized Electrons* (Springer-Verlag, Berlin-Heidelber-New York, 1976).

4.4 D. Roy and J. D. Carette, *Topics in Current Physics*, ed. H. Ibach (Springer-Verlag, Berlin, 1977), **4**.

4.5 K. D. Sevier, *Low Energy Electron Spectrometry* (Wiley, New York, 1972).

4.6 D. P. Woodruff and T. A. Delchar, *Modern Techniques of Surface Science, (Cambridge University*, Cambridge, 1986).

5.1 S. Ohnishi, A. J. Freeman, and M. Weinert, Phys. Rev. B **28**, 6741 (1983).

5.2 E. Wimmer, A. J. Freeman, and H. Krakauer, Phys. Rev. B **30**, 3113 (1984).

5.3 L. I. Chu, A. J. Freeman, and C. L. Fu, J. Magn. Magn. Mater. **75**, 53 (1988).

5.4 S. Ohnishi, M. Weinert, and A. J. Freeman, Phys. Rev. B **30** 36 (1984).

5.5 J. J. Yeh and I. Lindau, Atomic Data and Nulclear Data Tables, **32**, 1 (1985).

5.6 W. B. Pearson, *A Handbook of Lattice spacings and Structure of Metals and Alloy* (Pergamon Press, Oxford, 1958), P. 123.

5.7 S. Tanuma, C. J. Powell, and D. R. Penn, Surface and Interface Analysis, **11**, 577 (1988).

5.8 L. E. Davis, N. C. MacDonald, P. W. Palmberg G. E. Riach, and R. E. Webber, *Handbook of Auger Electron Spectroscopy* (Physical electronics Industries, Inc., 1976).

5.9 T. Kachel, C. Carbone, W. Heinen, and W. Gudat, BESSY Annual Report 1989, P. 178 (unpublished).

5.10 C. Carbone and E. Kisker, Solid State Commun. **65**, 1107 (1988).

5.11 B. Sinkovic, P. D. Johnson, N. B. Brookes, A. Clark, and N. V. Smith, Phys. Rev. Lett. **65**, 1647 (1990).

5.12 W. Clemens, E. Vescovo, T. Kachel, C. Carbone, and W. Eberhardt, Phys. Rev. B **46**, 4198 (1992).

5.13 S. Doniach and M. Sunjic, J. Phys. C **3**, 285 (1970).

5.14 J. F. van Acker, Z. M. Stadnik, J. C. Fuggle, H. J. W. M. Hoekstra, K. H. J. Buschow, and G. Stroink, Phys. Rev. B **37**, 6827 (1988).

5.15 S. -J. Oh, G. -G. Gweon, and J. -G. Park, Phys. Rev. Lett. **68**, 2850 (1992).

5.16 P. S. Bagus, A. J. Freeman, and F. Sasaki, Phys. Rev. Lett. **30**, 850 (1973).

5.17 T. Yamaguchi, S. Shibuya, and S. Sugano, J. Phys. C **15**, 2625 (1982).

5.18 J. H. van Vleck, *The Theory of Electric and Magnetic Susceptibilities* (Oxford, 1952), P. 285.

5.19 J. H. van Vleck, Rev. of Mod. Phys. **25**, 220 (1953).

5.20 E. U. Condon and H. Odabasi, *Atomic Structure* (Cambridge University Press, 1980), P.576.

5.21 B. W. Shore and D. H. Menzel, *Principles of Atomic Spectra* (John Wiley & son, Inc, 1968), P.360.

5.22 R. P. Gupta and S. K. Sen, Phys. Rev. B **10**, 71 (1974); B **12**, 15 (1975).

5.23 R. Rekha, S. Pal, and R. P. Gupta, Phys. Rev. B **26**, 35 (1982).

5.24 R. E. Watson, *MIT Technical Report*, No 12 (1959).

5.25 C. Satoko and S. Sugano, J. Phys. Soc. Japan 34, 701 (1973).

6.1 T. Shinjo, Surface Science Reports **12**, 49 (1991).

6.2 T. G. Walker, and A. W. Pang, H. Hopster, and S. G. Alvarado, Phys. Rev. Lett. **69**, 1121 (1992).

6.3 D. T. Pierce, R. J. Celotta, and J. Unguris, J. Appl. Phys. (1993) to be published.

6.4 P. D. Johnson, Proceedings of the VUV X Conference, Paris 27 – 31 July 1992, World Scientific Publishing.

6.5 P. Grünberg, R. Schreiber, Y. Pang, M. B. Brodsky, and H. Sowers, Phys. Rev. Lett. **57**, 2442 (1986); P. Grünberg, R. Schreiber, Y. Pang, U. Walz, M. B. Brodsky, and H. Sowers, J. Appl. Phys. **61**, 3750 (1987).

6.6 C. Carbone and S. F. Alvarado, Phys. Rev. B **36**, 2433 (1987).

6.7 F. Saurenbach, U. Walz, L. Hinchey, P. Grünberg, W. Zinn, J. Appl. Phys. **63**, 3473 (1988).

6.8 M. N. Baibich, J. M. Broto, A. Fert, F. Nguyen van Dau, F. Petroff, P. Etienne, G. Creuzet, A. Fredrich, and J. Chazelas, Phys. Rev. Lett. **61**, 2472 (1988).

6.9 A. Barthélémy, A. Fert, M. N. Baibich, S. Hadjoudj, F. Petroff, P. Etienne, R. Cabanel, S. Lequien, F. Nguyen van Dau, and G. Creuzet, J. Appl. Phys. **67**, 5908 (1990).

6.10 J. J. Krebs, P. Lubitz, A. Chaiken, and G. A. Prinz, J. Appl. Phys. **67**, 5920 (1990).

6.11 J. Unguris, R. J. Celotta, and D. T. Pierce, Phys. Rev. Lett. **67**, 140 (1991); J. Unguris, R. J. Celotta, and D. T. Pierce, Phys. Rev. Lett. **69**, 1125 (1992).

6.12 L. Corliss, J. Hastings, and R. Weiss, Phys. Rev. Lett. **3**, 211 (1959).

6.13 E. Fawcett, Rev. Mod. Phys. **60**, 209 (1988).

6.14 R. H. Victora and L. M. Falicov, Phys. Rev. B **31**, 7335 (1985).

6.15 C. L. Fu and A. J. Freeman, Phys. Rev. B 33, 1755 (1986).

6.16 S. Blügel, M. Weinert, and P. H. Dederichs, Phys. Rev. Lett. **14**, 1077 (1988).

6.17 S. Blügel, B. Drittler, R. Zeller, and P. H. Dederichs, Appl. Phys. A **49**, 547 (1989).

6.18 R. Jungblut, Ch. Roth, F. U. Hillebrecht, and E. Kisker, J. Appl. Phys. **70**, 5923 (1991); R. Jungblut, Ch. Roth, F. U. Hillebrecht, and E. Kisker, Surface Sci. **269**, 615 (1992).

6.19 W. B. Pearson, *A Handbook of Lattice spacings and Structure of Metals and Alloy* (Pergamon Press, Oxford, 1958), P. 123.

6.20 S. Tanuma, C. J. Powell, and D. R. Penn, Surface and Interface Analysis, **11**, 577 (1988).

6.21 L. E. Davis, N. C. MacDonald, P. W. Palmberg G. E. Riach, and R. E. Webber, *Handbook of Auger Electron Spectroscopy*, (Physical electronics Industries, Inc., 1976).